DISSERTATION

Strong-field ionization of few-electron systems with MCTDHF

ausgeführt zum Zwecke der Erlangung des akademischen Grades
eines Doktors der technischen Wissenschaften

unter der Leitung von
Univ.Doz. Mag.rer.nat. Dr.rer.nat. Armin Scrinzi
am Institut für Photonik (E387)

eingereicht an der Technischen Universität Wien,
Fakultät für Elektrotechnik und Informationstechnik

von
DI Gerald Jordan
Matrikelnummer 9925636
Enenkelstraße 23/14
1160 Wien

Wien, September 2009

To the lighting of the inner darkness

Contents

1 Introduction

> The electron is not as simple as it looks.
>
> *(William Lawrence Bragg)*

After femtosecond chemistry has made visible nuclear motions in molecules in real time [109], attosecond technology promises to reveal electronic dynamics to us.

The natural time scale of bound electron dynamics is one atomic unit (about 24 attoseconds = 24×10^{-18} s), which is the time it takes the electron in hydrogen to revolve around the nucleus divided by 2π. Probing the electronic structure at this time scale would also afford a closer look at the dynamics between electrons. For example, in a recent calculation it was shown that after removal of an electron, the created "hole" is filled within a response time of about 50 attoseconds [13].

Over the last two decades, tools have been developed that enable us in principle to probe this physics at sub-femtosecond time resolution: phase-stabilized femtosecond lasers, and attosecond XUV pulses (for recent reviews see [44] and references therein).

The key features of femtosecond laser pulses are, (i) the high field strength comparable to the atomic Coulomb field, which allows to directly shape the potential landscape in which the electrons move, and (ii) the phase stabilization, which gives us direct control not only over the cycle-averaged intensity but also over the instantaneous applied field strength and which extends the actual time resolution down to subcycle duration.

Few-cycle high-intensity laser pulses were instrumental in producing the second tool, attosecond pulses. To produce such short pulses, one needs frequencies in the XUV regime, higher than available from lasers and other sources of sufficient brightness. The XUV photon energies also match the characteristic energy of electronic excitations in atoms, on the order of 1 au $\approx$ 27.2 eV (this would correspond to photons of about 45 nm wavelength). Shooting with a high-power laser into a gas medium results in the emission of radiation at odd multiples of the laser fundamental frequency, the so-called high harmonic generation. The process of high-harmonic generation was first discovered in 1987 [61] and then studied extensively. An intuitive explanation was found in terms of the semi-classical 3-step model: (1) an electron is tunnel-ionized near the peak of the laser field, (2) the electron is accelerated in the laser field, and (3) the electron is driven back to the atom and may recombine, emitting its energy in a photon. By restricting this process to a short time window, a continuum of XUV frequencies is generated, which made it possible to obtain isolated pulses of attosecond duration [32]. The current world record in minimum duration stands now at about 80 attoseconds [28].

Femtolasers, attosecond pulses and high harmonic generation are the crucial ingredients to expose temporal and structural information of electrons in atoms and molecules. [1]

For the typical experiment to observe electron dynamics, a pump-probe scheme is used: e.g. an XUV pulse initiates some dynamics and a IR laser field probes the result. Ultimately, one would like to have both pump and probe be an attosecond pulse, but this has not yet been accomplished: the absorption cross-section for two photons is too low for intensities of current attosecond pulse-sources. Two experimental highlights demonstrate the two ways the IR laser can be used as a probe. First, it can serve as a streaking device [35]. The principle behind this attosecond streak camera is that the final momentum of photoelectrons depends on the laser vector field at the time of birth of this electron. Since we know exactly the phase of the laser electric field, we can then reconstruct the time dependence of electron release. In one of the first paradigmatic attosecond experiments, this technique was used to measure the Auger decay time of Kr [23]. Second, the laser field can tunnel-ionize the atom excited previously by an XUV pulse. Again, it is important that the phase of the laser electric field with respect to the XUV pulse is known. This idea was realized in [99] to measure directly the rate of tunnel ionization.

High harmonic generation not only provides access to the time scales of the electronic wave functions, but also to their length scales. In the harmonic spectrum is encoded information about the ground state wave function from which the electron was ionized. The simplest example for such spatial information is the internuclear distance in a diatomic molecule, which leads to interference between the harmonic contributions from both nuclei [51, 50, 102, 36]. Carrying the idea to the extreme, efforts are made to realize a long-standing dream of chemists and physicists: to reconstruct the complete molecular orbital function of an electron in both amplitude and phase [34, 98].

Provided, of course, that such a thing as a single-electron orbital exists. This points out one of the deficiencies still predominant in attosecond science: most of the potential applications of the attosecond toolbox still rely on the implicit assumption of a single-electron model.

The importance of multi-electron effects is highlighted by another textbook example of strong-field physics: the double ionization of helium. Plotting the ionization yield as a function of laser intensity exhibits a famous "knee" in the curve [103], which is ascribed to non-sequential double ionization (NSDI), where both electrons are removed by one ionization event and not each one separately. The mechanism behind NSDI puzzled theorists for some time. It is now generally accepted that recollision is responsible: the first electron recollides with the helium atom and knocks out the second electron. The experimental signature of this is a strong momentum correlation between the two electrons, i.e. they move with a high preference in the same direction, instead of opposite to each other, as expected from Coulomb repulsion. For a correct description of this process it is clearly essential to account for the correlated motion

[1] A more detailed account of attosecond experiments and references can be found in [41].

of two electrons.

Given the excitement that attosecond science has roused, remarkably little attention has been paid to possible multi-electron effects. The surprise is somewhat abated when one considers the difficulties connected to multi-electron calculations in strong fields. Even for one electron the presence of a high-intensity, long-wavelength electric field imposes a severe burden on the computation (so that one often resorts to the strong-field approximation in its various guises (see sec. 7.1)): Absorption of a high number of low-frequency photons causes the electron to undergo wide linear excursions, requiring a large box size and inclusion of a large number of angular momenta. Both conditions increase the size of the basis set and thus calculation time.

Solving the strong-field TDSE exactly is now routinely tractable for a single electron, but already for two electrons the air becomes very thin. Very often for two electrons, and certainly for everything beyond, approximations are necessary.

There are a number of groups which have developed codes for the treatment of 1- and 2-photon single- or double-ionization of two-electron atoms/molecules by a short-wavelength field (XUV). For example, the 1-photon DI is interesting because correlation is responsible for transferring energy to the second ejected electron. 1- and 2-photon processes are much easier to treat than multi-photon ionization (MPI) in an IR field since one can restrict oneself to lower angular momenta. Still, the problem is difficult enough. In particular, the final boundary conditions, i.e. the correct wave function for the 3-body Coulomb problem is not known analytically. One usually needs large spatial extension to avoid the influence of the Coulomb field. See the recent articles [24] and [62] for a list of references on this subject.

As for the holy grail, the direct solution of the 3-dimensional 2e-TDSE in the IR regime, it has so far only been tackled by the group of Taylor et al. [92]. In their approach, the wave function is expanded in coupled spherical harmonics and a finite difference discretization is used for the radial coordinates. Issues with defining asymptotic boundary conditions are circumvented by using huge grids. By now, they have investigated ionization of helium in a wavelength range from the XUV to the IR, up to 390 nm [68] and recently even 780 nm [69].

Otherwise, there exists a variety of approximative methods for 2e-TDSE at these laser parameters. One notable approach is dimensional reduction. Usually, the strong laser field is linearly polarized and electron motion happens predominantly in this direction. This suggests to employ models with only 1 spatial dimension along the laser polarization, which have produced good results for helium ionization (see e.g. [49] and references therein). In another 1D variant, the electrons are constrained to move along the lines that point towards the two-particle Stark saddle in the presence of the field [75]. A more sophisticated concept of dimensional reduction restricts only the center-of-mass coordinate [80]. Although the idea of these models sounds plausible, it is still a drastic modification of physics and has at one point to be justified by methods without such assumptions.

For more than two electrons, the number of practical and general enough methods is limited.

The first solution that comes to mind, is the time-dependent version of Hartree-Fock

(TDHF), already employed in the early days of the business [45]. However, TDHF miserably fails to predict the famous "knee" in the DI of helium [48] due to the lack of correlation. It is intuitively clear, that HF is not a well-suited theory to describe multi-electron dynamics since HF is a mean-field theory. This means that it can only describe slow processes, where the electrons can adiabatically adapt to changes.

One method that promises to permit true multi-electron calculations possibly more cheaply than Hartree-Fock is density functional theory (DFT). In DFT, the multi-particle equation is replaced by a set of single-particle equations, where in addition to the external potential the so-called and to-be-determined exchange-correlation potential V_{xc} figures. In its time-independent form it is now the de facto standard for electronic structure calculations in material science. However, the time-dependent version [81] is plagued by serious problems, since it was shown to be unable to reproduce the famous DI-"knee" of helium [48, 73, 4]. Subsequent work has shown that the reason for this failure is the derivative discontinuity of the exact exchange-correlation potential as a function of particle number [52, 65], which is not included in standard approximations for V_{xc}. A correlation functional that takes into account this feature was only recently proposed and tested against a 1D helium calculation [20]. Another problem that still remains for TD-DFT is the correct definition of observables. Unlike for the TDSE, where one obtains the full wave function, DFT only provides the single-electron *density*. While in principle it is possible to express any observable as a functional of the density, in practice these functionals are not known, which leaves additional room for errors.

An approximation tailored for general collision physics is the R-matrix method. Here, one divides space into an internal region, comprising the atom or molecule, and an external region, where the free electron moves, and then neglects the exchange and correlation between the electrons residing in different regions. So far, application of R-matrix theory for strong-field problems has been restricted to the combination with Floquet theory [16], which is applicable to long (strictly speaking infinitely long) laser pulses. Only recently, also the time-dependent version of R-matrix theory [15] has been implemented by two groups [100, 29] and applied to multi-photon ionization of Ar and Ne.

In this thesis, we will present the multi-configuration time-dependent Hartree-Fock (MCTDHF) method for solving the 3-dimensional time-dependent multi-electron Schrödinger equation, which on the one hand provides the full wave function with no fundamental restrictions on the system parameters, and on the other hand reduces drastically the computational requirements for this. In this way MCTDHF fills the gap of a practical general-purpose computational method for few-electron systems.

Part one is dedicated to the theory and practical implementation of the MCTDHF method. We define and illustrate the term "correlation", the challenges it creates for numerical treatment, and point out an efficient way of dealing with the problem. This results in the MCTDHF ansatz, where the multi-electron wave function is expanded in a time-dependent basis of single-electron orbitals. The only approximation in MCTDHF refers to the degree of correlation taken into account. It is controllable by the number of single-electron orbitals, which allows a systematic check for convergence.

Even with such an approximative scheme, the calculations are extremely demanding, and it is therefore of utmost importance to come up with a highly optimized code. Our MCTDHF implementation makes calculations of up to 6 electrons feasible within a tolerable time range on the order of days. In principle, any Hamiltonian and any geometry can be fitted in our program framework. Originally, the method was developed for and applied to strong-field problems, such as ionization and high harmonic generation, which are the topics of this work.

In part two, we investigate multi-electron effects in the strong-field ionization of molecules. Using MCTDHF we calculate ionization yields of linear molecules in a short, strong laser pulse as a function of the molecular length, both in 1D and 3D. Contrary to some experimental observations, we find that ionization increases with the size of the molecule in 3D. At the same time we show that results from simplified 1D models are faulty already at a qualitative level.

The third part deals with multi-electron dynamics in high-harmonic generation (HHG) of molecules. Until recently, HHG was almost uniformly interpreted in terms of a single-active electron model, most notably within the 3-step model and the strong-field approximation (SFA). We first investigate the dependence of the re-colliding electron wave packet on electron correlation effects. This is followed by an in-depth analysis of HHG in molecules. We calculate high harmonic spectra with MCTDHF for diatomic molecules with 2 and 4 active electrons, and compare the results with several simplifying models, all of which leave out multi-electron dynamics. None of them can qualitatively reproduce the multi-electron results. By factorization of the total wave function into the ionic core and a single-electron orbital, we demonstrate that polarization dynamics of the multi-electronic core has to be taken into account. These findings dismiss any hope of single-electron based description of HHG in molecules.

In the last and fourth part, we address a question from laser interaction with solids. To explain optical breakdown of dielectrics at very short pulse-lengths, the so-called "forest fire" mechanism was proposed, where the ionic charge of a previous ionization event enhances laser ionization at neighboring atoms. We construct a two-electron model of this process. Using well adapted initial states to rule out any collision effects, we find no evidence for "forest fire".

In all subprojects of this thesis, multi-electron aspects are a crucial ingredient. We hope that this work helps in raising the awareness of these effects, and at the same time, through the MCTDHF method, in facilitating their theoretical treatment.

Part I

MCTDHF

2 Correlation

2.1 What is correlation?

While in statistics, correlation often denotes specifically a linear relationship between two random variables, in a more general sense, two quantities are correlated, if they are not independent. In terms of a probability distribution, the absence of correlation means that the distribution of the variable X is independent of the value of Y, and vice versa, i.e.

$$P(x, y) = P_x(x)P_y(y). \tag{2.1}$$

The connection to quantum mechanics comes from the fact that electronic wave functions describe the probability distributions of the electrons.

In physics we can ask "what is the distribution of electron 2 provided that electron 1 is at position x_1". If this distribution is independent of x_1 then the two electrons are uncorrelated. Physically, this implies that they do not interact with each other, i.e. we deal with an independent particle problem, whose Hamiltonian is of the form

$$H = \sum_{\kappa=1}^{f} h_\kappa(x_\kappa), \tag{2.2}$$

where f is the number of electrons, and h_κ is the single-particle Hamiltonian of the κ-th electron. In this case, the wave function can be written as the product of single-particle functions

$$\Psi(x_1, \ldots, x_f) = \prod_{\kappa=1}^{f} \phi_\kappa(x_\kappa). \tag{2.3}$$

More precisely, there exists a basis of energy eigenfunctions with this property. A particular state can of course be composed of a linear combination of such states.

In reality, there is an additional complication because elementary particles are indistinguishable, i.e. the Hamiltonian is invariant under particle exchange. This forces the wave function to be either symmetric or antisymmetric with respect to particle interchange, depending on whether the spin is integer or half-integer. Throughout this thesis, we consider only electrons, hence the wave function is antisymmetric under

particle exchange,

$$\Psi(x_1, \ldots, x_f) = \mathcal{A}\Big[\prod_{\kappa=1}^{f} \phi_\kappa(x_\kappa)\Big], \tag{2.4}$$

where

$$\mathcal{A} = \frac{1}{\sqrt{f!}} \sum_{\pi} (-1)^{\mathrm{sgn}(\pi)} \prod_{\kappa} \phi_\kappa(x_{\pi(\kappa)}) \tag{2.5}$$

and π runs over all permutations of $(1, \ldots, f)$. This antisymmetry introduces already some form of correlation into the wave function.

The kind of correlation we are interested in here is however brought about by particle interactions. Due to the Coulomb repulsion, electron 1 will avoid the *instantaneous* position of electron 2, creating a Coulomb hole in the diagonal of $P(x_1, x_2)$.

The traditional, and still a popular, way to deal with interacting particles is Hartree-Fock (HF) theory. In it one retains the general form of a single Slater determinant for the wave function, by taking into account of the interaction only the mean field generated by all other particles. In contrast to non-interacting particles this mean field is not known a priori and has to be determined *self-consistently* in an iterative procedure. However, it became clear very early that HF is lacking some crucial physical features, as it could not even reliably describe the binding and dissociation of diatomic molecules.

The failure of HF theory is a direct consequence of the fact that it leaves out correlation effects. This is specifically true of singlet spin states, where the spatial wave function is symmetric, while for a triplet spin state, the antisymmetry of the spatial wave function automatically guarantees a node along the diagonal $x_1 = x_2$, similar to the Coulomb hole. In the context of MCTDHF, and for the purpose of this thesis, we *define* Hartree-Fock to be uncorrelated. Any wave function that cannot be represented by a single Slater determinant is correlated in this sense.

Conceptually, one distinguishes two kinds of correlation, long-range correlation and short-range correlation [42]. The distinction is somewhat vague, but it is illuminating to look at some typical examples.

Long-range correlation is necessary to describe dissociation and ionization correctly. For a two-electron atom or molecule after single ionization, a physically sensible wave function for the singlet spin state, has the form (ϕ = bound, χ = continuum)

$$\begin{aligned} \Psi(x_1, x_2) &= \left[c_1\phi\phi + c_2\frac{1}{\sqrt{2}}(\phi\chi + \chi\phi)\right]\frac{1}{\sqrt{2}}(\uparrow\downarrow - \downarrow\uparrow) \\ &= c_1\mathcal{A}(\phi^\uparrow\phi^\downarrow) + c_2[\mathcal{A}(\phi^\uparrow\chi^\downarrow) + \mathcal{A}(\chi^\uparrow\phi^\downarrow)], \end{aligned} \tag{2.6}$$

which is a sum of the ground state Slater determinant and two Slater determinants for the ionized system. On the other hand, the restricted Hartree-Fock (RHF) wave

function is of the general form

$$\Psi_{\mathrm{RHF}} = \mathcal{A}(\xi^{\uparrow}\xi^{\downarrow}). \tag{2.7}$$

In RHF one demands that both electrons occupy the same spatial orbital. Each orbital then contains a bound and a continuum part $\xi = (1/\sqrt{2})(\phi + \chi)$, which leads to

$$\Psi_{\mathrm{RHF}} = \tfrac{1}{2}\,\mathcal{A}(\phi^{\uparrow}\phi^{\downarrow} + \phi^{\uparrow}\chi^{\downarrow} + \chi^{\uparrow}\phi^{\downarrow} + \chi^{\downarrow}\chi^{\downarrow}). \tag{2.8}$$

This necessarily contains the last contribution $\chi\chi$ where both electrons are in the continuum, implying some unphysical double ionization. As a result, RHF has a tendency to overestimate the electronic Coulomb repulsion energy, since the electrons are required to occupy the same orbital and to reside in the same spatial regions. The energetic penalty associated with this spurious double ionization suppresses at the same time single ionization in Hartree-Fock. For small ionization yield, this term, which is quadratic in the ionization probability, is of less importance, but for strong fields, this causes major errors. Unrestricted Hartree-Fock could in principle cure this deficiency, but is itself plagued by spin contamination, i.e. the fact that the wave function is not a spin eigenstate, which in turn often leads to much worse trouble.

The other type of correlation determines the short-range behavior of the wave function in the vicinity of electronic coalescence points, where the interelectronic distance $r_{ij} = 0$ for some electron pair ij. At these points, there is a singularity in the Coulomb repulsion $1/r_{ij}$ of the Hamiltonian. However, considering the (stationary) Schrödinger equation,

$$H\Psi = E\Psi, \tag{2.9}$$

we observe that the right-hand side stays finite all the time. Further, the local energy $H\Psi/\Psi = E$ should be constant, and therefore the singularity in H cannot be undone by requiring Ψ to go to zero sufficiently fast at $r_{ij} = 0$. This would imply that $\Psi = O(r_{ij}^k), k \geq 1$ for $r_{ij} \to 0$ to cancel the Coulomb singularity, but then

$$\frac{H\Psi}{\Psi} \sim \frac{\alpha_{k-1} r_{ij}^{k-1} + \alpha_k r_{ij}^k + \cdots}{r_{ij}^k + \cdots} \tag{2.10}$$

would become singular. Hence the singularity must be cancelled by another term in $H\Psi$. Kato [37] derived the necessary *cusp conditions* (for singlet states),

$$\left.\frac{\partial \Psi}{\partial r_{ij}}\right|_{r_{ij}=0} = \left.\frac{\Psi}{2}\right|_{r_{ij}=0}. \tag{2.11}$$

In general, this means that the wave function derivative with respect to single-particle coordinates is discontinuous at the coalescence point. This behavior cannot be achieved by a single product of orbitals. In fact, to correctly represent this discontinuous behavior by a sum of Slater determinants, a very large number of terms is necessary. Fortunately, sufficient accuracy for energy and other observables can be reached with a smaller basis set because the region affected by the cusp is small and contributes little to these observables. For completeness, we note that at the 3-particle coalescence point there is a logarithmic singularity [25], which also impedes convergence when using separable basis sets.

2.2 Where can we find correlation?

As we saw, HF misses some important aspects of the electron interaction, yet it often gives reasonable results. This raises the question: Under what circumstances does correlation become important? Some general reasoning:

- Separation of energy scales:
  - High energy: If the kinetic energy is considerably larger than the interaction energy, interaction can be largely neglected. Examples: free electron gas model of conductors, plasma theory.
  - Level spacing: If the energy levels are widely separated, only a few of them are energetically accessible, which limits correlation. Conversely, if there is a large number of dense-lying states, many of them can be populated. Example: atoms vs. molecules. In molecules, due to splitting of (imaginary) atomic orbitals, the excitation energies are smaller, and hence correlation is expected to be more important than in atoms.
- Separation of time scales:

  Example: When an electron is removed suddenly, the other electrons have no time to react and modify the ionization process itself. But afterwards, there will be some rearrangement, which will be governed by correlation.

Of course, energy and time are conjugate quantities, so the two aspects are not independent.

In strong-laser interaction of molecules, which is the main topic of this thesis, the presence of dense-lying molecular states and attosecond sensitivity of experiments makes it likely that correlation has an appreciable influence on experimental observations. But the significance of correlation is very much problem-dependent and cannot be easily predicted in general. This emphasizes the need for ab-initio numerical calculations.

2.3 How to cope with correlation

While correlation makes physics a lot more interesting, it turns the solution of the Schrödinger equation into an extremely daunting computational challenge:

- **Storage:** For a wave function of f electrons $\Psi(x_1, \ldots, x_f)$ on a spatial grid with L grid points, the storage requirement scales like L^f. For a realistic quasi-3D model of molecular strong-field ionization one uses e.g. 10^4 grid points and 4 electrons. In this example, we already need to store $10^{4\times4} = 10^{16}$ (complex double) numbers, corresponding to 160 PB (Petabyte) of memory, which exceeds the capacities of any existing machine by far.

- **Operations count** for applying electron-electron interaction: The two-particle interaction operator $V_{12}(x, y)$ is effectively an $L \times L$ matrix. For a single application of this operator to the wave function, we need to carry out $L^2 \times L^{f-1}$ multiplications (and roughly the same number of additions, whose cost should be negligible on current hardware). For our example above, this works out as about $10^{4\times(4+1)} = 10^{20}$ floating point operations. Even if using a large cluster of $\sim 10^3$ parallel processors with $\sim 10^{12}$ Hz each, a single application would still take $\sim 10^5$ seconds or roughly 1 day. Given that a full time propagation usually takes hundreds of thousands of applications of the Hamiltonian, this turns out to be totally unfeasible.

As the direct, brute force approach is out of the question for more than 2 electrons for the foreseeable future, we need to find smarter solutions. An intuitive grasp of the complications introduced by correlation and how one can more efficiently deal with it can be gained from a schematic visualization.

Fig. 2.1a represents the wave function of two electrons in one dimension. Antisymmetrization results in mirror symmetry about the $x = y$ line (disregarding the sign).

In Hartree-Fock, one tries to cover this blob by a single product of orbital functions, as depicted in fig. 2.1b. No matter how you stretch or squeeze this rectangle, it will miss some significant part of the real wave function.

Much better results can be achieved if we allow for a larger set of orbitals and hence more configurations to "tile" the wave function, as shown in fig. 2.1c. This is called *Multi-Configuration* Hartree-Fock.

Next we allow the wave function to vary in time, so that e.g. at time t' the wave function has changed drastically (fig. 2.1d). Our previously chosen orbital set now matches our needs quite badly. In order to achieve a reasonably realistic description of Ψ, one would require a considerably enlarged basis set. This is the approach of time-dependent Configuration Interaction (CI), i.e. using a (usually huge) fixed set of configurations (fig. 2.1e).

We can however improve the fit appreciably by using a time-dependent orbital basis (fig. 2.1f), to choose at each time the optimal basis set for a fixed basis size. This is the essence of the *Multi-Configuration Time-Dependent Hartree-Fock* (MCTDHF) method described in the following chapter.

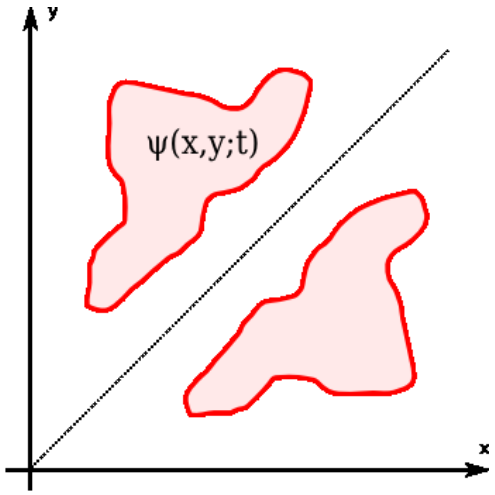

(a)

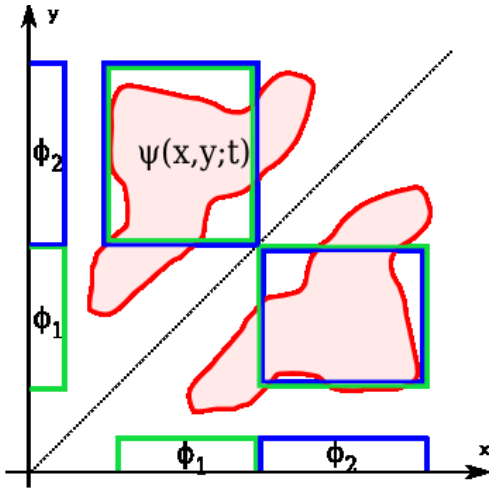

(b)

Hartree-Fock

$$\Psi(x,y) = \phi_1(x)\phi_2(y) - \phi_2(x)\phi_1(y)$$

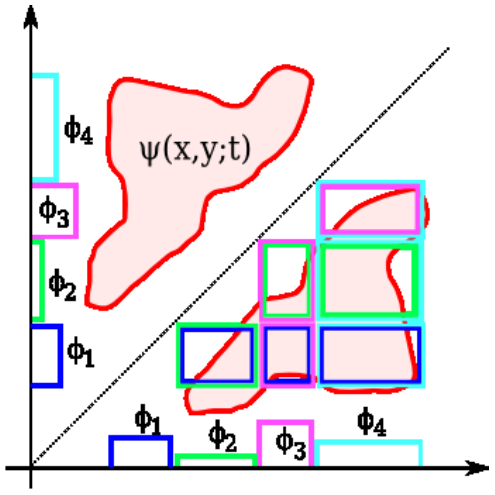

(c)

Multi-Configuration Hartree-Fock

$$\begin{aligned}\Psi(x,y;t) = {} & \phi_1(x)\phi_2(y) + \phi_1(x)\phi_3(y) \\ & + \phi_1(x)\phi_4(y) + \phi_2(x)\phi_3(y) \\ & + \phi_2(x)\phi_4(y) + \phi_3(x)\phi_4(y) \\ & - (x \leftrightarrow y)\end{aligned}$$

Figure 2.1

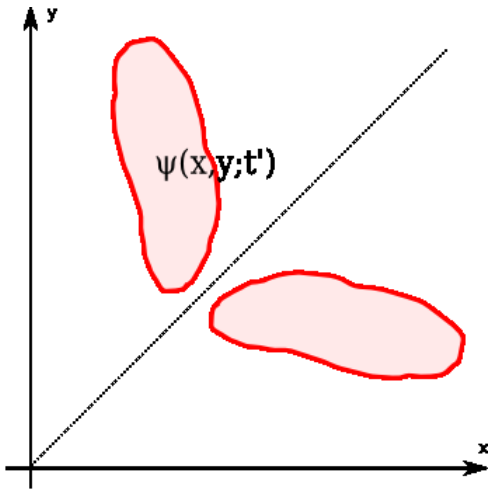

(d)

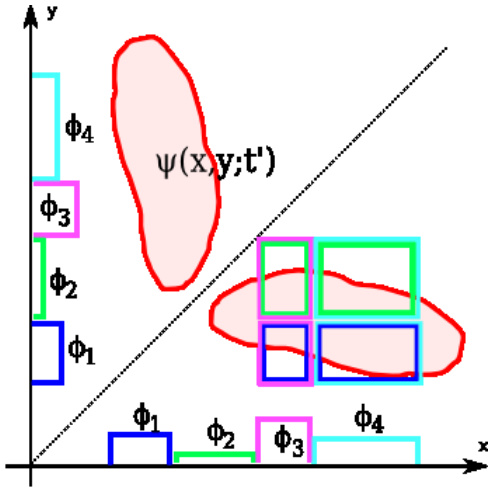

(e)

Configuration interaction
(time-independent basis)

$$\Psi(x,y;t') = \phi_1(x)\phi_4(y) + \phi_2(x)\phi_3(y) + \phi_2(x)\phi_4(y) - (x \leftrightarrow y)$$

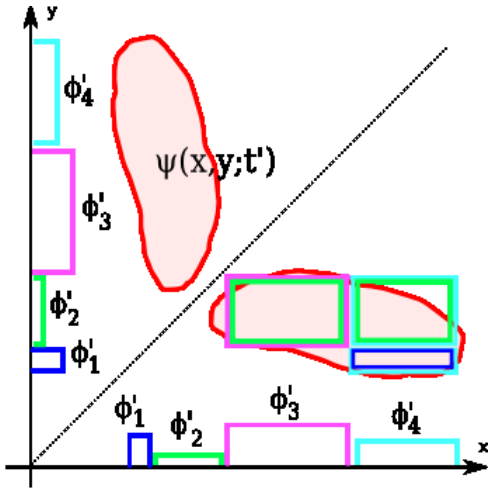

(f)

Multi-Configuration Time-Dependent
Hartree-Fock
(time-dependent basis)

$$\Psi(x,y;t') = \phi'_1(x)\phi'_4(y) + \phi'_2(x)\phi'_3(y) + \phi'_2(x)\phi'_4(y) - (x \leftrightarrow y)$$

Figure 2.1

3 MCTDHF

3.1 Ansatz

Extending the idea of Hartree-Fock, MCTDHF strives to solve the multi-electron Schrödinger equation within the subspace of multi-configuration wave functions, i.e. linear combinations of all possible f-electron Slater determinants, which can be formed from n different orbitals

$$\Psi(q_1, \dots, q_f; t) = \sum_{j_1=1}^{n} \cdots \sum_{j_f=1}^{n} B_{j_1 \cdots j_f}(t) \phi_{j_1}(q_1; t) \cdots \phi_{j_f}(q_f; t) \tag{3.1}$$

where n is the number of orbitals, f is the number of electrons, $B_{j_1 \cdots j_f}$ are the time-dependent expansion coefficients, $\phi_j(q, t)$ are the time-dependent orbitals and $q_\kappa = (\vec{r}_\kappa, m_\kappa)$ denotes the κ-th particle's coordinates including spatial coordinates and spin quantum number.

The ansatz is analogous to multi-configuration time-dependent Hartree (MCTDH) [8], but for the distinct case of indistinguishable fermions. The antisymmetry of the wave function under exchange of any two electrons is reflected in the antisymmetry of the coefficients B_J in all its indices

$$B_J = \operatorname{sign}(\pi) B_{\pi(J)}, \tag{3.2}$$

where $\pi(J)$ is any permutation of the f-tuple of indices (or multi-index) $J = (j_1, \dots, j_f)$. Thus, we can alternatively write the wave function as a sum over Slater determinants

$$\Psi(q_1, \dots, q_f; t) = \sum_{(J)} B_{(J)} \Phi_{(J)} \tag{3.3}$$

where

$$\Phi_J = \begin{vmatrix} \phi_{j_1}(q_1) & \dots & \phi_{j_f}(q_1) \\ \vdots & & \vdots \\ \phi_{j_1}(q_f) & \dots & \phi_{j_f}(q_f) \end{vmatrix} \tag{3.4}$$

is a Slater determinant, or configuration, and (J) is an *ordered* multi-index $(j_1, \dots, j_f)$, $j_1 < \cdots < j_f$. In total, there are $\binom{n}{f}$ possible Slater determinants.

The orbitals are chosen to be orthonormalized

$$\langle \phi_j | \phi_k \rangle = \delta_{jk}. \tag{3.5}$$

Note that both the coefficients and the orbitals are time-dependent. This is in contrast to configuration-interaction methods (CI), where one expands in a fixed set

of molecular states. These states are usually chosen as the lowest excited states of the time-independent problem. The advantage of MCTDHF is, that at any time, we choose the optimal set of orbitals to represent the wave function. Thus, one usually needs a substantially smaller number of configurations to get converged results. On the downside, of course, one needs to propagate the orbitals in time.

The representation (3.1) is not unique. We can choose any – possibly time-dependent – unitary $n \times n$-matrix $\boldsymbol{U}(t)$, to transform the orbitals and the coefficients

$$\phi'_j = U_{jk}\phi_k, \tag{3.6a}$$

$$B'_{j_1\cdots j_f} = U^{-1}_{j_1k_1}\cdots U^{-1}_{j_fk_f}B_{k_1\cdots k_f}. \tag{3.6b}$$

The $\boldsymbol{U}$-matrices of the B's and ϕ's cancel in Ψ, so the wave function is invariant.

In order to define unique equations of motion, we need some sort of "gauge fixing". We want to avoid for the time evolution of the ϕ's to just "re-mix" the old ϕ's. Thus, any change $\delta\phi = \dot{\boldsymbol{\phi}}\delta t$ should be orthogonal to the old orbitals:

$$\langle\dot{\boldsymbol{\phi}}_j|\phi_k\rangle = 0. \tag{3.7}$$

Making a "gauge transformation" $\boldsymbol{\phi}' = \boldsymbol{U}\boldsymbol{\phi}$, we get the alternative condition

$$\begin{aligned}\langle\dot{\boldsymbol{\phi}}'_j|\phi'_k\rangle &= U_{kl}\dot{U}^*_{jm}\langle\phi_m \mid \phi_l\rangle + U_{kl}U^*_{jm}\langle\dot{\boldsymbol{\phi}}_m \mid \phi_l\rangle \\ &= U_{kl}\dot{U}^*_{jl} \\ &= (U\dot{U}^\dagger)_{kj} \\ &= \mathrm{i}\, g_{jk},\end{aligned} \tag{3.8}$$

where $\boldsymbol{g} = -\mathrm{i}(\boldsymbol{U}\dot{\boldsymbol{U}}^\dagger)^T$ is a hermitian matrix, which follows from

$$\boldsymbol{U}\boldsymbol{U}^\dagger = \mathbb{1} \Rightarrow \dot{\boldsymbol{U}}\boldsymbol{U}^\dagger = -\boldsymbol{U}\dot{\boldsymbol{U}}^\dagger. \tag{3.9}$$

Hence, we can define a hermitian operator $\hat{\boldsymbol{g}}$ such that

$$-\mathrm{i}\,\langle\dot{\boldsymbol{\phi}}'_j|\phi'_k\rangle = \langle\phi'_j|\hat{\boldsymbol{g}}|\phi'_k\rangle = g_{jk}. \tag{3.10}$$

The role of $\boldsymbol{U}$ can be further elucidated by considering the simplest example when there is no electron-electron interaction,

$$H = \sum_{\kappa=1}^{f} h(q_\kappa). \tag{3.11}$$

The exact solution for this problem is (one Slater determinant only),

$$\Psi(q_1,\ldots,q_f;t) = B(0)\mathcal{A}[\mathrm{e}^{-\mathrm{i}\,\epsilon_1 t}\,\phi_1(q_1;0)\cdots\mathrm{e}^{-\mathrm{i}\,\epsilon_f t}\,\phi_f(q_f;0)] \tag{3.12}$$

There are now two extreme possibilities:

- The time-dependent phase goes entirely into the coefficient:

$$\begin{aligned} &\hat{g} = 0, \\ &B(t) = \mathrm{e}^{-\mathrm{i}(\epsilon_1+\cdots+\epsilon_f)t}\,, \\ &\phi_j(t) = \text{const}\,. \end{aligned} \tag{3.13}$$

- The phase goes entirely into the orbitals:

$$\begin{aligned} &\hat{g} = h_0, \\ &B(t) = \text{const}\,. \\ &\phi_j(t) = \mathrm{e}^{-\mathrm{i}\,\epsilon_j t}\,\phi_j(0). \end{aligned} \tag{3.14}$$

In conclusion, the ambiguities can be removed by condition (3.10).

3.2 Deriving equations of motion

Our goal is to solve the TDSE with the ansatz (3.1). Based on an observation of Dirac [21], Frenkel [26] has derived a variational principle for the time-dependent Schrödinger equation,

$$\langle \delta\Psi | \mathrm{i}\,\partial_t - H(t) | \Psi \rangle = 0, \tag{3.15}$$

which is most suitable to derive the equations obeyed by the MCTDHF wave function.

Condition (3.15) can be given an intuitive geometrical interpretation. The space spanned by all multi-configuration Hartree-Fock wave functions for n orbitals and f electrons is a non-linear subspace (a submanifold) $\mathcal{M}$ of the whole Hilbert space $\mathcal{H}$. The approximate solution for the wave function $\Psi(t)$ traces out a curve on this submanifold. At each point of the curve, its tangent $\dot{\Psi}(t)$ lies within the tangent space $\mathcal{T}_{\mathcal{M}}(\Psi(t))$ to $\mathcal{M}$ at $\Psi(t)$. For the exact wave function, we would have $\dot{\Psi}_{\text{exact}}(t) = -\mathrm{i}\,H\Psi_{\text{exact}}(t)$. However, $-\mathrm{i}\,H\Psi(t)$ will in general not belong to $\mathcal{T}_{\mathcal{M}}(\Psi(t))$. As an approximation, we choose the element u_t of the tangent space, which lies closest to $-\mathrm{i}\,H\Psi(t)$, i.e.

$$\dot{\Psi}(t) := u_t \in \mathcal{T}_{\mathcal{M}}(\Psi(t)) \quad \text{with} \quad \|u_t - (-\mathrm{i}\,H\Psi(t))\| \to \min\,. \tag{3.16}$$

Since fortunately $\mathcal{T}_{\mathcal{M}}(\Psi(t))$ is itself a linear subspace of the linear Hilbert space $\mathcal{H}$, we know how to compute u_t, namely by the orthogonal projection theorem. u_t is simply the orthogonal projection of $-\mathrm{i}\,H\Psi(t)$ onto the tangent space:

$$u_t = P_{\mathcal{T}_{\mathcal{M}}(\Psi(t))}(-\mathrm{i}\,H\Psi(t)). \tag{3.17}$$

But this is equivalent to saying that the difference $u_t - (-\mathrm{i}\,H\Psi(t))$ is orthogonal to the tangent space, i.e. to any variation $\delta\Psi$, which is precisely what is expressed by the Dirac-Frenkel variational principle (3.15).

The admissible variations of the MCTDHF wave function (3.1) are variations of the coefficients δB_J and of the orbitals $\delta\phi_j$. Inserting these into (3.15) and using the above-mentioned constraints

$$\langle \phi_j \mid \phi_k \rangle = \delta_{jk}, \tag{3.18a}$$

$$-\mathrm{i}\,\langle \dot{\phi}_j \mid \phi_k \rangle = \langle \phi_j \mid \hat{g}(t) \mid \phi_k \rangle, \tag{3.18b}$$

with a hermitian, but otherwise arbitrary $\hat{g}(t)$, one obtains the following working equations of MCTDHF:

$$\begin{aligned} \mathrm{i}\,\dot{B}_{j_1\cdots j_f} = &\sum_{k_1\cdots k_f} \langle \phi_{j_1}\cdots\phi_{j_f} \mid H \mid \phi_{k_1}\cdots\phi_{k_f}\rangle B_{j_1\cdots k_f} \\ &- \sum_{\kappa=1}^{f}\sum_{k=1}^{n} \langle \phi_{j_\kappa}|\hat{g}|\phi_k\rangle B_{j_1\cdots j_{\kappa-1}k j_{\kappa+1}\cdots j_f} \end{aligned} \tag{3.19a}$$

$$\mathrm{i}\,\dot{\phi}_j = \hat{g}\phi_j + (1-P)\Big[\sum_{k=1}^{n}\sum_{l=1}^{n}(\rho^{-1})_{jl}H_{lk}\phi_k - \hat{g}\phi_j\Big]. \tag{3.19b}$$

Here, ρ_{jl} denotes the density matrix,

$$\rho_{jl} = \sum_{j_2=1}^{n}\cdots\sum_{j_f=1}^{n} B^*_{jj_2\cdots j_f}B_{lj_2\cdots j_f}, \tag{3.20}$$

and P is the projector onto the space spanned by the time-dependent orbitals ϕ_j,

$$P = \sum_{j=1}^{n} |\phi_j\rangle\langle\phi_j|. \tag{3.21}$$

H_{lk} is the matrix of mean-field operators,

$$H_{lk} = \left\langle \frac{\delta\Psi}{\delta\phi_l(q_1)} \,\middle|\, H \,\middle|\, \frac{\delta\Psi}{\delta\phi_k(q_1)} \right\rangle, \tag{3.22}$$

where the functional derivative $\delta/\delta\phi_j(q_1)$ is defined as

$$\frac{\delta\Psi}{\delta\phi_l(q_1)} = B_{lj_2\cdots j_f}\phi_{j_2}(q_2)\cdots\phi_{j_f}(q_f). \tag{3.23}$$

We can rewrite the working equations in a compact manner by defining

$$K_{JL} := \langle \phi_{j_1}\cdots\phi_{j_f}|H|\phi_{l_1}\cdots\phi_{l_f}\rangle \tag{3.24}$$

and using $\boldsymbol{K}, \boldsymbol{H}, \boldsymbol{B}, \boldsymbol{\phi}, \boldsymbol{\rho}$ as short notations for the tensors in orbital space K_{JL}, H_{kl}, A_J, ϕ_j, ρ_{kl}. Then (3.19a) and (3.19b) become

$$\mathrm{i}\,\dot{\boldsymbol{B}} = \boldsymbol{K}\boldsymbol{B} \tag{3.25a}$$

$$\mathrm{i}\,\dot{\boldsymbol{\phi}} = \hat{g}\boldsymbol{\phi} + (1-P)\Big[\boldsymbol{\rho}^{-1}\boldsymbol{H}\boldsymbol{\phi} - \hat{g}\boldsymbol{\phi}\Big]. \tag{3.25b}$$

4 Implementation

4.1 Hamiltonian and working equations for laser-driven few-electron systems

In this thesis, MCTDHF is applied to few-electron systems, i.e. primarily molecules, interacting with a strong laser field. The Hamiltonian of a system of f electrons in an external electric field has the form

$$H(t) = \sum_{\kappa=1}^{f} \Big\{ \frac{1}{2} \left[-\mathrm{i}\,\vec{\nabla}_\kappa + \vec{A}(t) \right]^2 + \varphi_{\mathrm{el}}(\vec{r}_\kappa, t) + V_{\mathrm{n}}(\vec{r}_\kappa) + V_{\mathrm{cap}}(\vec{r}_\kappa) + \sum_{\lambda=\kappa+1}^{f} V_{12}(|\vec{r}_\kappa - \vec{r}_\lambda|) \Big\}. \tag{4.1}$$

If not otherwise indicated we use atomic units , where $\hbar = m_{\mathrm{e}} = e = 1$ and the electric charge of the electron is $-e$. The interaction of the electrons with the field is included in dipole approximation by the vector potential $\vec{A}(t)$ and the scalar potential $\varphi_{\mathrm{el}}(\vec{r}, t)$, where in

$$\text{velocity gauge} \quad \vec{A} \neq 0, \varphi_{\mathrm{el}} = 0 \tag{4.2a}$$

$$\text{length gauge} \quad \vec{A} = 0, \varphi_{\mathrm{el}} = \vec{E}(t) \cdot \vec{r}. \tag{4.2b}$$

The relation between the electric field and the electromagnetic potentials is defined to be $\vec{E}(t) = -\dot{\vec{A}} - \vec{\nabla}\varphi_{\mathrm{el}}$. Note that we do not include any factor of c. Therefore $\vec{A}$ has the same dimension as the momentum. The nuclei of the system are assumed fixed in space and act with the potential $V_{\mathrm{n}}(\vec{r}_\kappa)$ on the κ-th electron. A complex absorbing potential V_{cap} is optionally included to damp reflections from the boundaries. The electron-electron interaction is the Coulomb potential, $V_{12}(|\vec{r}_\kappa - \vec{r}_\lambda|) = |\vec{r}_\kappa - \vec{r}_\lambda|^{-1}$ in 3 dimensions and some screened version in 1D models, e.g. $V_{12}(|z_\kappa - z_\lambda|) = 1/\sqrt{(z_\kappa - z_\lambda)^2 + a^2}$ with a screening parameter a.

Equations (3.19a) and (3.19b) can be further transformed by splitting the Hamiltonian into a single- and a two-particle part:

$$H = H^{(1)} + H^{(2)}. \tag{4.3}$$

where $H^{(1)}$ is a sum of single-particle operators

$$H^{(1)} = \sum_{\kappa=1}^{f} h(q_\kappa; t) \tag{4.4}$$

and

$$H^{(2)} = \sum_{\kappa=1}^{f} \sum_{\lambda=\kappa+1}^{f} V_{12}(q_\kappa, q_\lambda). \tag{4.5}$$

Accordingly, we can split $\boldsymbol{K}$ (3.24) into a one- and two-particle contribution, with

$$(\boldsymbol{K}_1 \boldsymbol{B})_{j_1 \cdots j_f} = \sum_{k=1}^{n} \sum_{\lambda=1}^{f} h_{j_\lambda k} B_{j_1 \cdots j_\lambda \to k \cdots j_f}, \tag{4.6}$$

where we have introduced the single-particle matrix elements $h_{j_\lambda k} = \langle \phi_{j_\lambda} | h | \phi_k \rangle$. The lhs is calculated for the $\binom{n}{f}$ ordered f-tuples $j_1 < \cdots < j_f$. The notation $j_1 \cdots j_\lambda \to k \cdots j_f$ means that the index j_λ is replaced with k. Due to antisymmetry of the B's there are at most $n - f + 1$ non-vanishing terms in the rhs sum over k, which gives a count of $\binom{n}{p} \times \binom{n-f+1}{1} \times \binom{f}{1} \ll n^f$ multiplications. Similarly we have

$$(\boldsymbol{K}_2 \boldsymbol{B})_{j_1 \cdots j_f} = \sum_{\kappa=1}^{f} \sum_{\kappa<\lambda}^{f} \sum_{k=1}^{n} \sum_{k<l}^{n} (H_{j_\kappa j_\lambda k l} - H_{j_\kappa j_\lambda l k}) B_{j_1 \cdots j_\kappa \to k \cdots j_\lambda \to l \cdots j_f} \tag{4.7}$$

with a corresponding multiplication count of $\binom{n}{f} \times \binom{n-f+2}{2} \times \binom{f}{2}$. For systems of only a few fermions and moderate correlation – which holds for a large class of chemical systems – all these numbers remain small and constitute only a small fraction of computational effort.

Inserting $H^{(1)}$ into (3.22) yields

$$H^{(1)}_{lk} = h(q_1; t) \rho_{lk} + \underbrace{(f-1) A^*_{l m j_3 \cdots j_f} A_{k p j_3 \cdots j_f} \langle \phi_m \mid h \mid \phi_p \rangle}_{Q_{lk}} \tag{4.8}$$

In the working equation, the last term appears as $Q_{lk}\phi_k$, which is annihilated by the projector $(1 - P)$. Similarly, we get

$$H^{(2)}_{lk} = (f-1) B^*_{l r j_3 \cdots j_f} B_{k s j_3 \cdots j_f} \langle \phi_r \mid V_{12}(q_1, q_2) \mid \phi_s \rangle + Q_{lk} \tag{4.9}$$

where the last term again drops out of the working equations.

4.2 Spin

When we consider systems without spin forces, spin is strictly conserved. Rather than explicitly enforcing a given spin symmetry, all spin states are propagated and redundant operations are bypassed in the code. For the orbitals we choose single spin eigenfunctions and set all one-particle integrals for orbitals with different spins and all mean-field operators that would connect different spins equal to 0. For simplicity, some redundancy is admitted in the evaluation of the rhs of (3.25a).

With this approach, we do not need to distinguish "unrestricted" Hartree-Fock from the mostly employed "restricted" scheme, where orbitals are subjected to the constraint that their spatial parts must either be identical or orthogonal. Our only fundamental requirement is orthogonality of the orbitals including the spin coordinate. In Multi-Configuration Hartree-Fock this distinction loses much of its relevance, as any unrestricted scheme can be accommodated within a larger restricted scheme with comparable computational effort, by simple splitting the spatial orbitals into mutually orthogonal parts. In practice, we mostly use the restricted version employing orbitals with pairwise identical spatial parts and – again – avoiding redundant operations.

For obtaining an initial state with spin quantum numbers S and S_z by imaginary time propagation it is sufficient to start from a guess state with quantum numbers S, S_z. We first construct a set of orbitals $\boldsymbol{\phi}$, usually with the eigenfunctions of some single-particle Hamiltonian for the spatial part. A suitable guess coefficient vector $\boldsymbol{B}_{SS_z}$ is obtained by projection onto the subspace with the desired spin:

$$\boldsymbol{B}_{SS_z} = P_S Q_{S_z} \boldsymbol{B}. \tag{4.10}$$

A straightforward way of constructing the projection operators P_S and Q_{S_z} for small numbers of orbitals is by diagonalizing the $\binom{n}{f} \times \binom{n}{f}$ spin matrices

$$S_{JL} = \langle \Phi_J | S^2 | \Phi_L \rangle \quad \text{and} \quad M_{JL} = \langle \Phi_J | S^2 | \Phi_L \rangle. \tag{4.11}$$

Here one must make sure that the matrices $\boldsymbol{S}$ and $\boldsymbol{M}$ commute, that is that the determinants Φ_J cover complete spin subspaces, e.g. by starting from a maximal set of all doubly occupied spatial orbitals.

4.3 Spatial discretization

For our model application of laser-driven molecules there is no single coordinate system that allows an efficient separation of the single-particle functions: near the nuclei spherical symmetry dominates, but for detached electrons in a linearly polarized field cylindrical coordinates are most appropriate. To maintain the highest possible flexibility, in the present code, we represent the single particle functions on a 3-dimensional product basis of one-dimensional finite-element (FE) functions. Within this scheme we can implement any kind of coordinate system. For the applications presented in this thesis, either cylindrical or 1D Cartesian coordinates were used.

The FE framework offers superior flexibility over other formulations, which comprise global basis sets (spectral methods) on the one hand, and other local methods, such as finite differences and discrete variable representation (DVR) on the other hand. This flexibility comes in especially handy for our target applications.

At typical laser parameters, the ionization of bound systems ranges from a few percent to total depletion, so that a large fraction of the system is in continuum states. To accurately represent bound states near the nuclei, a finer discretization is required than for the free motion in the laser field. By contrast, hard electron-electron

collisions are unimportant for continuum electrons and the short-range behavior of the Coulomb repulsion is not as critical as near the nuclei. Therefore for both the electron orbitals and the electron-electron interaction the finite-element discretization allows to tune the size of the finite elements in a position-dependent way. In cases where the dynamics remains mostly within the bound-state regime, Gaussian functions were successfully employed [38]. There are further technical reasons for using FEs. Accurate integrations near the singularities of the potentials require transformations to denser quadrature grids, which can be easily administered with local functions. Local representations of all operators, including the differential operators, are also needed for efficient parallelization.

We use FEs of arbitrary order as described in [84]. A given coordinate q is split into intervals $[q_{n-1}, q_n]$ and the finite elements are completely defined by the type and number of approximation functions $g_{nk}^{(q)}(q), k = 0, \ldots, K$ on that interval. The only requirement for the $g_{nk}^{(q)}$ is that

(i) they be differentiable once,

(ii) that they can be linearly re-combined such that they all vanish at the endpoints of the of the FE, except for two of them: these are non-zero at the lower and upper boundary, respectively,

$$g_{nK}^{(q)}(q_n) = g_{n0}^{(q)}(q_{n-1}) = 1, \text{ else} \tag{4.12a}$$

$$g_{nk}^{(q)}(q_{n-1}) = g_{nk}^{(q)}(q_n) = 0. \tag{4.12b}$$

A spatial orbital in 3 dimensions is written as

$$\phi(r,s,t) = \sum_{l,m,n} \sum_{i,j,k} c_{lmn,ijk}\, g_{li}^{(r)}(r) g_{mj}^{(s)}(s) g_{nk}^{(t)}(t) \tag{4.13}$$

The sums extend over all "voxels", i.e. triplets of 1-dimensional elements (l, m, n), and over all functions (i, j, k) on each voxel.

Neighboring voxels are connected by the requirement of continuity at q_n, which translates into a linear constraint on the single-particle function expansion coefficients, e.g. for the t-coordinate

$$c_{lm(n-1),ijK} = c_{lmn,ij0}. \tag{4.14}$$

Note that for the discretization of differential operators up to the second order, continuity of the derivative is not required: formally a δ-like second derivative appears, but it is always integrated over with a continuous function. Dirichlet boundary conditions can be implemented by setting the desired values for the first coefficient of the first element and the last coefficient of the last element, respectively.

Any set of linearly independent functions with suitable continuity properties and boundary values can be used to represent the solution within one element. General global bases are included as limiting cases in this scheme, when a single element covers the whole coordinate range. To obtain a (global) DVR of the basis, one transforms it

such that it diagonalizes the coordinate operator. Our FE scheme also includes the case of the so-called FE-DVR method [78], where polynomial finite element functions are represented by their values at the quadrature points of a Lobatto scheme which includes the points at the element boundaries. This allows an easy implementation of continuity conditions. The same Lobatto quadrature can be employed for most integrations, if one makes minor compromises on the quadrature error.

For the implementation, in particular for parallelization, it is convenient to formulate the continuity condition for coordinate q at boundary q_n with the help of a projection operator $\widehat{\boldsymbol{Q}}_n^{(q)}$

$$\widehat{\boldsymbol{Q}}_n^{(q)} = \mathbb{1} - \widehat{\boldsymbol{P}}_n^{(q)} = \mathbb{1} - |d_n\rangle\langle d_n| \tag{4.15}$$

which acts on the coefficients $\boldsymbol{c}$. The "discontinuity vector"

$$\langle d_n| = \frac{1}{\sqrt{2}}(\ldots, 0, 0, -1, 0, \ldots, 0, 1, 0, 0, \ldots) \tag{4.16}$$

has the values -1 and $+1$ at the position of the pairs of coefficients that need to be identical for continuity at q_n. The projector ensuring continuity at all element boundaries on coordinate q is given by

$$\widehat{\boldsymbol{Q}}_n^{(q)} = \prod_n (\mathbb{1} - \widehat{\boldsymbol{P}}_n^{(q)}) = \mathbb{1} - \sum_n \widehat{\boldsymbol{P}}_n^{(q)} =: \mathbb{1} - \widehat{\boldsymbol{P}}^{(q)} \tag{4.17}$$

The second equality holds because of the mutual orthogonality of the projectors $\widehat{\boldsymbol{P}}_n^{(q)}\widehat{\boldsymbol{P}}_m^{(q)} = 0$ for $n \neq m$. A coefficient vector for a continuous function in 3D is obtained from an arbitrary coefficient vector $\boldsymbol{c}$ by applying the projectors for all three directions

$$\boldsymbol{c}^{\text{cont}} = \widehat{\boldsymbol{Q}}^{(r)}\widehat{\boldsymbol{Q}}^{(s)}\widehat{\boldsymbol{Q}}^{(t)}\boldsymbol{c} =: \widehat{\boldsymbol{Q}}\boldsymbol{c} \tag{4.18}$$

In our model applications we need very large grids: the oscillation amplitude of the free electrons in typical fields may reach several tens of atomic units. Some of the most prominent strong field phenomena like high-harmonic generation or non-sequential double ionization occur only when electrons return to the molecule. During the excursion, electron kinetic energies can reach several atomic units. For a proper representation of the momentum and excursion of the electrons, we need a typical number of 500 discretization points in the polarization direction of the laser and at least several tens of points in the perpendicular direction. Even when we only admit cylindrically symmetric orbitals, we obtain on the scale of 10^4 discretization points per orbital. In spite of the large extension of the simulation box, large parts of the wave function may reach the box boundaries and need to be absorbed. For this we employ complex absorbing potentials V_{cap}. Mostly, CAPs are of the general form $V_{\text{cap}}(\vec{r}) = -\mathrm{i}\,W(\vec{r})$ with a real positive function W, although CAPs with real parts have also been suggested [33]. Absorption must be strong enough to blot out all outgoing parts of Ψ within a reasonably short distance in order to keep the box size

as small as possible. At the same time, reflections of the wave function from the CAP itself have to be minimized. The problem is compounded by the fact that absorption and reflection depend on the wavelength of the incident electrons, which generally span a wide range of energies. The search for optimized CAPs has led to a large number of different expressions for W that have been investigated in the literature [79, 64, 101]. In the calculations presented in this thesis, we employ the following CAP with empirically determined parameters:

$$W(z,\rho) = W_z(z)W_\rho(\rho) \tag{4.19}$$

$$W_q(q) = \begin{cases} 0, & |q| < q_0 \\ \dfrac{C_q}{2}\left[1 - \cos\left(\dfrac{\pi}{L_q}(q - q_0)\right)\right], & q_0 < |q| < q_0 + L_q \\ C_q, & q_0 + L_q < |q|. \end{cases} \tag{4.20}$$

The distribution of the FE boundaries can be adjusted to the specific physical system. At large distances electron momenta are predictably lower, while the highest momenta appear in the surroundings of the original bound system. Unnecessary stiffness of the discretized equations results, when the sum of potential and kinetic energies locally present in the discretization significantly exceeds the energies in the actual solution: a dense grid near a negative potential singularity does not significantly impact on the stiffness of the system, but the same density in regions of zero potential may severely slow down time-propagation.

Stiffness of a differential equation means that explicit methods for solving the equation are numerically unstable, unless the step size is taken to be extremely small. In practice, given a system of ODEs, one linearizes it,

$$\dot{\boldsymbol{y}} = \boldsymbol{f}(\boldsymbol{y}, t) \approx J(\boldsymbol{y}, t)\boldsymbol{y}, \tag{4.21}$$

which implies

$$\dot{\boldsymbol{y}}_{t+\Delta t} \approx \Big[1 + \Delta t J(\boldsymbol{y}_t, t) + O(\Delta t^2)\Big]\boldsymbol{y}_t. \tag{4.22}$$

The linear problem is generally considered to be stiff if the Jacobian J has eigenvalues of unnecessarily large absolute value, which are not present in the actual solution $\boldsymbol{y}$. This is because then the step size Δt must be chosen small in order that the linearization $[1 + \Delta t J]$ approximates the correct exponential $\mathrm{e}^{\Delta t J}$ in a reasonable way. In our case, J corresponds to the single-electron Hamiltonian $H \sim T + V$. Large eigenvalues can arise from the kinetic energy by too fine discretization, which, however, will be offset when there is a large, negative potential.

Variable grids therefore have the twofold advantage of a significantly lower number of grid points and fewer stiffness related problems.

4.4 One-particle operators

With a FE product basis, the total single-particle Hamiltonian can be written as sum over "voxel" Hamiltonians

$$h\boldsymbol{c} = \widehat{Q} \sum_v h^{(v)} \widehat{Q} \boldsymbol{c} \tag{4.23}$$

for the volumes $[r_l, r_{l+1}] \times [s_m, s_{m+1}] \times [t_n, t_{n+1}]$ with $v = (l, m, n)$. Assuming locality of h, the voxel discretization is diagonal with respect to the voxel index v, except for overlaps between neighboring voxels introduced by the continuity constraint $\widehat{Q}$. The time-independent parts of $h^{(v)}$ are computed during an initial setup stage. The $h^{(v)}$ are in general full matrices, but their tensor product structure is exploited wherever possible. For example, the Laplacian in Cartesian coordinates is a sum of three tensor products,

$$\Delta = \partial_x^2 \otimes \mathbb{1} \otimes \mathbb{1} + \mathbb{1} \otimes \partial_y^2 \otimes \mathbb{1} + \mathbb{1} \otimes \mathbb{1} \otimes \partial_x^2. \tag{4.24}$$

The matrix elements of such a 3D tensor product operator $\mathcal{O} = \mathcal{O}_x \otimes \mathcal{O}_y \otimes \mathcal{O}_z$ on one voxel can be factorized as

$$\langle li, mj, nk|\mathcal{O}|li', mj', nk'\rangle = \langle li|\mathcal{O}_x|li'\rangle \langle mj|\mathcal{O}_y|mj'\rangle \langle nk|\mathcal{O}_z|nk'\rangle. \tag{4.25}$$

For a basis set of size $L = L_x L_y L_z$, the full matrix application costs L^2 operations, while the factorized form only $L_x^2 L_y L_z + L_x L_y^2 L_z + L_x L_y L_z^2 = (L_x + L_y + L_z)L$. For a typical calculation in cylindrical coordinates, e.g. $L_z = 500$ and $L_\rho = 20$, factorization reduces the operations count from $L^2 = 10^8$ to $(L_z + L_\rho)L = 5.2 \times 10^6$ by about a factor of 20.

Potentials are applied by transformations to quadrature grids, which again have tensor product form. Thus, the matrix element $\langle li, mj, nk|V|li', mj', nk'\rangle$ is calculated as

$$\begin{aligned}
\langle li, mj, nk|V|li', mj', nk'\rangle = &\int \mathrm{d}r\, \mathrm{d}s\, \mathrm{d}t\, g_{li}^{(r)}(r)\, g_{mj}^{(s)}(s) g_{nk}^{(t)}(t) \times \\
&V(r,s,t) g_{li'}^{(r)}(r) g_{mj'}^{(s)}(s) g_{nk'}^{(t)}(t) \\
\approx &\sum_{\rho=1}^{N_r} \sum_{\sigma=1}^{N_s} \sum_{\tau=1}^{N_t} g_{li}^{(r)}(r_\rho) g_{mj}^{(s)}(s_\sigma) g_{nk}^{(t)}(t_\tau) \times \\
&V(r_\rho, s_\sigma, t_\tau) g_{li'}^{(r)}(r_\rho) g_{mj'}^{(s)}(s_\sigma) g_{nk'}^{(t)}(t_\tau) \\
\equiv &\, g_{i\rho}^{(r,l)} g_{j\sigma}^{(s,m)} g_{k\tau}^{(t,n)} V_{\rho\sigma\tau} [g^{(r,l)}]_{\rho i'}^T [g^{(s,m)}]_{\sigma j'}^T [g^{(t,n)}]_{\tau k'}^T,
\end{aligned} \tag{4.26}$$

where r_ρ, s_σ, t_τ are the quadrature points, which are determined once during setup. Only near the singularities of non-separable potentials, where one would need large product grids for accurate quadrature and correspondingly expensive transformations,

all single-electron terms are united in a full 3-dimensional voxel matrix $h^{(v)}$. The computationally optimal crossover point between the methods is determined during setup by measuring the CPU time needed for application of $h^{(v)}$ in either form.

When solving the single-particle equations in FE discretization one obtains equations of the form

$$S\mathrm{i}\,\frac{\mathrm{d}}{\mathrm{d}t}\boldsymbol{c} = h\boldsymbol{c} \tag{4.27}$$

where

$$S := \widehat{Q}S_0\widehat{Q} = \widehat{Q}\sum_v S^{(v)}\widehat{Q} \tag{4.28}$$

is the overlap matrix, with the voxel overlap matrices $S^{(v)} = S^{(r,l)} \otimes S^{(s,m)} \otimes S^{(t,n)}$ and

$$S^{(q,i)}_{kk'} = \langle h^{(q)}_{i,k} | h^{(q)}_{i,k'} \rangle, (q,i) = (r,l),(s,m),(t,n). \tag{4.29}$$

A parallelizable method for computing $S^{-1}h\boldsymbol{c}$ is described below.

4.5 Two-particle operators

The fact that the interaction is in general singular at the point of coalescence, that it may be long range, and that we are dealing with very extended orbitals poses great computational challenges.

As exemplified in sec. 2.3, a brute force application of V_{12} is computationally utopian. With the single-particle grid size on the scale of a few thousand, the exact discretization of the two-particle operators would lead to matrix sizes of several millions. For polynomial FE functions, the size of the exact discretization for two-particle operators can be strongly reduced but always remains significantly larger than the dimension of the single-particle space. This is usually much too large to even calculate the discretization of V_{12}, let alone apply it in each time step. We therefore approximate the interaction potential in three stages by

(i) representing it on a coarse grid that is adjusted to the physical problem in question,

(ii) factorizing it by the H-matrix technique, and

(iii) making a locally weighted low-rank approximation of the H-matrix.

4.5.1 Representation of V_{12} on a coarse grid

As electron-electron interactions near the nuclei are more important, we choose a FE discretization of V_{12} with high accuracies only in the vicinity of the molecule and much coarser grids outside. In addition, the order of the FE representation can be chosen mostly lower than the order of the FE on the orbitals. For efficient quadrature it is advantageous if the FE boundaries for V_{12} are a subset of those for the orbitals.

For a given FE basis the interaction potential is

$$V_{12}(q_1, q_2) \approx \sum_{v,v'} G_v(q_1)(S^{-1}V_{12}S^{-1})_{vv'}G_{v'}(q_2) =: \boldsymbol{G}(q_1)\boldsymbol{W}\boldsymbol{G}^T(q_2) \quad (4.30)$$

where $v = (lmn, ijk)$ and $v' = (l'm'n', i'j'k')$ label the FE product functions $G_v(q) = g^{(r)}_{li}(r)g^{(s)}_{mj}(s)g^{(t)}_{nk}(t)$. The matrix

$$(V_{12})_{vv'} = \int \mathrm{d}q_1 \mathrm{d}q_2 \, G_v(q_1)V_{12}(q_1, q_2)G_{v'}(q_2) \quad (4.31)$$

is the discretized potential matrix and S the overlap matrix (4.28). As we are approximating a multiplication operator, we do not need to enforce continuity across element boundaries. This has the technical advantage of a strictly local overlap matrix S which is easily inverted or diagonalized. It has the additional benefit of maintaining voxel-wise locality also after application of S^{-1}, which is important for the H-matrix technique discussed in the following section.

4.5.2 H-matrix representation

For an efficient computation of the two-particle integrals, it is advantageous to bring V_{12} to the form

$$V_{12}(q_1, q_2) \approx \sum_{m=1}^{M} U_m(q_1)w_m V_m(q_2), \quad (4.32)$$

where the functions U_m and V_m and the numbers w_m can be assumed to be real. From (4.30) one readily obtains one such representation with the help of the eigenvectors $\boldsymbol{W}\boldsymbol{u}_m = \boldsymbol{u}_m w_m$, so that

$$V_{12}(Q_1, Q_2) \approx \sum_{m=1}^{M} (\boldsymbol{u}_m \cdot \boldsymbol{G}(q_1))w_m(\boldsymbol{u}_m \cdot \boldsymbol{G}(q_2)). \quad (4.33)$$

In this particular case the left and right functions are identical $U_m = V_m = \boldsymbol{u}_m \cdot \boldsymbol{G}$. For eigenvalues sorted by decreasing modulus $|w_1| > |w_2| > \cdots$ this so-called Schmidt decomposition constitutes the L^2-optimal approximation to (4.30) for a given rank M. Another well-known example of such a decomposition is the multipole expansion of the Coulomb potential.

Both the Schmidt decomposition and the multipole expansion have global functions U_m and V_m, which makes each term in the sum (4.32) a non-local operator. A systematic way of generating *localized* factor functions and take advantage of local smoothness in V_{12} is by hierarchical matrices (H-matrices) [30]. This technique relies on the fact that almost any two-particle interaction will be diagonally dominated and increasingly smooth far from the diagonal. This is best illustrated by the Coulomb potential, where for $|\vec{r}_1| \ll |\vec{r}_2|$ a few terms of the multipole expansion suffice for an

accurate description of the interaction. If we choose a discretization (like finite elements) that to some extent preserves locality properties, this factorization into a few products carries over to the discrete matrix. The strategy is to first approximate large off-diagonal blocks of the interaction by a few products and than repeat the procedure for smaller blocks that are closer to the diagonal. One thus obtains hierarchy of matrix blocks, which each can be approximated by a low-rank matrix, until one reaches the diagonal elements (cf. fig. 4.1). The sum of the ranks of all blocks of this decomposition, i.e. the number of terms in (4.32) will in general be larger than the rank of a Schmidt decomposition of comparable accuracy, however, due to the small size of the majority of the individual blocks, the operations count for applying the H-matrix approximation can be much smaller.

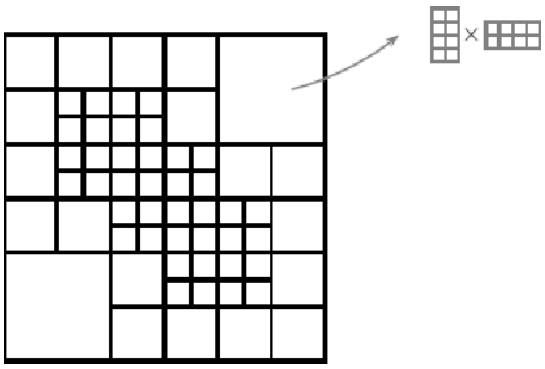

Figure 4.1: Schematic representation of a partitioning of the two-particle potential. Partitioning is denser near the center of coordinate space by an a priori choice of discretization. The discrete matrix is divided into blocks that are smaller near the diagonal. The off-diagonal blocks allow efficient low-rank approximation.

Let us demonstrate the working principle of the H-matrix decomposition on some small examples. Given an $L \times L$-matrix $\boldsymbol{A}$, we can write it in the same form as (4.32) by using the singular value decomposition (SVD),

$$\boldsymbol{A} = \sum_{j=1}^{L} \sigma_j \boldsymbol{u}_j \otimes \boldsymbol{v}_j^\dagger. \tag{4.34}$$

with the singular values σ_j. If $\boldsymbol{A}$ is diagonalizable, $\boldsymbol{u}_j = \boldsymbol{v}_j$, and σ_j are the eigenvalues. In this form, we see that the computational cost of applying $\boldsymbol{A}$ can be reduced in two ways: (a) by reducing the number of vectors, i.e. the rank of the matrix, (b) by reducing the length of each vector. The first goal can easily be achieved by truncating the SVD for singular value $\sigma_j < \epsilon$. The latter goal is more tricky and depends on the structure of the matrix.

Consider first a block-diagonal matrix

$$\boldsymbol{A} = \begin{pmatrix} \boldsymbol{C} & 0 \\ 0 & \boldsymbol{D} \end{pmatrix} \tag{4.35}$$

where $\boldsymbol{C}$ and $\boldsymbol{D}$ are $L/2 \times L/2$. The eigenvectors of $\boldsymbol{A}$ have the form $(\boldsymbol{u}_C, 0)^T$ and $(0, \boldsymbol{u}_D)$, respectively. The operations count can hence be reduced from N^2 to $2 \times (N/2)^2 = N^2/2$ by skipping the known zero entries when applying the vectors.

Consider now a slightly perturbed diagonal matrix

$$\boldsymbol{A} = \begin{pmatrix} 1 & 0 & \alpha & \beta \\ 0 & 1 & \gamma & \delta \\ \alpha & \gamma & 1 & 0 \\ \beta & \delta & 0 & 1 \end{pmatrix} = \begin{pmatrix} \mathbb{1} & \boldsymbol{\mathcal{E}} \\ \boldsymbol{\mathcal{E}} & \mathbb{1} \end{pmatrix} \tag{4.36}$$

and assume that the eigenvalues of $\boldsymbol{\mathcal{E}}$ are smaller than our required accuracy. Diagonalizing the full matrix, we obtain eigenvalues $\lambda \sim 1$, and eigenvectors with no obvious zero entries. Thus, we cannot simply truncate the SVD, nor can we neglect parts of the eigenvectors. However, if we factorize the matrix into blocks, and consider the SVD for each of them separately, we can, within our accuracy requirements, neglect the $\mathcal{E}$-blocks completely.

We use the H-matrix decomposition to bring the two-particle interaction into the form (4.32). As in our case the rank of the approximation, i.e. the number of terms in the sum, affects the operations count for the computation of the matrix $\boldsymbol{K}_2$, we set a lower limit to the block-size of the H-matrix decomposition.

As a last fine-tuning of the approximation, we choose different approximation accuracies for H-matrix blocks depending on their importance for the physical process. This is in spirit similar to the initial choice of a coarser FE grid. However, it provides additional flexibility as it can be made on the two-particle space rather than on the single-particle coordinates. In addition, it is more systematic as the neglected terms can be directly related to the L^2-error of the approximation.

4.6 Parallelization

On distributed memory machines, the key to efficient large-scale parallelization are locality and synchronization. In our typical applications using Hamiltonian (4.1), the main compute load is on the orbitals for which locality of differential and multiplication operators translates into data locality, if one distributes the spatial part of each orbital over the compute nodes. Application of the projector $\widehat{Q}$ for wave function continuity then involves only nearest-neighbor communication. Somewhat more involved is the application of a non-diagonal FE inverse overlap matrix S^{-1}, which we discuss below. The most challenging part is the parallel computation of the mean field potentials, as the two-particle interactions are fundamentally non-local. However, strong interactions usually occur over a short range, i.e.. locally, while the long-rang part of the interaction is well described by low-rank approximations. With the H-matrix decomposition we

have already taken advantage of such a structure. Below we show how the H-matrix structure can be used for parallelization.

For simplicity, we assume that only the most extended coordinate is distributed over compute nodes. For our model systems, this is usually the z-coordinate. The z-axis is split at some finite element boundaries and each chunk is assigned to a different compute node. In the MCTDHF applications so far, the coefficient vector B_J is comparatively small and does not require parallelization.

Fig. 4.2 summarizes the work flow of our parallelized MCTDHF implementation. Starting from a set of old orbitals $\boldsymbol{\phi}$ and coefficients $\boldsymbol{B}$, we calculate the mean fields $\boldsymbol{H}$, which requires communication across all nodes. Applying the mean fields and the single-particle operators in the equations of motion, we compute new coefficients $\boldsymbol{B}$ and provisional new orbitals $\boldsymbol{\phi}$. The latter are then subjected to the continuity condition, which requires mostly nearest-node communication. This procedure is repeated at each time step.

4.6.1 Application of the inverse overlap matrix S^{-1}

With high-order FE methods the inverse overlap matrix can be approximately transformed to the unit matrix by local transformations. However, the exact overlap matrix can also be applied with only little extra inter-node communication. One reason why one may want to make this small effort is to maintain the variational property of the FE discretization.

For solving an equation of the form (4.27) we must invert the matrix S in the subspace of $\widehat{Q}$. For that purpose, we use the identity

$$S^{-1} = (\widehat{Q}S_0\widehat{Q})^{-1} = \widehat{Q}S_0^{-1}\widehat{Q} - \widehat{Q}S_0^{-1}\widehat{P}(\widehat{P}S_0^{-1}\widehat{P})^{-1}\widehat{P}S_0^{-1}\widehat{Q} \tag{4.37}$$

which holds for any pair of mutually orthogonal projectors $\widehat{P} + \widehat{Q} = \mathbb{1}$. The inversion is to be understood in the sense

$$(\widehat{Q}S_0\widehat{Q})^{-1}\widehat{Q}S_0\widehat{Q} = \widehat{Q} \tag{4.38}$$

and analogous for $(\widehat{P}S_0^{-1}\widehat{P})^{-1}$. The advantage of replacing the inversion of $\widehat{Q}S_0\widehat{Q}$ with the inversion of $\widehat{P}S_0^{-1}\widehat{P}$ lies in the fact that the number of $\widehat{P}_n{}'s$ that connect coefficients on different compute nodes is much smaller than the dimension of $\widehat{Q}$, which equals the number of independent coefficients in z-direction. Only this small number of coefficients needs to be exchanged in an all-to-all type of communication.

4.6.2 Parallel computation of mean fields

With a factorization of the form (4.32) the computation of the integrals can be split into three steps. First the single-particle factor integrals calculated locally

$$U_{mik,\nu} = \langle \phi_i \mid U_m \mid \phi_k \rangle_\nu, \tag{4.39}$$

where the subscript ν indicates that integrations are restricted to the ν-th compute node. This integration needs to be done only for U_m, as due to the exchange-symmetry

of the two-particle operator, for each m there is an m' such that $W_{mik} = U_{m'ik}$. The integrals are then added up over all nodes ν where $U_m(q)$ has non-vanishing support

$$U_{mik} = \sum_\nu U_{mik,\nu}. \tag{4.40}$$

With an H-matrix partitioning as sketched in fig. 4.1 many U_m have their support only on a single node and require no summation and no communication in this step, and a large number of m's involves only two or a few nodes causing little communication. After summation of the integrals they are distributed to those nodes that compute separate parts of the $\boldsymbol{K}$-matrix and the mean-field potentials. Finally, the application of the mean field potentials is strictly local and multiplication of $\boldsymbol{B}$ by the distributed $\boldsymbol{K}$ matrix requires all-to-all communication of the coefficient vector $\boldsymbol{B}$, which has moderate size.

4.6.3 Dynamic load balancing

Synchronization is deteriorated by imbalance of the compute load introduced by the strong spatial variation of the potentials and the spatial weighting of the H-matrix decomposition. The exact load distribution is difficult to predict a priori. For typical applications, we have observed load imbalances of 50% or more with a corresponding loss in scalability. We have therefore implemented a scheme where self-timing of the code is used to re-distribute the load over the processors.

Dynamic load balancing causes little overhead as imbalances originate in the time-independent part of the operators and only few adjustments occur after the initial establishment of a balanced distribution.

4.7 Measuring correlation

As mentioned in sec. 3.1, the coefficients in the MCTDHF wave function expansion (3.1) are not unique as we can make a change of bases by a unitary matrix $\boldsymbol{U}(t)$. We can however arrive at a unique representation by considering the one-particle density matrix

$$\rho^{(1)}(q,q') := \int \mathrm{d}q_2 \cdots \mathrm{d}q_f \, \Psi(q,q_2,\ldots,q_f)\Psi^*(q',q_2,\ldots,q_f) \tag{4.41}$$

which becomes, on inserting (3.1),

$$\begin{aligned} \rho^{(1)}(q,q') &= B_{jj_2\cdots j_f} B^*_{kk_2\cdots k_f} \phi_j(q)\phi^*_k(q') \\ &= \rho^{(1)}_{jk}\phi_j(q)\phi^*_k(q'). \end{aligned} \tag{4.42}$$

(Note that $\rho^{(1)}_{jk}$ is defined with exchanged indices as compared to (3.20).) Since $\rho^{(1)}_{jk}$ is a hermitian matrix, we can diagonalize it, such that

$$\rho^{(1)}(q,q') = \sum_j p_j \tilde{\phi}_j(q)\tilde{\phi}^*_j(q'). \tag{4.43}$$

The new $\widetilde{\phi_j}$ are called the *natural orbitals* [58], which are unique (except if some eigenvalues p_j are degenerate) for each Ψ and are the eigenfunctions of the one-particle density operator

$$\hat{\rho}^{(1)} = \mathrm{Tr}_{q_2,\ldots,q_f}(|\Psi\rangle\langle\Psi|). \tag{4.44}$$

The real eigenvalues p_j are called the natural populations. The rate at which the natural populations drop off in magnitude serves as a measure for the degree of correlation. For each natural orbital, the corresponding eigenvalue indicates how significant are the contributions of the configurations where the orbital participates to the total wave function. For an f-electron Hartree-Fock wave function $p_j = 1, j = 1, \ldots, f$ and $p_j = 0, j > f$, i.e. each of f orbitals is equally important, since there is only one configuration. For a strongly correlated wave function, more than f orbitals are necessary and their populations would only slowly go to zero. Using the natural orbitals as a basis set in the expansion (3.1) is optimal insofar as it allows to represent any wave function with the minimum number for orbitals for a given error (in the L^2-sense).

4.8 Observables

4.8.1 Projections onto multi-particle states

The overlap between two multi-particle wave functions constructed from the same orthonormal set of orbitals is obtained from the inner product of the two coefficient vectors. For the calculation of overlaps with different sets of orbitals, e.g. the autocorrelation function $\langle\Psi(0) \mid \Psi(t)\rangle$, one can take advantage of antisymmetry by observing that

$$\begin{aligned}\langle\Psi_b \mid \Psi_c\rangle &= \sum_{j_1\cdots j_f}\sum_{l_1\cdots l_f} B^*_{j_1\cdots j_f}\Big(\prod_{\kappa=1}^{f}\mathcal{O}_{j_\kappa l_\kappa}\Big)C_{l_1\cdots l_f} \\ &= f!\sum_{j_1<\cdots<j_f}\sum_{l_1<\cdots<l_f} B^*_{j_1\cdots j_f}C_{l_1\cdots l_f}\det(\mathcal{O}^{l_1\cdots l_f}_{j_1\cdots j_f}),\end{aligned} \tag{4.45}$$

where $\mathcal{O}_{jk} = \langle\phi^b_j \mid \phi^c_k\rangle$ and

$$\mathcal{O}^{k_1\cdots k_f}_{j_1\cdots j_f} := \begin{pmatrix}\mathcal{O}_{j_1k_1} & \cdots & \mathcal{O}_{j_1k_f}\\ \vdots & & \vdots \\ \mathcal{O}_{j_pk_1} & \cdots & \mathcal{O}_{j_pk_f}\end{pmatrix} \tag{4.46}$$

denotes the submatrix of the overlap matrix for the respective left and right index sets.

4.8.2 One- and two-particle

For a system of indistinguishable particles the general form of a one-particle observable X is the sum of one operator in the single-particle space over all single-particle

coordinates

$$X(q_1, \ldots, q_f) = \sum_{\kappa=1}^{f} x(q_\kappa). \tag{4.47}$$

For example, the dipole moment operator is $d_z = \sum_{\kappa=1}^{f} z_\kappa$. The expectation value of X with an MCTDHF wave function Ψ is therefore just f times the expectation value for the first particle

$$\langle \Psi \mid X \mid \Psi \rangle = f \sum_{k=1}^{n} \sum_{l=1}^{n} X_{kl} \sum_{j_2 \cdots j_f} B^*_{kj_2\cdots j_f} B_{lj_2\cdots j_f} =: f \operatorname{Tr}(\boldsymbol{\rho X}), \tag{4.48}$$

where $\boldsymbol{X}$ denotes the matrix $X_{jl} = \langle \phi_j \mid x \mid \phi_l \rangle$ and $\boldsymbol{\rho}$ is the single-particle density matrix.

Two-particle observables have the general form

$$Y = \sum_{\kappa,\lambda=1}^{f} y(q_\kappa, q_\lambda). \tag{4.49}$$

Analogous to single-particle expectation values, general two-particle expectation values can be written as

$$\langle \Psi | Y | \Psi \rangle = f^2 \operatorname{Tr}(\boldsymbol{Y\sigma}), \tag{4.50}$$

where we have introduced the two-particle density-matrix

$$\sigma_{kl,mn} = \sum_{j_3 \cdots j_f} B^*_{klj_3\cdots j_f} B_{mnj_3\cdots j_f} \tag{4.51}$$

and the matrix $Y_{kl,mn} = \langle \phi_k \phi_l | y | \phi_m \phi_n \rangle$.

4.8.3 All-particle observables

The scheme set up above for one- and two-particle observables can be generalized to many-particle observables. One such observable that involves all particles is the probability of single or multiple ionization, which we define as the probability of finding – at large times – any m particles *outside* some binding area A, while the remaining particles are *inside* this area.

The corresponding operator is

$$Z_m = \sum_{T_m} \prod_{\kappa \in T_m} O_A(q_\kappa) \prod_{\lambda \notin T_m} P_A(q_\lambda) \tag{4.52}$$

where T_m extends over all m-element subsets of $\{1, \ldots, f\}$,

$$O_A(q) = \begin{cases} 0 & \text{for } Q \in A \\ 1 & \text{else} \end{cases} \tag{4.53}$$

and $P_A = 1 - O_A$ (i.e. the characteristic function of A). The expectation value for this

f-particle operator is

$$\langle \Psi \mid Z_m \mid \Psi \rangle = f! \sum_{j_1<\cdots<j_f} \sum_{l_1<\cdots<l_f} B^*_{j_1\cdots j_f} Z^{l_1\cdots l_f}_{j_1\cdots j_f} B_{l_1\cdots l_f}, \tag{4.54}$$

where for observables of the form (4.52) the matrix elements $Z^{l_1\cdots l_f}_{j_1\cdots j_f}$ can be evaluated as

$$Z^{l_1\cdots l_f}_{j_1\cdots j_f} = \sum_{R,S} \sigma(S)\sigma(R) \det(O^S_R) \det(P^{C(S)}_{C(R)}), \tag{4.55}$$

and the sum extends over all ordered m-element subsets $R = (r_1, \ldots, r_m)$ and $S = (s_1, \ldots, s_m)$ of $\{j_1, \ldots, j_f\}$ and $\{l_1, \ldots, l_f\}$, respectively. $C(R)$ denotes the complement of R, i.e. those indices of $(j_1, \ldots, j_f)$ that do not occur in R and analogous for $C(S)$. The single-particle submatrices O^S_R and $P^{C(S)}_{C(R)}$ of the matrices $O_{jl} = \langle \phi_j \mid O_B \mid \phi_l \rangle$ and $P_{jl} = \langle \phi_j \mid P_B \mid \phi_l \rangle$ are defined as in (4.46). The sign $\sigma(X)$ is the sign of the permutation $(X, C(X))$ relative to the original ordering of the indices.

By replacing in (4.52) the product $\prod_{\lambda=m+1}^{f} P_A(q_\lambda)$ with a projector $P_i = |i\rangle\langle i|$ onto ground or excited states $|i\rangle$ of the m-fold ionized system, one obtains, without further changes, ionization into the ionic ground state and shake-up. In that case one must ensure (approximate) orthogonality of the projectors $O_A P_i \approx 0$, i.e. the binding area A must be chosen large enough to accommodate the state $|i\rangle$.

4.9 Time propagation

As the working equations (3.25a), (3.25b) form a *non-linear* system of differential equations, some of the most efficient numerical time-propagators (such as Lanczos-Arnoldi; for a brief explanation of this algorithm see e.g. [47]) cannot be used because in their usual implementation they are only applicable to linear equations.

For time propagation we have settled on an explicit Runge-Kutta-type scheme of high order (4 or 5). Accuracy at each time step is checked by comparing the results obtained by advancing one step of h and two successive steps of $h/2$. Based on the recorded error, the step size and the order of the propagator are automatically adjusted.

To calculate ground states, imaginary time propagation is used. Our initial guess state is constructed from single-particle eigenfunctions. Expanding this into eigenstates $|0\rangle, |1\rangle, \ldots$ of the full Hamiltonian, the wave function propagated in imaginary time τ and continually normalized is

$$\Psi(\tau) = \frac{\mathrm{e}^{-\tau\epsilon_0}\,|0\rangle + \mathrm{e}^{-\tau\epsilon_1}\,|1\rangle + \cdots}{\sqrt{\mathrm{e}^{-2\tau\epsilon_0} + \mathrm{e}^{-2\tau\epsilon_1} + \cdots}}, \tag{4.56}$$

which, since $\epsilon_0 < \epsilon_1 < \cdots$, for large τ converges to the ground state,

$$\frac{\mathrm{e}^{-\tau\epsilon_0}\,|0\rangle[1 + \mathrm{e}^{-\tau(\epsilon_1-\epsilon_0)}\,|1\rangle + \cdots]}{\mathrm{e}^{-\tau\epsilon_0}\,\sqrt{1 + \mathrm{e}^{-2\tau(\epsilon_1-\epsilon_0)} + \cdots}} \to |0\rangle \quad \text{for} \quad \tau \to \infty. \tag{4.57}$$

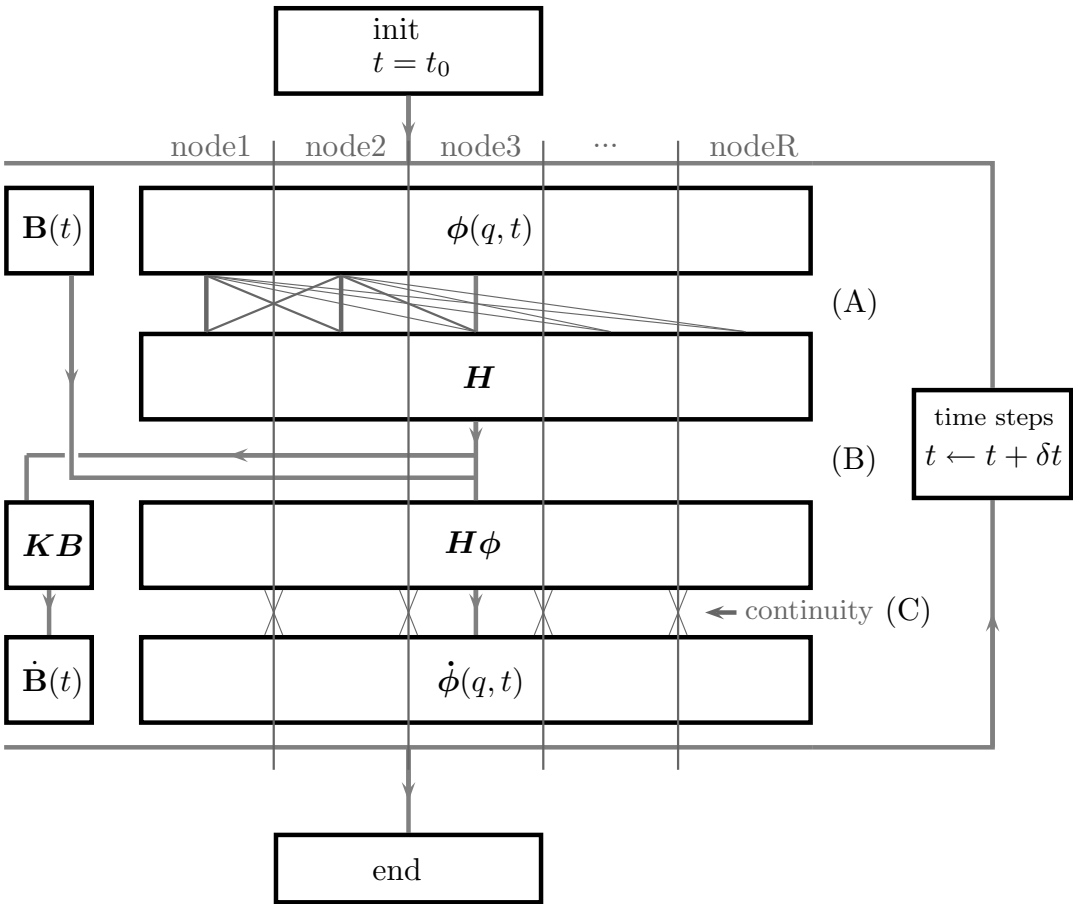

Figure 4.2: Parallelization of a MCTDHF calculation. Node boundaries are indicated by vertical lines. (A) the calculation of the mean field potentials involves all-to-all communication. (B) their application is strictly local, (C) continuity conditions require mostly nearest neighbor communication. Node boundaries are adjusted during computation.

Part II

Ionization of molecules

5 Strong-field ionization

5.1 Strong-field ionization for a single active electron

Strong laser fields give rise to *multi-photon* processes, which adds complexity as compared to single-photon interaction. From a theoretical point of view, the high field strength limits the use of perturbative techniques.

At the intensities considered here, the laser field can be treated purely classically. The two most popular ways to include it in the Hamiltonian are in length gauge $\vec{r}\cdot\vec{E}(t)$ or in velocity gauge $\vec{A}(t)\cdot\vec{p}+\vec{A}^2(t)$, where the dipole approximation is used, i.e. the spatial variation of the field is neglected. This approximation is admissible when the laser wavelength is much larger than the extent of the electronic wave function. It is easily fulfilled for the widely used Ti:Sapphire laser with a wavelength of 800 nm. Multipole terms can normally be neglected in infrared regime (see e.g. [59] for an experiment where quadrupole interaction was observed).

Usually, the vector potential is of the form $\vec{A}(t) = A_0(t)\vec{e}_z\cos(\omega t+\varphi_{CE})$, with a slowly varying envelope function $A_0(t)$, a constant polarization vector in z-direction, a monochromatic carrier wave, and a carrier-envelope phase (CEP) φ_{CE}. CEP becomes important at extremely short pulse lengths of a single or very few laser cycles. For usual pulse durations in the range of tens of femtoseconds, the two important characteristic properties of the laser are the carrier frequency ω and the intensity (or field strength). They can be combined into the ponderomotive potential $U_p = E^2/4\omega^2$, which is the mean kinetic energy of an electron in a harmonic electric field of field strength amplitude E. The important atomic property that largely determines the behavior of the atom in a strong field is its ionization potential I_p. Using U_p and I_p, Keldysh [39] defined a dimensionless quantity, the so-called Keldysh parameter γ,

$$\gamma = \sqrt{\frac{I_p}{2U_p}} = \frac{\omega\sqrt{2I_p}}{E}. \tag{5.1}$$

γ can be interpreted as the ratio $\omega_{\text{laser}}/\omega_{\text{tunnel}}$ of the laser frequency and the "tunneling frequency" of the electron. To define the latter, take as the velocity of the tunneling electron the average velocity in the ground state derived from the virial theorem, $v = \sqrt{2I_p}$. The tunneling distance is the width of the potential barrier for electrons of energy $-I_p$, $l = I_p/E$. This gives a tunneling period of $T_{\text{tunnel}} = v/l = \sqrt{2}\,E/\sqrt{I_p}$. By putting $\omega_{\text{tunnel}} = 2\pi/T$, we get

$$\frac{\omega_{\text{laser}}}{\omega_{\text{tunnel}}} = \frac{1}{4\pi}\frac{\omega\sqrt{2I_p}}{E} = \frac{1}{4\pi}\gamma, \tag{5.2}$$

which is proportional to the Keldysh parameter.

γ can be considered as a measure of adiabaticity, which determines the physical character of the ionization process. When the electron tunnels under the barrier much faster than the electric field changes, i.e. $\omega_{\text{tunnel}} \ll \omega_{\text{laser}}$, the static tunneling picture is applicable. Otherwise, the electron is promoted up to the continuum by multi-photon absorption. Thus, we have the limiting cases

$$\gamma \ll 1 \qquad \text{tunneling regime (high field, low frequency),} \tag{5.3a}$$

$$\gamma \gg 1 \qquad \text{multiphoton regime (low field, high frequency).} \tag{5.3b}$$

In many experiments, however, $\gamma \approx 1$ so that neither picture is alone applicable.

In [39], Keldysh developed the so-called strong-field approximation (SFA) to describe ionization in strong fields. The difficulty of strong-field problems arises from the fact that both the binding potential and the external field are of comparable strength and neither can be treated on a perturbative basis. The central, novel idea of Keldysh's method is to neglect the influence of the laser while the electron is bound, and neglect the binding potential when the electron is in the continuum. SFA is described in more detail in sec. 7.1.

Keldysh's theory in principle covers all values of γ. However, it takes into account only one bound state, while in the multiphoton regime resonances and near-resonances to excited states are important. Further, Keldysh did not treat the effects of the Coulomb potential on the continuum states.

At moderate intensities, multiphoton ionization is still amenable to low-order perturbation theory. Processes involving a different number of photons can then usually be distinguished by the scaling of their respective ionization rate with intensity:

$$\Gamma_n \sim I^n \quad \text{for } n\text{-photon process.} \tag{5.4}$$

Multiphoton ionization usually means that the electron absorbs just enough photons to reach the continuum,

$$\epsilon' = \epsilon + N\omega, \tag{5.5}$$

with N being the smallest integer such that $N\omega > I_p$, but at very high intensities, it can absorb a surplus S of photons,

$$\epsilon' = \epsilon + (N + S)\omega, \tag{5.6}$$

which is known as above-threshold ionization (ATI).

At the other extreme, we have tunnel ionization. In Landau-Lifshitz, the tunneling rate from the hydrogen ground state in a static electric field is derived as

$$\Gamma_H = \frac{4}{E} \exp\left(-\frac{2}{3E}\right), \tag{5.7}$$

using the semiclassical WKB-method to calculate the wave function under the barrier. Improving Keldysh's theory and including also Coulomb corrections lead to the tunneling formula of PPT (Perelomov-Popov-Terent'ev) [72], which became more widely

known as ADK (Ammosov-Delone-Krainov) theory [2]. The PPT/ADK tunneling formula is:

$$\Gamma_{\mathrm{ADK}} = (2I_p)\frac{2^{n^*}}{\Gamma(n^*+1)}\left(\frac{2(2I_p)^{3/2}}{E}\right)^{2n^*-1}\exp\left(-\frac{2(2I_p)^{3/2}}{3E}\right) \tag{5.8}$$

where $n^* := Z/\sqrt{2I_p}$ is the effective quantum number. Usually one assumes the quasistatic approximation, where for E one takes the instantaneous field strength $E(t)$ and then averages the rate over the laser cycle. The PPT/ADK formula performs well for tunneling. Even though strictly speaking it is not applicable for intermediate values of $\gamma \sim 1$, it often yields satisfactory results when using the cycle-averaged rates. Therefore it has been popular since most experiments are done in this γ-range. An improved tunneling theory which should be valid for all γ has been proposed in [107]. Going to very high intensities, we enter the region of *barrier suppression*, where the electron can leave without passing under a barrier. No adequate theory is known for this regime.

5.2 Strong-field ionization of molecules

Several experiments on the ionization of molecules by strong laser pulses show that these systems behave distinctly differently from atoms.

First, there are the effects of orientation of the molecule relative to the laser field. Both the ionization yield and the photoelectron angular distribution depend on the molecular symmetry with respect to the laser polarization direction ([57, 1, 74, 71]). To account for symmetry effects, both the SFA [66] and the PPT/ADK [97] theory for the ionization of atoms were generalized to molecules by replacing the atomic orbital of the single active electron (SAE) with a suitable approximation for a molecular system.

Other effects hinge on the additional degrees of freedom of the nuclei. The term enhanced ionization was introduced for the phenomenon that under certain circumstances ionization becomes more likely at particular internuclear distances. It can be understood intuitively by modelling the diatomic molecule by two potential wells, which are shifted upwards and downwards by the laser field. When the electron happens to be in the upper well, the tunneling barrier is lowered by the other nucleus [110, 86]. Bond softening [14] and bond hardening are other mechanisms that refer to the motion of the nuclear wave packet on the potential energy curves, which are deformed by the laser.

But there are also more subtle differences that are traced back to the in general more complex valence electronic structure, which gives rise to rich nonadiabatic dynamics.

Most strikingly, it is found that molecules resist ionization better than atoms with the same ionization potential [31, 56, 104], quite opposite to the naive expectation that the generally larger polarizability of molecules would enhance the effect of the laser on the molecule. Similar observations were made for metal clusters [91], transition metal

atoms [90], and and C_{60} [11]. In all cases the laser field strengths are assumed to be large enough for dominant ionization by tunneling or barrier suppression.

The enhanced resistance to ionization is generally attributed to multi-electron effects. The simplest multi-electron effect is screening, which reduces the effective field acting on a single electron and thus reduces tunneling. Screening can be included into the SAE picture by the addition of suitable polarization terms to the potential that the electron sees during tunneling [12]. The derivation of these corrections is exceedingly difficult and involves serious approximations. While the basic picture may well be correct, it is difficult to verify the approaches by comparison with experimental data only.

Meanwhile, the reverse trend has also been reported, i.e. that ionization and fragmentation occur at lower threshold intensities for larger molecules [60]. Inconclusive experimental evidence makes it doubtful that one may describe all situations in one simple picture.

Numerical calculations provide invaluable data on ionization that are of utmost importance, both as input to experiments and to verify more intuitive physical pictures of the ionization mechanisms. As discussed in the introduction, so far, this was possible only for a single or at most two active electrons in the field. Methods suitable for a higher number of electrons, such as TDHF and TD-DFT, have failed due to fundamental restrictions. This problem is overcome by the MCTDHF method.

6 Ionization yields as a function of molecule size with MCTDHF

6.1 System parameters

We investigate the ionization of 3D linear model molecules with two to six nuclei at a constant internuclear separation. It is assumed that there is one active electron per nucleus, while the remaining electrons only contribute through a screening of the nuclear potentials in the form

$$V_{\text{nucl}} = \sum_{k=1}^{K} \frac{1}{\sqrt{x^2 + y^2 + (z + kR)^2 + a^2}} \tag{6.1}$$

The screening parameter a was adjusted to obtain a constant ionization potential of 0.3 a.u. ($\approx$ 10 eV), independent of the number of nuclei K. Two different internuclear separations $R = 1.4$ and $R = 3.0$ were used in the calculations. As initial states we used the singlet neutral ground states of the molecules, obtained by imaginary time propagation. Note that in the 3D case, screening is only needed to adjust ionization potentials, whereas in 1D it is physically required to hide the singularity. The specific form of the screening in equation 6.1 was chosen in order to have the closest possible analogy with the commonly used 1D screened Coulomb potentials. We show below that our general conclusions are independent of that particular nuclear potential.

The model molecules are exposed to a laser pulse with linear polarization along the molecular axis (z-direction)

$$\vec{A}(t) = \vec{e}_z A_0(t) \sin(\omega t), \tag{6.2}$$

where we assumed Gaussian and $\sin^2$ envelope functions $A_0(t)$ with a width of 1 optical cycle. We use a laser frequency $\omega = 0.057$ ($\lambda = 800$ nm) and intensity $I = 2.5 \times 10^{13}$ W cm^{-2} (7.1×10^{-4} a.u.), which leads to nearly 90% depletion for the largest molecule at $R = 3$. For $R = 1.4$ a slightly higher intensity of $I = 3.0 \times 10^{13}$ W cm^{-2} (10^{-3} a.u.) was used. With the Keldysh parameter γ ranging from 1.4 to 1.65, we are in an intermediate regime.

6.2 Results and interpretation

Fig. 6.1 shows the depletion of the ground state after passage of the laser pulse for molecules with an increasing number of nuclei. The results are also listed in table 6.1.

	R	I	no. of nuclei	residual ground state population	
				MC	HF
3d	1.4	3.0×10^{13}	2	0.87	–
	1.4	3.0×10^{13}	4	0.82	–
	1.4	3.0×10^{13}	6	0.74	–
	3.0	2.5×10^{13}	2	0.88	0.96
	3.0	2.5×10^{13}	4	0.71	0.77
	3.0	2.5×10^{13}	6	0.14	0.11
1d	1.4	3.0×10^{13}	2	0.42	0.44
	1.4	3.0×10^{13}	4	0.49	0.57
	1.4	3.0×10^{13}	6	0.55	0.65
	3.0	2.5×10^{13}	2	0.54	0.65
	3.0	2.5×10^{13}	4	0.59	0.79
	3.0	2.5×10^{13}	6	0.66	0.85

Table 6.1: Residual ground-state population for 3D and 1D model molecules in the correlated (MC) and Hartree-Fock (HF) calculation.

For both internuclear separations, $R = 1.4$ and $R = 3$, depletion increases with the number of nuclei.

For fig. 6.1 we used a $\sin^2$ pulse shape and pulse duration of 1 optical cycle. At the very short pulse duration used here, the pulse shape becomes important, but it does not affect our results qualitatively. When a Gaussian pulse is used, the maximal change from 13% to 23% residual population occurs for the largest 3D molecule with internuclear separation $R = 3$.

The increase of depletion for long molecules is in accordance with naive expectations that larger molecules should respond more strongly to an external field because of their generally larger polarizability. It is, however, in striking disagreement with our findings for 1D model molecules with the same internuclear separations of $R = 1.4$ and $R = 3.0$, respectively, and at similar total depletion, where the opposite trend is observed: larger 1D molecules are harder to ionize. Another less pronounced difference between the 1D and 3D calculations is found in the single-configuration time-dependent Hartree-Fock (TDHF) approximation: in 1D, ionization yields calculated in TDHF are typically markedly below the correct yields, while in 3D, TDHF qualitatively agrees with MCTDHF with TDHF yields typically only by about 10% below MCTDHF.

At present, we cannot offer a conclusive explanation for these observations. Screening was suggested as the cause for the experimentally observed stability of multi-electron systems against ionization [56] and was identified qualitatively in 1D calculations [40]. In that picture, the electron density is enhanced near the tunneling barrier, which raises the potential barrier seen by a single electron, or, from an alternative point of view, reduces the local field strength. That mechanism exists in 3 dimensions,

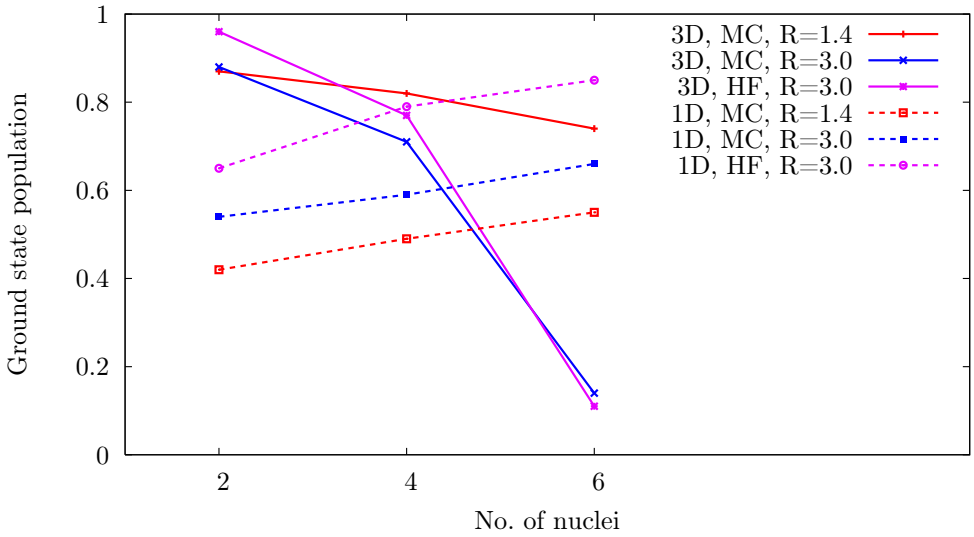

Figure 6.1: Residual ground-state population for 3D and 1D model molecules as a function of molecule size. In 3D, population decreases with molecule size for internuclear separations $R = 1.4$ and $R = 3$, and the Hartree-Fock result is similar to the correlated (MC) result. In contrast, 1D models show an increase of residual population with size.

as well. However, a closer inspection of the idea shows that

(i) it is applicable only to static electric fields or at Keldysh parameters $\gamma \ll 1$, and

(ii) the Stark shift of the tunneling electron energy relative to the top of the tunneling barrier must be properly included. The constraint on the Keldysh parameter in molecules may be more stringent, as electron mobility is not so much characterized by the ionization potential I_p, but by the spacing between ground and excited electronic levels, which decreases with size and with it mobility. Hence the electrons will spend more time under the barrier than suggested by the Keldysh parameter. Even when the quasi-static tunneling picture is applicable, the interplay of screening on the one hand and adiabatic dc Stark shift on the other hand is complicated by the fact that both quantities enter exponentially into the tunneling rate.

The 3D potentials 6.1 were used because of their similarity to the 1D model potentials, which allowed us to more clearly expose effects due to dimensionality. We repeated the calculations with modified Coulomb potentials of the form

$$V_{\text{nucl}} = \sum_k V(\sqrt{x^2 + y^2 + (z + kR)^2}), \qquad V(r) = -\frac{1}{r} + \mathrm{e}^{-ar}\,\frac{b}{r}, \tag{6.3}$$

observing the same trend.

6.3 Conclusions

We have performed to our knowledge the first calculations of molecular strong-field ionization in 3D and with several correlated electrons. Indeed, the use of simplified 1D models for the study of strong field ionization is put into serious doubt by our findings. Such models may only be used for quick studies, but always require independent confirmation by a more refined calculation. Also, we must re-raise the question about the unexpected stability of larger molecules when compared to atoms with the same ionization potential. At least for our 3D linear model molecules, we cannot confirm such a tendency. Influence of core electrons cannot be excluded, but seems unlikely as ionization depends only weakly on the precise form of core screening. Laser pulse parameters used here were not fully realistic: although pulse shape has no influence on our conclusions, pulse duration is much shorter than in experiments, and hence the spectrum contains a wider range of frequencies. For a systematic comparison with experiments, longer pulses and a more realistic modelling of the valence electrons will be required.

Part III

Correlation effects in high harmonic generation of molecules

7 Review of high harmonic generation

7.1 HHG in atoms

A gas of atoms or molecules exposed to a strong laser pulse emits radiation that contains odd multiples of the laser fundamental frequency up to very high order. This so-called *high harmonic generation* (HHG) was first observed in 1987 [61], where the 17th harmonic was detected, as of today harmonic orders up to 700 have been achieved [87].

At lower field strengths, the macroscopic response of a medium to an external electric field is usually described in terms of the polarizabilities $\chi^{(n)}$, such that

$$P_i = \chi^{(1)}_{ij} E_j + \chi^{(2)}_{ij_1 j_2} E_{j_1} E_{j_2} + \cdots \tag{7.1}$$

where P_i is the dipole moment and $\chi^{(n)}$ is a tensor of rank $n+1$. For a monochromatic field, $\chi^{(n)}$ gives rise to harmonic order n. In general, the polarizibilities are frequency-dependent, $\chi^{(n)}(\omega; \omega_1, \ldots, \omega_{n-1})$, which has the physical meaning of temporal non-locality, i.e. the polarization at time t is the cumulative outcome of the field at prior times. Theoretically, the perturbation series makes sense if convergence is assured, and practically, if a reasonably small number of terms are sufficient for accurate results. At high field strengths, the expansion converges at least very slowly (if at all), and thus is not very useful.

That HHG contains only odd multiples of the laser frequency is strictly speaking only true for infinitely long, monochromatic laser pulses, and inversion-symmetric targets (which comprises all atoms). The Hamiltonian of such a system,

$$H = \frac{p^2}{2} + V(\vec{r}) + \vec{r} \cdot \vec{E}_0 \cos \omega t, \tag{7.2}$$

is invariant under the combined spatial inversion and temporal translation by half a laser period, $(\vec{r}, t) \to (-\vec{r}, t + T/2)$. The harmonic spectrum $S(\omega)$ is derived from the Fourier transform of $\ddot{\vec{P}}$,

$$S(\omega) \propto |\mathcal{F}[\ddot{\vec{P}}](\omega)|^2. \tag{7.3}$$

Demanding from $\vec{P}$ the same symmetry as the Hamiltonian,

$$\vec{P}(t) = -\vec{P}\left(t + \frac{T}{2}\right), \tag{7.4}$$

and expanding it in a Fourier series,

$$\vec{P}(t) = \sum_n \vec{P}_n \mathrm{e}^{\mathrm{i}\, n\omega t}\,, \tag{7.5}$$

leads to the requirement $\vec{P}_n = (-1)^{n+1}\vec{P}_n$, which is only fulfilled by odd harmonics.

For a realistic, finite-length pulse, the discrete spectral lines will be broadened. Molecules without inversion center or setups with more than one laser frequency involved will not follow these rules.

7.1.1 Semiclassical 3-step model

The origin of the non-linearity responsible for the high-energy part of the harmonic spectrum is the electron ionization-recollision process described by the semi-classical 3-step model (also called the simple man's model) proposed by Ken Schafer [46] and Paul Corkum [19]. The three steps are:

1. (tunnel) ionization,
2. acceleration in the laser field,
3. recollision, recombination and emission of photon.

The ionization occurs near the peak of the electric field due to the exponential dependence of the tunneling rate on the field strength. After its release, the electron is first driven away from the atom by the laser and then back again, which is described by the classical equations of motion:

$$\text{initial conditions: } \vec{r}(t_0) = \vec{r}_0, \dot{\vec{r}}(t_0) = \vec{k}_0 \tag{7.6a}$$

$$\ddot{\vec{r}}(t) = -\vec{E}(t) = \dot{\vec{A}}(t) \tag{7.6b}$$

$$\dot{\vec{r}}(t) = \vec{k}_0 + [\vec{A}(t) - \vec{A}(t_0)] \tag{7.6c}$$

$$\vec{r}(t) = \vec{r}_0 + \int_{t_0}^{t} \mathrm{d}t' \vec{A}(t') + [\vec{k}_0 - \vec{A}(t_0)](t - t_0) \tag{7.6d}$$

The recollision condition $\vec{r}(t_1) = \vec{r}(t_0)$ leads to

$$\int_{t_0}^{t_1} \mathrm{d}t' \vec{A}(t') = -[\vec{k}_0 - \vec{A}(t_0)](t_0)(t_1 - t_0), \tag{7.7}$$

which for each time of birth t_0 determines the time of recollision $t_1[t_0]$. For tunnel ionization, the initial position $\vec{r}_0$ is the classical turning point at the outer side of the potential barrier, but in first approximation one can set $\vec{r}_0 \approx 0$. The initial velocity $\vec{k}_0 \approx 0$ also, as the electron emerges with zero kinetic energy from the tunnel. [1] The

[1] For an electron of energy ϵ, the classically forbidden region is defined by $V(\vec{r}) > \epsilon$. Thus at the end of the tunnel $V(\vec{r}_0) = \epsilon$, which means that the emerging electron has only potential and no kinetic energy.

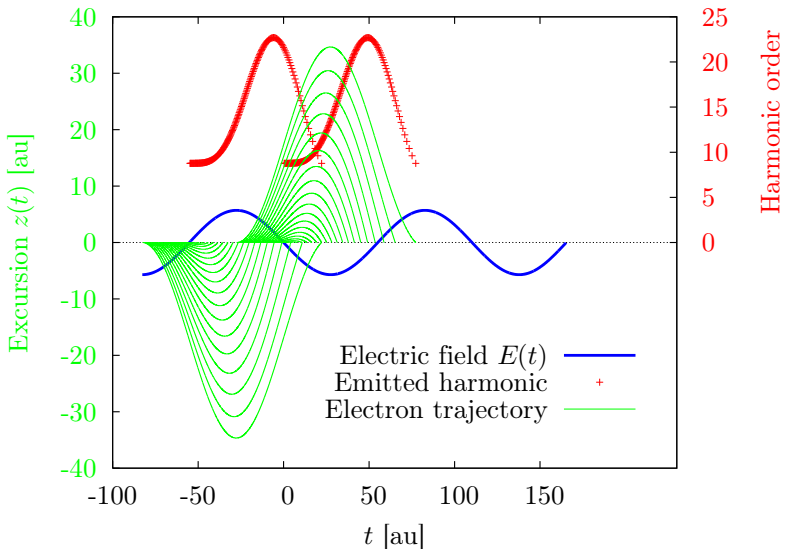

Figure 7.1: Electron trajectories $z(t)$ (green, left y-scale) in a linearly polarized, sinusoidal electric field $E(t)$ (blue). Trajectories are shown for birth times approximately every 1.38 au. Red crosses denote the harmonic order (right y-scale) emitted at recollision. The harmonic order $N = \omega/\omega_{\text{laser}}$ is given by the emitted photon energy $\omega = k_1^2/2 + I_p$ divided by the laser photon energy $\omega_{\text{laser}} = 0.057$. The offset of the harmonic order from zero is due to I_p. ($I_p = 0.5, I = 1.1 \times 10^{14}$ W cm^{-2}, $\lambda = 800$ nm)

kinetic energy at recombination is $\epsilon_{\text{kin}} = [\vec{A}(t_1) - \vec{A}(t_0)]^2/2 = k_1^2/2$. Upon recombination, the kinetic energy plus the binding energy (ionization potential) I_p is emitted in a photon of frequency $\omega = k_1^2/2 + I_p$. Fig. 7.1 shows the trajectories $z(t)$ of electrons ionized at different birth times, their recollision times and the corresponding harmonic order produced. For each photon energy (except the maximum), there are two types of trajectories, a short and a long one, which occur once per half-cycle. The mapping from harmonic frequencies to recollision times can be used to obtain timing information from a harmonic spectrum [3]. The highest classically possible electron energy determines the cutoff of the harmonic spectrum

$$\omega_{\text{cut}} = 3.17U_p + I_p, \tag{7.8}$$

where $U_p = A_0^2/4$ is the ponderomotive potential, the average kinetic energy of an electron in a sinusoidal electric field $A_0 \cos \omega t$.

7.1.2 Quantum mechanical approximations: SFA/Lewenstein model

A quantum-mechanical description of HHG, which recovers the essential features of the 3-step model, was given within the framework of the strong-field approximation by Lewenstein et al. [55].

As mentioned in sec. 5.1, the problem with the analytical solution for a bound electron in a strong field is that one has to deal with two potentials, the binding potential and the time-dependent electric field, at the same time and neither of them is small enough for a perturbative ansatz. For each of them separately, exact solutions are available, but not for both. Keldysh [39] circumvented this obstacle by the following idea, which is at the core of the strong-field approximation (SFA). The time evolution of the electron is divided into two phases: before the ionization, and after the ionization. In phase one, the laser field can be neglected, in phase two, the binding potential. (Perturbative corrections can then be applied afterwards.)

S-matrix formalism of SFA

Historically, the first setting which naturally lended itself to this concept was calculation of strong-field ionization via S-matrix theory. The S-matrix is

$$S_{fi} = \langle f \mid U(+\infty, -\infty) \mid i \rangle, \tag{7.9}$$

where U is the time evolution operator or propagator, $|i\rangle$ the initial state, and $|f\rangle$ the final state. U obeys the same Schrödinger equation as $\Psi(t)$,

$$\begin{aligned} &\mathrm{i}\,\partial_t U(t,t_0)|\Psi(t_0)\rangle = H(t)U(t,t_0)|\Psi(t_0)\rangle \Rightarrow \\ &\mathrm{i}\,\partial_t U(t,t_0) = H(t)U(t,t_0) \end{aligned} \tag{7.10}$$

with the initial condition $U(t_0,t_0) = \mathbb{1}$. We now consider two splittings of the Hamiltonian

$$H = H_0 + F = H_F + V \tag{7.11}$$

and assume that the evolution operators U_0 for H_0 and U_F for H_F are known. We can rewrite (7.10) for the full evolution operator U as

$$(\mathrm{i}\,\partial_t - H_0)U = FU. \tag{7.12}$$

Using the Green's function of $(\mathrm{i}\,\partial_t - H_0)$, which is $-\mathrm{i}\,U_0(t,t')\Theta(t-t')$, the solution is

$$U(t,t_0) = U_0(t,t_0) - \mathrm{i}\int_{t_0}^{t} \mathrm{d}t'\, U_0(t,t')F(t')U(t',t_0). \tag{7.13}$$

Alternatively, we can also reformulate the equation for U_0 as

$$(\mathrm{i}\,\partial_t - H)U_0 = -FU_0, \tag{7.14}$$

and use the full Green's function $-\mathrm{i}\,U(t,t')\Theta(t-t')$ to find the solution

$$U_0(t,t_0) = U(t,t_0) + \mathrm{i}\int_{t_0}^{t} \mathrm{d}t'\, U(t,t')F(t')U_0(t',t_0). \tag{7.15}$$

The latter expression proves to be particularly suitable for performing a strong-field approximation. The S-matrix can now be written

$$\begin{aligned} S_{fi} &= \langle f \mid U(+\infty,-\infty) \mid i\rangle \\ &= \langle f \mid U_0(+\infty,-\infty) \mid i\rangle + \left\langle f \,\middle|\, \mathrm{i}\int_{-\infty}^{+\infty} \mathrm{d}t\, U(+\infty,t)F(t)U_0(t,-\infty) \,\middle|\, i\right\rangle \end{aligned} \tag{7.16}$$

The final and initial states are eigenstates of H_0 since the perturbation F is assumed to vanish asymptotically for infinite future and past. Consequently, the first term $\langle f|U_0|i\rangle = \delta_{fi}$ just describes free propagation with no interaction taking place and it is therefore subtracted. The quantity of interest is

$$(S-\mathbb{1})_{fi} = \mathrm{i}\int_{-\infty}^{+\infty} \mathrm{d}t\, \langle f \mid U(+\infty,t)F(t)U_0(t,-\infty) \mid i\rangle. \tag{7.17}$$

For the interaction of an atom with a laser, $H_0 = p^2/2 + V$ is the usual atomic Hamiltonian, and F is the interaction with the laser field, which can be given in length or velocity gauge

$$F^{(len)} = \vec{r}\cdot\vec{E}(t), \tag{7.18a}$$

$$F^{(vel)} = \vec{A}\cdot\vec{p} + \frac{\vec{A}^2}{2}. \tag{7.18b}$$

In (7.17) $U(-\infty,t)$ describes the motion of the electron after ionization mediated by F has taken place. SFA consists in replacing the unknown full propagator $U(+\infty,t)$ by the propagator in the laser field alone $U_F(+\infty,t)$ and using for $\langle f|$ a Volkov state ${}_V\langle k,t|$, which is the exact solution for a free electron in the laser field with Hamiltonian H_F. Volkov states can be labelled by the canonical momentum $\vec{k} = \vec{k}_{\mathrm{phys}} - \vec{A}$, which is conserved by H_F:

$$\psi^{(len)}_{V,\vec{k}} = \frac{1}{(2\pi)^{3/2}} \mathrm{e}^{\mathrm{i}[\vec{k}+\vec{A}(t)]\cdot\vec{r}}\, \mathrm{e}^{-\mathrm{i}\,\Phi(\vec{k},t)}\,, \tag{7.19a}$$

$$\psi^{(vel)}_{V,\vec{k}} = \mathrm{e}^{-\mathrm{i}\,\vec{A}(t)\cdot\vec{r}}\, \psi^{(len)}_{V,\vec{k}}, \tag{7.19b}$$

where

$$\Phi(\vec{k},t) = \int^t \mathrm{d}\tau\, \frac{1}{2}\,[\vec{k}+\vec{A}(\tau)]^2. \tag{7.20}$$

is the Volkov phase. Hence, the S-matrix element for ionization in strong-field approximation reads

$$(S-\mathbb{1})_{fi} = \mathrm{i}\int_{-\infty}^{+\infty} \mathrm{d}t\, \langle k,t|F(t)|i,t\rangle. \tag{7.21}$$

A similar procedure can be applied to derive an SFA expression for the dipole

moment

$$P_z(t) = \langle \Psi(t) \mid z \mid \Psi(t) \rangle, \tag{7.22}$$

from which high harmonic spectra are calculated. Writing $|\Psi(t)\rangle = U(t, -\infty)|i, -\infty\rangle$, inserting (7.15) and again replacing U by U_F leads to [10]

$$P_z(t) = \int_{-\infty}^{t} \mathrm{d}t' \, \mathrm{d}t'' \, \langle i, t'|V U_F(t', t) z U_F(t, t'') V|i, t''\rangle. \tag{7.23}$$

Lewenstein model

An alternative approach to the SFA is by modifying the Schrödinger equation directly, rather than the S-matrix. Lewenstein [55] adopted this approach to obtain a formula for HHG within SFA. We will derive it in a different, more transparent way [85], but the result is the same.

The electronic wave function is written as the sum of the atomic ground state plus a linear combination of Volkov states,

$$|\Psi(t)\rangle = c(t)|0, t\rangle + \int_k b_k(t)|k, t\rangle_V, \tag{7.24}$$

with

$$\mathrm{i}\,\partial_t|0, t\rangle = H_0|0, t\rangle, \tag{7.25a}$$

$$\mathrm{i}\,\partial_t|k, t\rangle_V = H_F|k, t\rangle_V. \tag{7.25b}$$

The coefficients c, b_k in this ansatz are not yet unique, since our basis set is overcomplete (the Volkov states are already complete on their own). To fix this, one imposes a further orthogonality condition

$$\int_k b_k(t)\langle 0, t \mid k, t\rangle_V = 0. \tag{7.26}$$

Equations for c, b_k can be derived by using the Dirac-Frenkel variational principle with constraint (7.26),

$$\langle \delta\Psi \mid i\partial_t - H(t) \mid \Psi\rangle + \lambda\left[\int_k b_k^*(t)_V\langle k, t|0, t\rangle\right] + \mu\left[\int_k \langle 0, t|k, t\rangle_V b_k(t)\right], \tag{7.27}$$

where λ, μ are Lagrange multipliers. To simplify notation we will temporarily drop the label V for Volkov states and suppress the explicit t-dependence for all quantities. Variation w.r.t. c^*, b_k^* and λ, μ yields

$$\mathrm{i}\,\dot{c} = \langle 0|V|l\rangle b_l - \langle 0|l\rangle \mathrm{i}\,\dot{b}_l \tag{7.28a}$$

$$\mathrm{i}\,\dot{b}_k = -\mathrm{i}\,\dot{c}\langle k|0\rangle + \langle k|F|0\rangle c + \langle k|V|l\rangle b_l - \lambda\langle k|0\rangle \tag{7.28b}$$

$$b_l^*\langle l|0\rangle = 0 = \langle 0|l\rangle b_l. \tag{7.28c}$$

By differentiation of the last equation, we get

$$\mathrm{i}\,\dot{b}_l\langle 0|l\rangle = -\langle 0|H_F|l\rangle b_l. \tag{7.29}$$

Inserting this into (7.28a) gives

$$\mathrm{i}\,\dot{c} = \langle 0|F|l\rangle b_l. \tag{7.30}$$

Eliminating $\dot{b}_k$ in (7.28b) and (7.29) leads to

$$\lambda = \langle 0|V|l\rangle b_l - \langle 0|F|l\rangle b_l - \langle 0|H_F|l\rangle b_l = 0. \tag{7.31}$$

Thus, (7.28b) becomes

$$\mathrm{i}\,\dot{b}_k = \langle k|F|0\rangle c - \langle k|0\rangle\langle 0|F|l\rangle b_l + \langle k|V|l\rangle b_l. \tag{7.32}$$

With $F = V - H_0 + H_F$ we arrive at

$$\mathrm{i}\,\dot{b}_k = \langle k|F|0\rangle c - \langle k|0\rangle\langle 0|H_F|l\rangle b_l + \langle k|(1-P_0)V|l\rangle b_l. \tag{7.33}$$

where $P_0 = |0\rangle\langle 0|$. Because of (7.26), $\langle k|(1-P_0)V|l\rangle b_l = \langle k|(1-P_0)V(1-P_0)|l\rangle b_l =: \langle k|V_\perp|l\rangle b_l$. Our final form of the equations of motion is hence

$$\mathrm{i}\,\dot{c} = \langle 0|F|l\rangle b_l \tag{7.34a}$$

$$\mathrm{i}\,\dot{b}_k = \langle k|F|0\rangle c - \langle k|0\rangle\langle 0|H_F|l\rangle b_l + \langle k|V_\perp|l\rangle b_l. \tag{7.34b}$$

The terms $\langle 0|F|l\rangle b_l$ and $\langle k|F|0\rangle c$ describe transitions from the Volkov states to the ground state and vice versa, respectively, induced by the field. $\langle k|V_\perp|l\rangle b_l$ accounts for scattering within the space orthogonal to $|0\rangle$ due to the binding potential. The term $\langle k|0\rangle\langle 0|H_F|l\rangle b_l$ arises from the non-orthogonality of the Volkov states to the ground state (otherwise $\langle k|0\rangle = 0$): even when $\langle 0|k\rangle b_k = 0$ initially, the free evolution of the Volkov states would create ground state contamination, which must be subtracted to maintain the orthogonality condition.

SFA consists in making the following approximations to these equations:

- Neglect the depletion of the ground state: $\dot{c} = 0$.
- Neglect the influence of the binding potential on everything but the ground state: $\langle l|V_\perp|k\rangle = 0$.
- Neglect the non-orthogonality of ground and Volkov states: $\langle k|0\rangle = 0$, whence $\langle k|0\rangle\langle 0|H_F|l\rangle b_l = 0$.

This simplifies things considerably: the SFA version of the TDSE is (returning to previous explicit notation):

$$c = 1 \tag{7.35a}$$

$$\mathrm{i}\,\dot{b}_k(t) = {}_V\langle k,t|F(t)|0,t\rangle. \tag{7.35b}$$

SFA is not gauge-invariant, therefore different gauges lead to different results. In the following, we use length gauge for the Volkov states (7.19a) and the interaction operator (7.18a), and assume a linearly polarized electric field, i.e. $F = zE_z(t)$. (7.35b) can be integrated to

$$b_k(t) = -\mathrm{i}\int_{t_0}^{t} \mathrm{d}t'\, \mathrm{e}^{\mathrm{i}\int^{t'} \mathrm{d}\tau([\vec{k}+\vec{A}(\tau)]^2/2+I_p)}\, \langle \vec{k}+\vec{A}(t') \mid E_z(t')z \mid 0\rangle, \tag{7.36}$$

where $|k\rangle$ is used for the plane wave $\mathrm{e}^{\mathrm{i}\,\vec{k}\cdot\vec{r}}$ (in contrast to Volkov states).

Given the wave function (7.24), the time-dependent dipole moment $P_z(t)$ is

$$\begin{aligned} P_z(t) = \langle\Psi(t)|z|\Psi(t)\rangle = \langle 0,t|z|0,t\rangle + 2\,\mathrm{Re}\left[\int_k \langle 0,t|z|k,t\rangle_V b_k(t)\right] \\ + \int_k\int_l {}_V\langle l,t|z|k,t\rangle_V b_l^*(t)b_k(t). \end{aligned} \tag{7.37}$$

The first term is zero due to inversion symmetry of the ground state. The last term can be neglected since continuum-continuum transitions contribute only little to harmonic emission (which can be verified numerically). Inserting b_k gives

$$\begin{aligned} P_z(t) &= -\mathrm{i}\int \mathrm{d}^3k \int_{t_0}^{t} \mathrm{d}t' \langle 0,t|z|\vec{k}+\vec{A}(t)\rangle \mathrm{e}^{-\mathrm{i}\int^t \mathrm{d}\tau([\vec{k}+\vec{A}(\tau)]^2/2)} \\ &\quad \times \mathrm{e}^{\mathrm{i}\int^{t'} \mathrm{d}\tau'([\vec{k}+\vec{A}(\tau')]^2/2)}\, E_z(t')\langle \vec{k}+\vec{A}(t')|z|0,t'\rangle + \mathrm{c.c.} \\ &= -\mathrm{i}\int \mathrm{d}^3k \int_{t_0}^{t} \mathrm{d}t'\, \langle 0|z|\vec{k}+\vec{A}(t)\rangle \mathrm{e}^{-\mathrm{i}\int_{t'}^{t} \mathrm{d}\tau([\vec{k}+\vec{A}(\tau)]^2/2)+I_p}\, E_z(t')\langle \vec{k}+\vec{A}(t')|z|0\rangle + \mathrm{c.c.} \\ &= -\mathrm{i}\int \mathrm{d}^3k \int_{t_0}^{t} \mathrm{d}t'\, d_z^*[\vec{k}+\vec{A}(t)]\mathrm{e}^{-\mathrm{i}\,S(\vec{k},t,t')}\, E_z(t')d_z[\vec{k}+\vec{A}(t')] + \mathrm{c.c.}, \end{aligned} \tag{7.38}$$

where

$$S(\vec{k},t,t') = \int_{t'}^{t} \mathrm{d}\tau \left\{ \frac{[\vec{k}+\vec{A}(\tau)]^2}{2} + I_p \right\} \tag{7.39}$$

and $d_z[\vec{k}] = \langle \vec{k}|z|0\rangle$.

(7.38) can be nicely interpreted in terms of the 3-step model: $E_z(t')d_z[\vec{k}+\vec{A}(t')]$ describes ionization by the laser field at birth time t', creating an electron of canonical

momentum $\vec{k}$ and physical momentum $\vec{k}+\vec{A}(t')$. $\mathrm{e}^{-\mathrm{i}\,S(\vec{k},t,t')}$ is the phase factor accumulated by the electron as it propagates freely in the laser field until time t. $d_z^*[\vec{k}+\vec{A}(t)]$ is the amplitude for recombination at time t. The whole expression is integrated over all birth times t' and all momenta $\vec{k}$.

The integration over k is customarily performed in the saddle point approximation, which is usually justified since the dipole matrix elements $d_z[\vec{k}]$ are slowly varying functions of $\vec{k}$, while the phase $S(\vec{k},t,t')$ is changing much faster. In the saddle point approximation one expands the exponent around its stationary points $\vec{k}_{st}$, i.e. zeros of the first derivative,

$$\partial_{k_j} S(\vec{k},t,t')|_{k_{st}} = \int_{t'}^{t} \mathrm{d}\tau [k_j + A_j(\tau)]\Big|_{k_{st}} = 0 \tag{7.40}$$

$$k_{st}(t,t') \equiv k_{st,z}(t,t') = -\frac{1}{(t-t')}\int_{t'}^{t} \mathrm{d}\tau A_z(\tau) \tag{7.41}$$

$$k_{st,x} = k_{st,y} = 0, \tag{7.42}$$

assuming linear polarization $\vec{A} = A(t)\vec{e}_z$. In (7.41) we recognize the recollision condition (7.7) with $k_{st} = k_0 - A(t')$. $k_{st}(t,t')$ is the canonical momentum that allows the electron starting at t' to return to the origin at time t. Using

$$\partial_{k_l}\partial_{k_j} S(\vec{k},t,t') = (t-t')\delta_{jl}, \tag{7.43}$$

S is expanded to second order in k,

$$S(\vec{k},t,t') = S(k_{st}(t,t'),t,t') + \tfrac{1}{2}\,(\vec{k}-\vec{k}_{st}(t,t'))^2 + O(k^3) \tag{7.44}$$

which leads to

$$\begin{aligned} P_z(t) = -\mathrm{i}\int_{t_0}^{t} \mathrm{d}t' \left(\frac{\pi}{\epsilon + \mathrm{i}\,t'}\right)^{3/2} d_z^*[k_{st}(t,t') + A_z(t)]\mathrm{e}^{-\mathrm{i}\,S(k_{st}(t,t'),t,t')} \\ \times E_z(t') d_z[k_{st}(t,t') + \vec{A}(t')] + \mathrm{c.c.}\,. \end{aligned} \tag{7.45}$$

Here, the first factor in the integral with infinitesimal ϵ comes from the regularized Gaussian integration over $\vec{k}$.

7.1.3 Limitations and extensions of SFA

SFA is the work horse for interpreting strong-field experiments, specifically the Lewenstein model for HHG (see e.g. [36], [34], [3]).

However, as outlined above, SFA makes rather far-reaching approximations, which imply:

- Single-electron approximation.
- Neglects influence of the laser on the bound system by ignoring excited states and depletion of the ground state.

- Uses plane waves as continuum states, neglecting the binding potential.
- Not gauge-invariant: the choice of the interaction operator (length or velocity or other gauge) matters.

Excellent agreement between SFA and exact TDSE calculations of hydrogen was shown for high-energetic electrons [6]. At low energies, the omission of the Coulomb effects on the continuum states results in substantial discrepancies.

SFA underestimates the total ionization yield by up to order-of-magnitude factors [7], mainly because the Coulomb potential actually lowers the tunneling barrier. Coulomb force also affects the sub-cycle dynamics of strong-field ionization [88], creates a pronounced "dip" at zero energy in the momentum distributions of photoelectrons [63], and modifies the left-right asymmetry in photoelectron spectra caused by carrier-envelope phase effects in very short laser pulses [17]. While total ionization rates can be successfully repaired by introducing an additional prefactor that accounts for the action of the Coulomb potential during tunneling [43, 9], the electron distributions cannot be patched up in this way [77]. Many ways of taking into account Coulomb effects more comprehensively have been proposed (for a recent work see e.g. [89], where the Coulomb-eikonal Volkov states have been developed for this purpose).

The issue of gauge-noninvariance has induced a debate about which gauge is most suitable for SFA. What can be said, is that the answer depends on the concrete problem (see e.g. [18] vs. [5]). Related to it is the question of which *dipole operator* to choose for calculating the spectrum. (Note: In the SFA formula for the dipole moment (7.45), one matrix element contains the dipole operator, and the other the interaction operator, which we chose to be the same, but this need not necessarily be so.) See sec. 9.1.2 for further discussion on this topic.

Another severe restriction of conventional SFA is the single active electron approximation. Particularly as HHG experiments turn to molecules the role of multi-electron effects becomes increasingly relevant.

7.2 HHG in molecules

7.2.1 New features in molecular HHG

Like for the ionization rates discussed in sec. 5.2, the additional degrees of freedom present in molecules lead to a number of effects which are absent in HHG from atoms. Of the three steps of harmonic generation, the structure of the core plays an important role in the ionization and recombination steps. All factors which affect ionization thus potentially also show up in the harmonic spectrum. New aspects arise from recombination, which on the one hand represent additional complications, on the other hand open the possibility to gain further knowledge.

In particular, information about the ground state wave function $|0\rangle$ is encoded into the spectrum, which, apart from the laser pulse, is entirely determined by the dipole matrix element $\langle k|\vec{r}|0\rangle$.

In their simplest manifestation, the properties of the electronic initial state lead to so-called two-center interference in diatomic molecules [51]. While the ionization of the electron takes place predominantly at large distance from the nuclei through tunneling (multi-photon process), the recombination occurs mainly in the vicinity of the nuclei (single-photon process). Instead of a transition into a molecular orbital, we can visualize this step as a recombination into either of the two atomic orbitals localized at the nuclei. The two different contributions then add up coherently to deliver the total recombination amplitude. Interference occurs because the electron acquires a phase difference $\Delta\varphi = kR$ (where R is the distance between the nuclei) when going to one or the other nucleus. If $\Delta\varphi = \pi$, the interference is destructive and a minimum at the corresponding harmonic frequency $\omega(k)$ appears. By aligning the molecular axis at an angle θ to the laser polarization, the effective internuclear distance in direction of the electron momentum is $R\cos\theta$ and can be varied, which shifts the position of the minimum. The idea has been confirmed by experiments on CO_2 [36, 102]. By measuring the full harmonic spectrum as a function of the alignment angle over the whole range, it would in principle be possible to reconstruct the complete orbital wave function. This famous "orbital imaging" concept is explored further in the next section.

Not only the static structure of the molecule, but also its time evolution leaves its traces in the harmonic spectrum. A detailed analysis shows that the overlap of the nuclear wave function at ionization and recombination time enters the expression for the harmonic signal [53]. This was used to track the distance of the nuclei during dissociation of D_2^+ [3].

As of yet, HHG from molecules has been mainly investigated in the single-electron approximation, adapting the atomic Lewenstein model by simply replacing the atomic state by a molecular orbital. This orbital is often chosen as the HOMO, the highest occupied molecular orbital, as ionization from lower orbitals is expected to be exponentially suppressed. However, lower orbitals can become important when ionization from the HOMO is suppressed due to orientation, or when its harmonic emission is suppressed due to e.g. two-center interference. A first step towards a multi-electron description has been taken by extending the SFA to multi-electron ground states [70, 82]. These models include ionization from and recombination into lower orbitals. Still, they do not account for multi-electron *dynamics* as only the ground state enters.

Multi-electron effects have not yet been directly identified in experiment, which is not astonishing, as there are almost no calculations to compare with. It is the intent of the present work to point out that these effects cannot be neglected, in particular for the recombination step. Recently, the significance of multi-electron effects has been confirmed in [94] for a 2-electron model. The authors ascribe major contributions to polarizability of the neutral, electron exchange and collisional excitation of the ion. Different from our observations, but also for a different system, they find no sizable influence of the polarization of the ion.

7.2.2 Orbital imaging with HHG

One of the most intriguing, but also most controversial experiments in attosecond science is probably the imaging of molecular orbitals with high harmonics [34]. In contrast to other commonly used imaging methods (like X-ray or electron scattering), this technique would allow to recover the complete wave function, including not only the density but also the quantum phase. Another promise is that one can selectively image only the HOMO.

A molecule, in this particular experiment N_2, is first aligned by a weak prepulse, and then ionized by an intense femtosecond laser pulse, leading to harmonic emission. Ionization is assumed to happen only from the HOMO, ionization from lower orbitals being exponentially suppressed. The harmonic spectrum is recorded for a grid of values of the angle θ between molecular and polarization axis, which then allows to reconstruct the molecular orbital in a manner similar to X-ray tomography.

We write the total wave function as a sum of the ground state and a continuum wave packet

$$|\Psi(t)\rangle = a_0(t)|0,\theta\rangle + |\mathrm{cont},t\rangle. \tag{7.46}$$

$|0,\theta\rangle$ means that the molecule is aligned at an angle θ to the laser polarization. We assume that the recollision happens over a short time period so that the field strength can be considered fixed $E \approx \mathrm{const.}$, further, that on recollision the wave packet has spread to a considerable lateral width and that the binding potential can be neglected. In this case, the wave packet can be expanded in plane waves with momentum k along the laser polarization,

$$|\mathrm{cont},t\rangle = \int_k a(k)|k,t\rangle, \tag{7.47}$$

$$\langle x|k,t\rangle = \frac{1}{(2\pi)^{3/2}}\mathrm{e}^{i(kx-\nu(k)t)}\,, \quad \nu(k) = \frac{k^2}{2}. \tag{7.48}$$

The dipole moment of the wave function (7.46) is

$$P_z(t) = \langle\Psi(t)|z|\Psi(t)\rangle = 2\,\mathrm{Re}\left[\int \mathrm{d}k\, a(k)\langle 0,\theta|z|k\rangle \mathrm{e}^{-i\nu(k)t}\right], \tag{7.49}$$

where we have omitted the ground state dipole and continuum-continuum transitions and and set $a_0 = 1$, as in (7.37). The spectrum $S(\omega)$ is given by

$$S(\omega) \propto \omega^2 |\widetilde{P}_z(\omega)|^2, \tag{7.50}$$

with the Fourier transform

$$\begin{aligned}\widetilde{P}_z(\omega) &= \int \mathrm{d}t \int \mathrm{d}k\, a(k)\langle 0,\theta|z|k\rangle \mathrm{e}^{-\mathrm{i}(\nu(k)-\omega)t} \\ &= (2\pi)\int \mathrm{d}k\, a(k)\langle 0,\theta|z|k\rangle \delta(\omega - k^2/2) \\ &= (2\pi)\frac{a(k[\omega])}{|k[\omega]|}\langle 0,\theta|z|k[\omega]\rangle, \quad k[\omega] = \sqrt{2\omega}\,.\end{aligned} \tag{7.51}$$

From this, the dipole matrix element $\langle 0, \theta | z | k \rangle$ can be recovered, provided one knows $a(k)$. This information is obtained by performing a second measurement on a reference atom, where $\langle 0_{ref} | z | k \rangle$ (no θ-dependence due to spherical symmetry) is known from theory and which has the same I_p as the molecule. One assumes that $a(k)$, which characterizes the ionized wave packet, does not depend on the detailed structure of the parent orbital, but only on I_p. The harmonic signals of the sample and the reference are related by

$$\begin{aligned} \frac{S(\omega)}{S_{ref}(\omega)} &= \frac{|a(k[\omega])\langle 0, \theta | z | k[\omega] \rangle|^2}{|a(k[\omega])\langle 0_{ref} | z | k[\omega] \rangle|^2} \\ &= \frac{|\langle 0, \theta | z | k[\omega] \rangle|^2}{|\langle 0_{ref} | z | k[\omega] \rangle|^2}. \end{aligned} \tag{7.52}$$

In this way, $\langle 0, \theta | z | k \rangle$ is measured as a function of θ and the orbital $|0\rangle$ is reconstructed.

The success of this prescription relies on several questionable assumptions:

1. In the form described it assumes that the ionization rate does not depend on the molecule's orientation. While for nitrogen this was checked in an experiment [108], this does not necessarily hold for other molecules. Probably this can be corrected for, but it requires additional measurements.

2. It assumes that the electron wave packet can be represented by plane waves of a single propagation direction ($\vec{k}$-direction).

3. It assumes that the electronic wave packet created by the laser field depends only on the ionization potential of the parent orbital (and on the laser pulse), but not on its shape. This hypothesis, often expressed succinctly as "all tunnels are the same", needs to be modified, as some features of the orbital, such as nodal planes, survive in the momentum distribution of the tunneled electrons by simple symmetry considerations.

4. Finally, it makes the major assumption that only one particle participates in HHG and that the process is completely determined by something which can be considered as a single-electron orbital. It will be shown in this thesis, that the concept of a single-electron orbital cannot be maintained within the context of HHG.

8 Electron distributions of the recollision current

8.1 Rescattering electrons – a definition

In this chapter, we will investigate possible multi-electron effects in the first two stages of the 3-step model, ionization and propagation. Extracting information about the bound orbital from harmonic radiation vitally relies on a knowledge of the recolliding electron wave packet. Considering its importance, little attention has been paid to the structure of an electron wave function produced by tunnel ionization in the laser field. The reason may be a conceptual one, as in a strong field there is no rigorous distinction between bound parts of the wave function and the wave function "after" tunneling.

The Hamiltonian with a (dc) field has a strictly continuous spectrum and all eigenfunctions including the approximate bound states are infinitely extended and not normalizable. When the field is strong, even approximate bound states cease to be clearly identifiable. If one decomposes an exact solution of the TDSE with a field into field-free bound and scattering states, one observes transitions between bound and scattering states, of which a large part is reversible. Depending on the system parameters, these virtual transitions may largely exceed the final ionization. They can be partly associated with adiabatic distortions of the wave function in the field, but their ultimately unphysical nature is betrayed by their gauge dependence. The discussion about the "correct" gauge for the SFA derives from this ambiguity. In SFA, the bound part of the wave function is *chosen* as the field-free initial electron orbital, but the physical meaning of this orbital in the presence of the laser field depends on the gauge. As the reversible bound-continuum transitions appear generally less pronounced in length as compared to velocity gauge, length gauge can be considered the better choice for an approximate decomposition.

The physical reason for the difficulties to spectrally distinguish bound from rescattering electrons is the coherence of the two parts of the wave function: where they overlap, amplitudes add up and merge into a single, indistinguishable entity. This difficulty does not arise when one 'observes' electrons at a distance from the bound system, where all more strongly bound parts are exponentially damped. This amounts to taking the rescattering picture seriously and counting only those electrons that had been removed to a large distance before they reappear near the bound electrons.

We implement this idea as follows: at time t_0 the solution $\Psi(\vec{r}_1, \ldots, \vec{r}_f; t_0)$ of the multi-electron TDSE is multiplied by a probe function $M_{z_0}(\vec{r}_1)$ which is localized at a distance z_0 from the bound system measured in the polarization direction. This

probe function approximates a plane where we measure intensity and momenta of the electrons as a function of time. Because of the indistinguishability of the electrons it suffices to consider only a single electron coordinate, and for simplicity, we write now only $\Psi(\vec{r},t)$. The criteria for the choice of M_{z_0} will be discussed below. The probed wave function part $M_{z_0}(\vec{r})\Psi(\vec{r},t_0)$ can then be propagated further by the TDSE

$$\mathrm{i}\,\frac{\partial}{\partial t}\chi_{t_0}(t) = H(t)\chi_{t_0}(t), \qquad \chi_{t_0}(t_0) = M_{z_0}\Psi(t_0) \tag{8.1}$$

or it can be converted to a Wigner distribution and propagated classically:

$$W_{t_0}(\vec{r},\vec{p},t) = \frac{1}{2\pi}\int \mathrm{d}^3\xi\, \chi^*_{t_0}\left(\vec{r}-\frac{\vec{\xi}}{2},t\right)\chi_{t_0}\left(\vec{r}+\frac{\vec{\xi}}{2},t\right)\mathrm{e}^{\mathrm{i}\,\vec{p}\cdot\vec{\xi}} \tag{8.2}$$

$$\frac{\partial W_{t_0}}{\partial t} = \frac{\partial W_{t_0}}{\partial \vec{p}}\cdot\frac{\partial V}{\partial \vec{r}} - \vec{p}\cdot\frac{\partial W_{t_0}}{\partial \vec{r}} \tag{8.3}$$

By integrating over all probe times t_0

$$\Phi_r(\vec{r},t) = \int \mathrm{d}t_0\, \chi_{t_0}(\vec{r},t), \tag{8.4}$$

or

$$W_r(\vec{r},\vec{p},t) = \int \mathrm{d}t_0\, W_{t_0}(\vec{r},\vec{p},t), \tag{8.5}$$

one obtains the rescattering part of the wave function and a classical rescattering beam of electrons, respectively, from which time, space and momentum distributions 'on target', i.e. at $z = 0$, are calculated.

The probe distance z_0 and the shape of the mask function are unphysical parameters on which our conclusions must not depend. The significance of these parameters was investigated by my co-worker Xinhua Xie [105]. Here we will only summarize his findings and general considerations:

(i) To distinguish clearly between bound system and rescattering electrons, the probe should be at sufficient a distance to damp out the bound wave function. We must, however, make a compromise, because only electrons with high momentum will reach the barrier at large distance, so we will lose information on the low-energetic end of the spectrum.

(ii) The rescattering current depends only weakly on the width of the probe function.

(iii) In the direction perpendicular to laser polarization, the probe function can be chosen to be rather broad or even infinite without causing overlap with the bound system, thus obviating the need for an unphysical restriction.

The unphysical nature of the probe function also introduces gauge dependence into the present procedure: the Fourier transform of $M_{z_0}\Psi$ refers to the canonical momentum, which coincides with the physical momentum in length gauge, but contains a time-dependent boost in velocity gauge. The gauge dependence, however, is much smaller than the dependence on the probe width.

Finally, we mention that a different approach to identifying the rescattering current was presented in [96]: The authors separate the electron wave packets ionized during each half cycle and analyze them in terms of energy and angular momentum eigenstates of the field-free Hamiltonian with ingoing and outgoing boundary conditions. Our method offers the advantage that it is easily applied to multi-electron systems, as well.

8.2 Atomic vs. molecular structure and correlation

We investigate to which extent the electron distributions are affected by electron correlation and molecular structure. The single-electron momentum distribution as probed by M_{z_0} for a general f-electron wave function is

$$w(\vec{p},t) = \int \mathrm{d}^3 r_2 \cdots \mathrm{d}^3 r_f \, |\mathcal{F}_1[\Psi](\vec{p},\vec{r}_2,\ldots,\vec{r}_f;t)|^2, \tag{8.6}$$

$$\mathcal{F}_1[\Psi](\vec{p},\vec{r}_2,\ldots,\vec{r}_f;t) = \int \mathrm{d}^3 r_1 \, \mathrm{e}^{-\mathrm{i}\,\vec{p}_1\cdot\vec{r}_1} \, M_{z_0}(\vec{r}_1)\Psi(\vec{r}_1,\ldots,\vec{r}_f;t). \tag{8.7}$$

We use model systems that mimic some of the aspects of the Ar atom and N_2 molecule: there are two active electrons in a 3D model potential whose parameters are adjusted to provide ionization potentials that agree with those of the Ar and N_2 molecule. The internuclear distance for the model molecule is fixed at at distance of 2.8, somewhat larger than the equilibrium distance of N_2, and the molecular axis is aligned with the laser polarization. It should be mentioned that this misses several important aspects of the electronic structure of the real systems, namely, our outer orbitals have no nodes, are always σ-type, and, in the case of the molecule, we cannot rotate the molecular axis relative to laser polarization.

The TDSE for the correlated 2-electron system is solved using MCTDHF in 3D with enforced cylindrical symmetry. We consider only spin singlet states, which means that the spatial wave function is symmetric under exchange of the two particles. The orbitals are restricted to cylindrical symmetry, i.e. they do not depend on the azimuthal angle.

We first investigate the importance of including correlation effects in the ionization of Ar by a single cycle FWHM laser pulse with a peak intensity of 3×10^{14} W cm^{-2}. and $\lambda = 800$ nm. The probe function with a FWHM of 8 was placed at a distance of $z_0 = 15$. Fig. 8.1 shows the momentum spectrum $w(p_z,t)$ in the z direction at three different probe times $t_0 = 0.5$, 1.17 and 1.5 fs (0.19, 0.44 and 0.56 optical cycles) after the laser field reaches the peak field strength. The importance of correlation effects is estimated by comparing calculations with $n = 2$ (ordinary TDHF) and 8 spatial orbitals ϕ_j. As explained in chapter 6, the *total* ionization yield depends on correlation. For the comparison, we normalized to equal total yield and integrated over the perpendicular momenta. Near the highest densities, we find only small differences between momentum distributions from the Hartree-Fock and the correlated calculation.

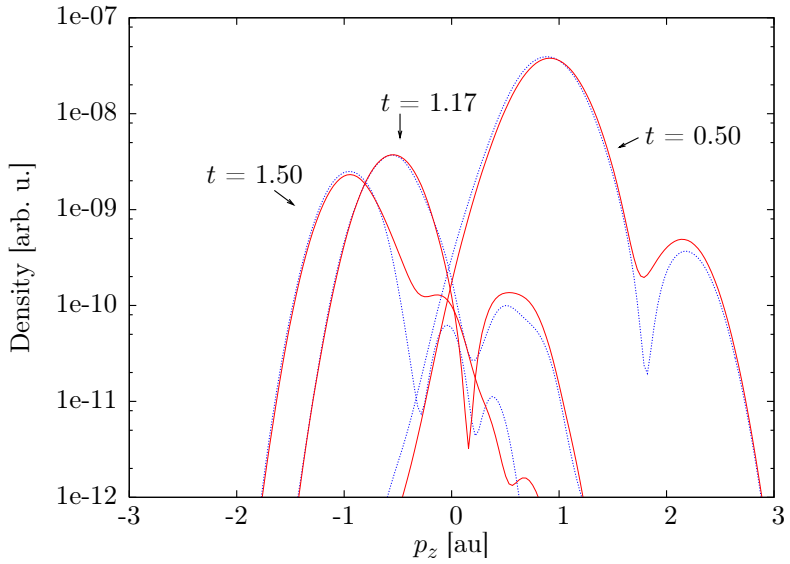

Figure 8.1: The effect of electron correlation on the rescattering electrons: electron momentum distributions as probed at $z_0 = 15$ at times $t = 0.5, 1.17$ and 1.5 fs for a model atom with two active electrons and the ionization potential of Ar ($I_p = 0.58$). MCT-DHF calculations with full correlation (solid red line) and in (single-configuration) time-dependent Hartree-Fock (dotted blue line). The curves are normalized to compensate for the different ionization rates in the two approaches.

Whether such differences would affect the details of a reconstruction that is based on a single active electron picture remains to be investigated.

In fig. 8.2 we compare rescattering electron spectra for the atomic and the molecular model systems. The differences between the two systems are comparable to those due to correlation. This is consistent as clearly the correlation effects in the two systems are radically different. Again the effect is small but may be quantitatively important for rescattering imaging.

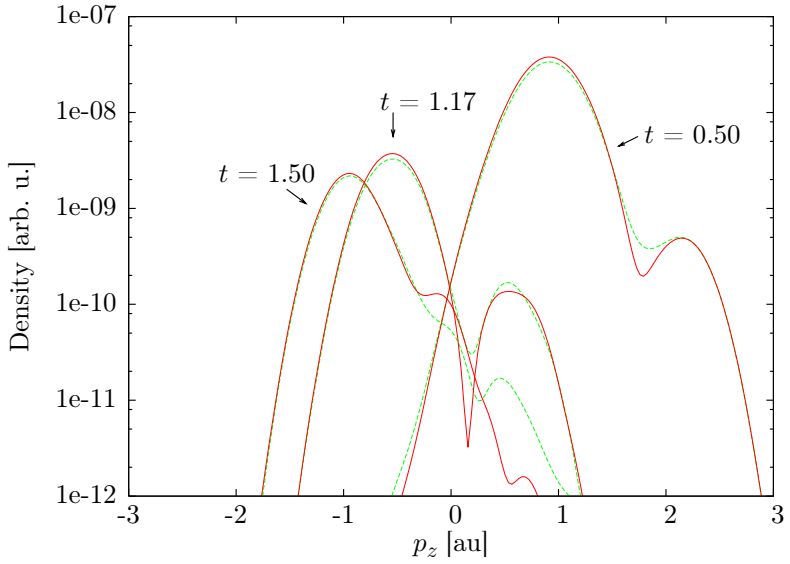

Figure 8.2: Molecular effects on rescattering: electron momentum distribution as probed at $z_0 = 15$ for a model Ar atom (solid red line) vs. a model N_2 molecule with the molecular axis aligned with the laser polarization (dashed green line).

9 Core polarization effects in molecular HHG

By design of the SFA, be it in single active electron approximation or in its multi-electron extensions, the electronic structure is considered to remain static without significant polarization by the laser field. We go beyond this assumption and investigate the effect of polarization of the ionic core by the driving laser field on the harmonic emission spectrum. We solve the time-dependent Schrödinger equation for diatomic model molecules with 2 and 4 active electrons using MCTDHF, and compare results with several single-electron models of increasing complexity. We will show that core polarization profoundly changes the harmonic response thus excluding any single-electron based description of the details of the harmonics. Conversely, *dynamical* multi-electron effects must be included for the reconstruction of electronic structure from the harmonic response.

9.1 Multi-electron molecules in a laser field

9.1.1 Model molecules

The Hamiltonian for multi-electron molecules in a laser field is of the general form (4.1). We choose homonuclear, diatomic molecules with an internuclear distance of $|\vec{R}| = 2.8$ for our calculations. Only a few outer electrons are simulated explicitly, while inner shell electrons are accounted for by a screened nuclear Coulomb potential of the form

$$V_{\mathrm{n}}(\vec{r}) = V_1(|\vec{r} - \vec{R}/2|) + V_1(|\vec{r} + \vec{R}/2|) \tag{9.1}$$

with the potential for one nucleus being

$$V_1(r) = \frac{Z}{r} + \alpha \frac{\mathrm{e}^{-\beta r}}{r} \tag{9.2}$$

The charge Z on each nucleus is equal to half the number of active electrons. The screening parameters α and β have been adjusted such as to yield the ionization potential $I_{\mathrm{p}} = 0.58$ (the same as N_2).

For homonuclear diatomic molecules, the electronic orbitals can be characterized by their symmetry properties with respect to inversion about the origin: the lowest orbital is of gerade, and the next higher orbital is of ungerade type. We studied systems with $f = 2$ and 4 active electrons. For the 2-electron system, in the singlet spin state both

Symmetry	2e-gg	2e-gu	4e	2e-atom
g	−0.594	−0.788	−0.781	−0.604
u		−0.586	−0.595	

Table 9.1: Hartree-Fock orbital energies of the atomic and molecular systems.

	2e-gg	2e-gu	4e	2e-atom
TDHF	0.082	0.079	0.073	0.041
MCTDHF	0.182	—	0.084	0.062
1e-TDSE	0.077	0.073	0.071	0.045

Table 9.2: Sum of ionization and excitation probability in TDHF, MCTDHF and 1e-TDSE after passage of the pulse.

electrons occupy a gerade orbital (we abbreviate this system by 2e-gg), while in the triplet spin state, gerade and ungerade orbital are occupied by one electron each (2e-gu system). For the 4-electron system, two electrons occupy the gerade orbital, and the other two the ungerade orbital (4e system). For comparison, we have also calculated harmonic spectra for a 2-electron atom with the same I_p as for the molecules, the same general form of nuclear potential, and the same laser parameters.

In table 9.1, we list the Hartree-Fock orbital energies for our model systems. To the extent that the HF energies characterize the molecule's electronic structure it is worth noting that the energy spacing between the u and g levels of about $\Delta E \approx 0.2$ is close to the value for CO_2 with $\Delta E = 0.21$, while being in between N_2 ($\Delta E = 0.06$) and O_2 ($\Delta E = 0.28$). Thus, while not meant to represent a specific molecular species, the characteristics of our systems are clearly in the typical range for small molecules.

The laser pulse has linear polarization parallel to the internuclear axis, a carrier wavelength of 800 nm ($\omega = 0.057$) and a $\cos^4$-shaped envelope for the vector potential $\vec{A}(t) = \hat{e}_R A(t)$ with a FWHM of 1 optical cycle:

$$A(t) = A_0 \cos^4\left(\frac{\pi t}{2\sigma}\right) \sin\omega t, \quad \sigma = \frac{\pi T}{4 \arccos\left(\frac{1}{\sqrt{4}\,2}\right)}, \quad T = \frac{2\pi}{\omega}. \tag{9.3}$$

The rather short pulse duration and the pulse shape are dictated by computational requirements. The $\cos^4$-envelope has finite support and a continuous third derivative everywhere. The latter is needed for calculating the dipole acceleration in the Lewenstein model. The electric field peaks at $t = 0$ (see fig. 9.1). The laser intensity was $I = 3 \times 10^{14}$ W cm^{-2}, which causes between 6 and 18% ionization (see table 9.2).

In our simulations we use cylindrical coordinates (z, ρ) and neglect the dependence on the azimuthal angle. The dimensions of the simulation box ranged from 200 to 300

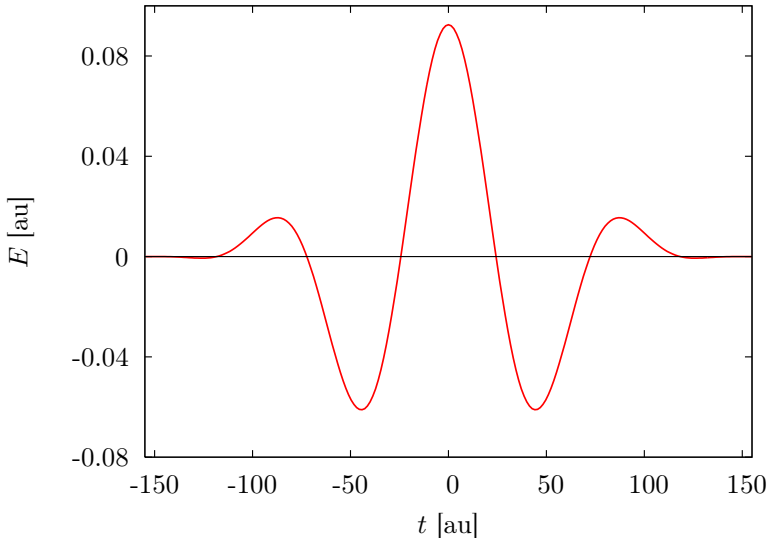

Figure 9.1: Electric field of the laser pulse with $\cos^4$ envelope and intensity $I = 3\times10^{14}$ W cm^{-2}.

au in the z-direction (polarization direction), and from 40 to 60 au in ρ, with between 2.5 and 5 discretization points per au.

9.1.2 Length vs. velocity vs. acceleration form of the dipole operator

The harmonic response of a system of electrons to a laser field is proportional to the acceleration of the system's dipole, which can be written in

- length form

$$\ddot{\vec{P}}(t) = \frac{\mathrm{d}^2}{\mathrm{d}\,t^2}\langle\Psi(t) \mid \vec{r} \mid \Psi(t)\rangle, \tag{9.4}$$

- velocity form

$$\ddot{\vec{P}}(t) = \frac{\mathrm{d}}{\mathrm{d}t}\left\langle\Psi(t)\,\middle|\,\frac{1}{\mathrm{i}}\vec{\nabla} + \vec{A}\,\middle|\,\Psi(t)\right\rangle, \tag{9.5}$$

- acceleration form

$$\ddot{\vec{P}}(t) = -\langle\Psi(t) \mid \vec{\nabla}V + \vec{E} \mid \Psi(t)\rangle. \tag{9.6}$$

The equivalence of the three forms is a special case of the Ehrenfest theorem and relies on

(a) the standard quantum mechanical commutation relations and the fact that the Hamiltonian has the standard form of kinetic energy plus potential,

(b) the fact that the wave functions are *exact* solutions of the Schrödinger equation, and

(c) the fact that the Hamiltonian is hermitian.

For the computations and models used here, these conditions are violated in several respects:

(i) the discrete approximation of differential operators does not exactly reproduce the commutation relations,

(ii) the complex absorbing potential V_{cap} violates hermiticity, and

(iii) the approximate wave functions of some of our simplifying models do not solve a standard Schrödinger equation consisting of a Laplacian representing kinetic energy plus potentials in the form of multiplication operators, and thus the commutation relations with H are not the usual ones (see sections 9.2.1 SFA and 9.3.1 effective 1e-TDSE).

It turns out that in our case absorption at the boundaries and discretization errors only lead to minor differences in spectra obtained in the length and velocity forms: when we use the MCTDHF wave functions, spectra calculated in either form – although differing by a factor of up to 10 for the lowest 20 harmonics – agree within 5% for all higher harmonics. The discrepancies at lower harmonics can be ascribed to violation of hermiticity by the absorbing potential, which do not affect higher harmonics as they are generated near the nuclei. However, for our model systems with non-standard Hamiltonians rather large discrepancies arise throughout the whole spectrum. The gauge-noninvariance of SFA is well-known and has been extensively demonstrated (see sec. 7.1.3). For our effective 1e-TDSE model (sec. 9.3.1), the differences between length and velocity gauge for some of the molecular systems reach up to one to two orders of magnitude even in the relevant cutoff region.

The choice of the dipole operator depends on which properties of the true solution are best reproduced by the approximate solution. The length form depends only on the electron density and emphasizes contributions from larger distances. The velocity form depends on the momentum distribution of the electrons irrespective of their location in space. This favors the length form of the operator for the strong field approximation, which becomes more accurate at larger distances, where the influence of the molecular potential is weaker. Similar arguments hold for the other models used in the present paper, which do not aspire to accurately reproduce details of the molecular potential. For this reason and to allow a consistent comparison between models, here we always show the harmonic spectra calculated in the length form.

In [27] a third point of view was taken, namely that the acceleration operator $\vec{\nabla}V$ should be considered as fundamental. The acceleration operator more strongly depends on regions of the electronic wave function near the singularities of the nuclear potential, which are dominated by multi-electron effects and where for HHG the dynamics of the electrons is important. While our MCTDHF calculations do include these effects, all

models using only a single active electron by definition exclude them. For this reason again we prefer the length form over the acceleration form for the present study.

9.2 Results

Fig. 9.2 shows the harmonic spectra for our model systems obtained with correlated MCTDHF wave functions using up to $n = f + 4$ orbitals. The overall shape of the spectra is similar in all cases. Due to the extremely short pulse duration there is a double plateau structure. The more intense plateau at lower harmonic numbers corresponds to ionization by the peak of the field with lower acceleration by the subsequent smaller field half-cycle (cf. fig. 9.1). The lower intensity plateau reaching to harmonic numbers of ~ 45 originates from ionization one half-cycle before peak field strength.

We verified the convergence of our calculations with respect to box size, discretization and number of orbitals n. Varying the extent of the box in laser polarization direction between 200 and 300 au has considerable effects only on the harmonic orders $\lesssim 20$. The dependence of our observables on the number of orbitals n is of physical interest as it provides information about the degree of correlation in the molecule, i.e. the number of different Slater determinants needed for an accurate description of the multi-electron wave function.

In fig. 9.2 we also included the spectra obtained from uncorrelated calculations ($n = f$, TDHF, blue) and weakly correlated calculations with $n = f + 2$ (green). The agreement between $n = f + 2$ and $n = f + 4$ for the 2e-gg molecule and the 2e atom shows that the spectra can be considered as converged for all practical purposes. Convergence of the 4e spectrum has not been reached, but the main qualitative features at high harmonic orders are preserved.

The rather good agreement of harmonic spectra does not necessarily imply that the TDHF wave function reflects other important properties of the true, correlated wave function. Fig. 9.3 shows the sum of ionization and excitation yields as a function of n. While for the 2e-gg molecule correlation leads to a strong increase in ionization plus excitation, for the 2e atom and the 4e molecule ionization remains almost constant. This is consistent with the greater importance of correlation for the ionization of smaller molecular systems (see chapter 6).

9.2.1 Comparison with the Lewenstein model

In sec. 7.1.2 we described the Lewenstein model, pointing out that it disregards excited states and therefore does not account for bound-state dynamics of the molecule in the laser field, and that in its original form it also neglects any influence of the binding potential on the scattering states. This amounts to representing the continuum by plane wave Volkov states.

We use the Lewenstein formula in the form (7.45), after integrating over the wave vectors $\vec{k}$ of the continuum electrons in stationary phase approximation. Time integration is performed numerically. Figures 9.4 show the spectra obtained in the Lewen-

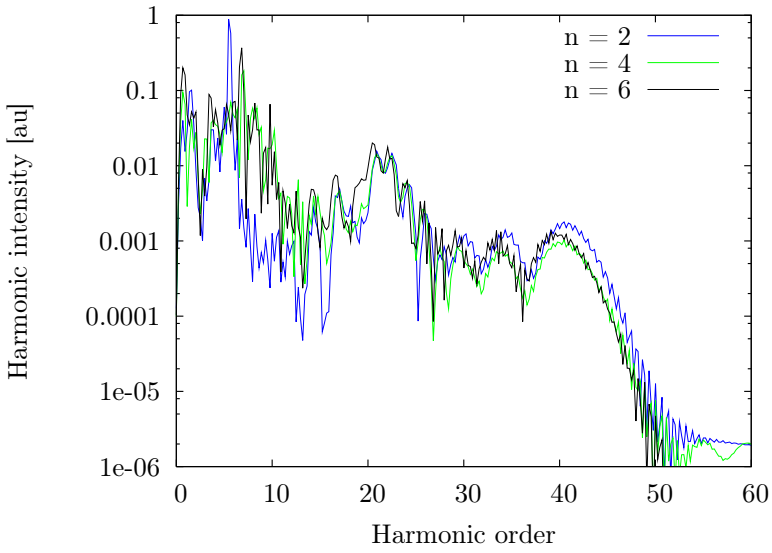

(a) 2e-gg molecule

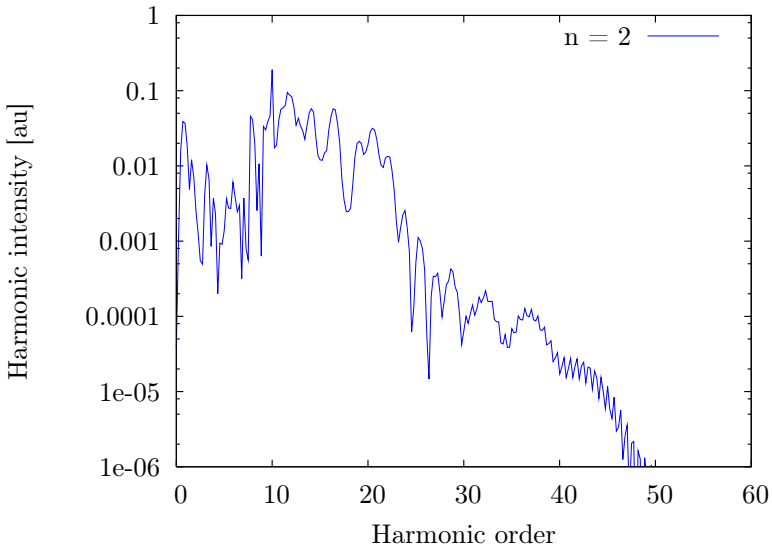

(b) 2e-gu molecule (only TDHF)

Figure 9.2: Harmonic spectra from MCTDHF calculations with increasing number of orbitals n (i.e. allowing for more correlation).

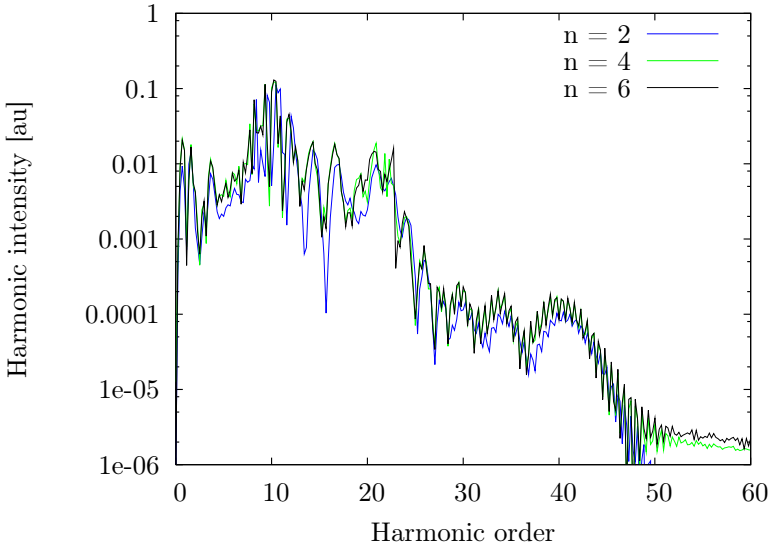

(c) 2e atom

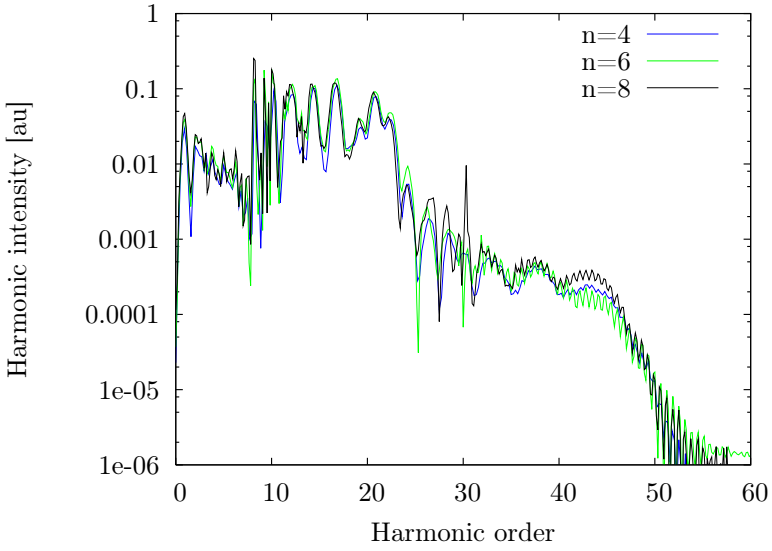

(d) 4e molecule

Figure 9.2: (continued)

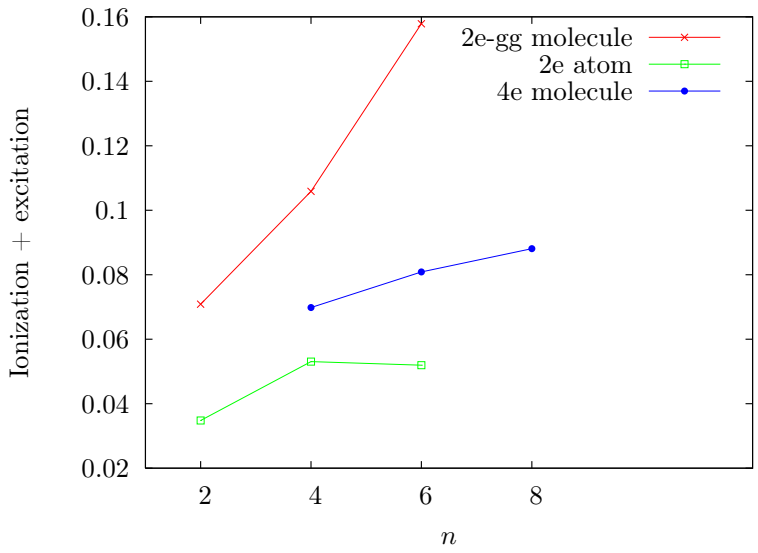

Figure 9.3: Sum of ionization and excitation for MCTDHF calculations with increasing number of orbitals n.

stein picture for our model systems in comparison with MCTDHF. Only the overall plateau structure and cutoffs, but neither harmonic intensities nor the spectral shape are reproduced correctly for the molecular systems. By contrast, for the 2e atom good agreement in both aspects is achieved.

For a multi-particle system, the choice of an initial *single-electron* state $|0\rangle$ – suited for the physical problem under consideration – is not unique. Possible choices are the highest occupied molecular orbital of a HF wave function or the Dyson orbital (see sec. 9.3.3 for a discussion of the Dyson orbital). This choice will result in different dipole matrix elements $d_z(\vec{k})$ in the Lewenstein formula (7.45). As was shown in [82], the difference between the dipole elements of HF- and Dyson-orbitals is only of second order in the electron-electron interaction, using multi-particle perturbation theory. Although a Dyson orbital drawn from a correlated calculation changes the Lewenstein spectrum of the 2e-gg molecule near the cutoff, it in no way leads to better agreement with the MCTDHF result. For the 2e atom and 4e molecule, there is no difference between Dyson and HF orbitals. We therefore omit the HF curve in fig. 9.4.

9.3 Discussion

9.3.1 Accounting for the molecular potential

One of the known shortcomings of the Lewenstein model is the absence of the molecular binding potential: neither dynamics of excited states nor scattering from the molecular potential are included. This affects both the ionization and the recombination step in

HHG.

In order to assess the importance of these effects for our systems, we construct a single-electron Hamiltonian whose initial state coincides with the Dyson orbital, but which includes excited states and scattering from the molecular potential. It is based on the assumptions that a single active electron moves in the potential of a frozen ionic core and the Stark shift of the ground state is negligible. While the second of these assumptions seems quite reasonable, our results below will show that the ionic core cannot be considered as untouched by the laser field.

We start from a field-free single-electron Hamiltonian of the form

$$H_{\mathrm{m}} = -\frac{1}{2}\Delta - \frac{1/2}{|\vec{r} - \vec{R}/2|} - \frac{1/2}{|\vec{r} + \vec{R}/2|} \tag{9.7}$$

which contains a molecular potential with screened point charges. We then choose the desired single-electron initial state orbital $|0\rangle$ and divide the Hilbert space into $\mathcal{H}_0 = \mathrm{span}(\{|0\rangle\})$ and its orthogonal complement. The effective Hamiltonian H_{eff} acts like H_{m} on the orthogonal complement of $\mathcal{H}_0$ and gives the desired ground state energy E_0 for $|0\rangle$:

$$H_{\mathrm{eff}} = E_0 P_0 + (\mathbb{1} - P_0) H_{\mathrm{m}} (\mathbb{1} - P_0) + E_z(t) z, \tag{9.8a}$$

$$P_0 = |0\rangle\langle 0|. \tag{9.8b}$$

The interaction with the field has been included here in length gauge, as the field-free molecular Hamiltonian H_{m} should not contain time-dependent terms. As the ground state energy we choose $-I_{\mathrm{p}}$ of the multi-electron system. For $|0\rangle$ we use the Dyson orbital, but very similar results are obtained with the highest occupied HF orbital. The one-electron TDSE can be easily solved for this model, which we denote by 1e-TDSE.

Fig. 9.4 also includes the 1e-TDSE harmonic spectra (red) obtained with the same orbital $|0\rangle$ as in the Lewenstein model (blue). We immediately see that the dynamics of bound and/or continuum states *does* play an important role in molecules. Magnitude, overall decrease with harmonic order, and the positions of the minima and cutoff in the spectrum all differ between the two models, although the variations are comparatively smooth. Again, however, the 1e-TDSE model works well for the high harmonics of the 2e-atomic system.

The 1e-TDSE model describes the ionization process reasonably well. Table 9.2 compares the sum of ionization plus excitation of TDHF, MCTDHF and 1e-TDSE for the 2 and 4 electron system. The agreement of the model with the TDHF calculation is better than 1%. The use of a Dyson orbital derived from correlated ground state wave functions instead of from HF wave functions for $|0\rangle$ in (9.8a) has little impact on the figures. However, in the multi-electron calculation of the 2e-gg molecule, correlation leads to a significantly enhanced ionization and excitation probability, which is not reproduced by 1e-TDSE. Comparing with the MCTDHF spectra of fig. 9.4 we see that in spite of the inclusion of the molecular potential and a good match with the outer electron's orbital, the 1e-TDSE model completely fails to reproduce the molecular high harmonic spectra in intensity as well as spectral shape.

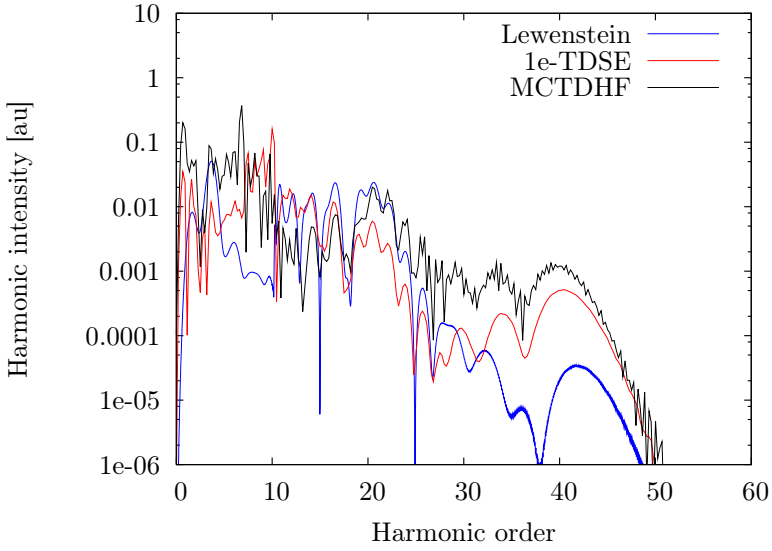

(a) 2e-gg molecule

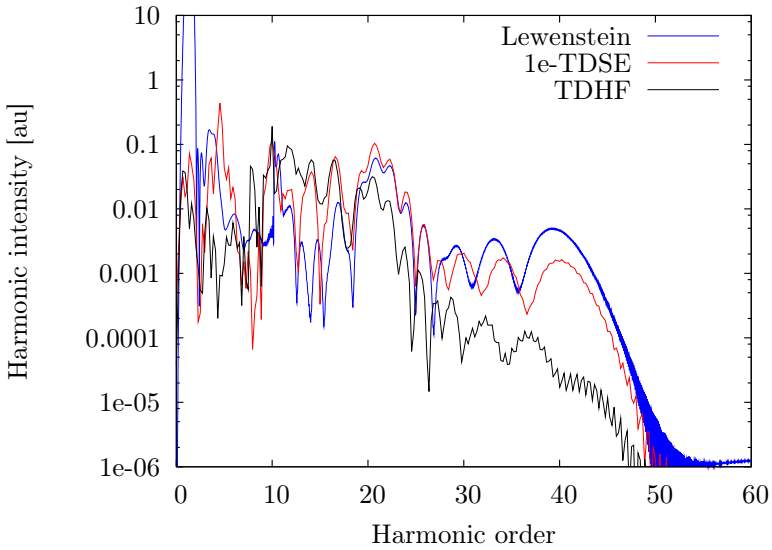

(b) 2e-gu molecule

Figure 9.4: Comparison of the harmonic spectra in the Lewenstein model (blue), 1e-TDSE (red) and MCTDHF (black).

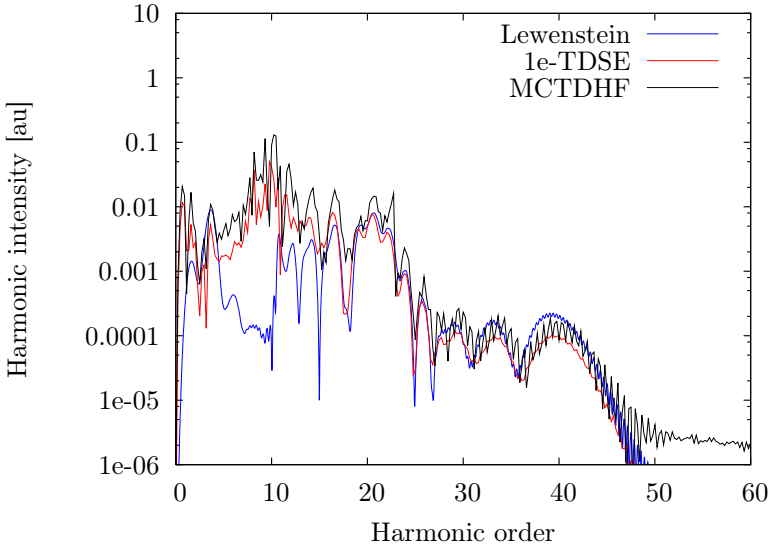

(c) 2e atom

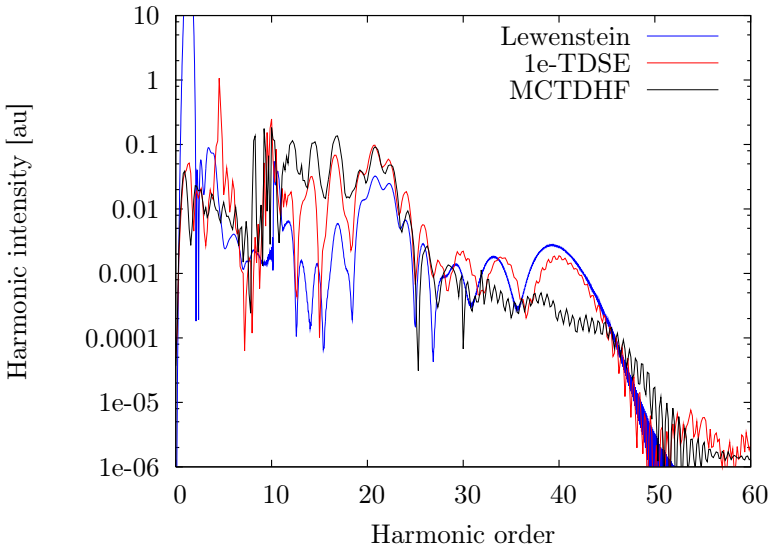

(d) 4e molecule

Figure 9.4: (continued)

One possible source for the discrepancy between MCTDHF and 1e-TDSE is ionization. We have seen that 1e-TDSE gives overall ionization yields only to within factors $\lesssim 3$ of the MCTDHF result, when correlation is included. However, even much larger correction factors to the overall ionization yield could not eliminate the difference in the spectral shapes. According to the three-step model, one important factor determining the spectral shape is the time structure of the re-collision current. In sec. 8.1, we have described a method to extract the current of recolliding electrons from the total wave function. Fig. 9.5 shows the momentum distribution of the electron currents at a distance $z_0 = 15$ with a FWHM of the Gaussian of 8.24 for different times during the pulse as obtained from the MCTDHF and 1e-TDSE wave functions. After multiplication by overall normalization constants between 0.40 and 0.90, which quite well reflect the errors in total ionization for the various system, electron momentum distributions at different times agree within 10% or better. We conclude that the time distribution of ionization is well described by the 1e-TDSE, though the magnitude is not. When we reason within the three-step model, this leaves only the recombination step as the source of error in the 1e-TDSE model.

9.3.2 Multi-electron corrections to the SFA

One important modification of the SFA has been introduced in [82, 70], where multi-electron effects were included in the recombination matrix element. In this case, the field-free bound state $|0\rangle$ is the multi-electron ground state $|\Psi_0\rangle$ itself, and the continuum states are written as products of the (field-free) ionic ground state $|\Psi_+\rangle$ and single-electron plane waves $|\vec{k}\rangle$. The total wave function for a spin singlet becomes

$$\Psi'_{\vec{k}} = \mathcal{A}\frac{1}{\sqrt{2}}(\Psi_+^{\uparrow}\chi_{\vec{k}}^{\downarrow} - \Psi_+^{\downarrow}\chi_{\vec{k}}^{\uparrow}), \tag{9.9}$$

where $\mathcal{A} = (1/\sqrt{f})(\mathbb{1} - \sum_{j=1}^{f-1} P_{jf})$ is the antisymmetrization operator, P_{jf} transposes the j-th and the f-th electron, and $\uparrow, \downarrow$ denote the $\pm\frac{1}{2}$ spin states. The dipole matrix element is given by

$$\vec{d}(\vec{k}) = \left\langle \Psi'_{\vec{k}} \,\middle|\, \sum_{l=1}^{f} \vec{r}_l \,\middle|\, \Psi_0 \right\rangle, \tag{9.10}$$

which can be evaluated further as [70]

$$\vec{d}(\vec{k}) = \sqrt{2}\,(\vec{d}_1 + \vec{d}_2), \tag{9.11a}$$

$$\vec{d}_1 = \langle \vec{k} \mid \vec{r} \mid \phi_D \rangle, \tag{9.11b}$$

$$\vec{d}_2 = -\sqrt{f} \sum_{j=1}^{f-1} \langle P_{jf}(\Psi_+\vec{k}) \mid \vec{r}_f \mid \Psi_0 \rangle, \tag{9.11c}$$

where ϕ_D denotes the Dyson orbital.

Fig. 9.6 shows the importance of these corrections for our molecules. Dipole matrix elements were calculated with the respective neutral and ionic MCTDHF wave functions. We see that the exchange correction can be very substantial, amounting to more than one order of magnitude in the case of the 4e system.

The exception is the 2e-gg system, for the simple reason that the exchange term d_2 nearly vanishes. It vanishes exactly in the HF case

$$d_z = 2\left\langle \phi\phi \;\middle|\; z_1 \;\middle|\; \frac{1}{\sqrt{2}}(\phi_+ k - k\phi_+) \right\rangle = \sqrt{2}[\underbrace{\langle\phi \mid z_1 \mid \phi_+\rangle}_{d_2=0} - \underbrace{\langle\phi \mid z_1 \mid k\rangle\langle\phi \mid \phi_+\rangle}_{d_1}], \quad (9.12)$$

since both the HF orbital ϕ and the ionic single-electron orbital ϕ_+ have gerade symmetry (z_1 refers to the z-coordinate of the first electronic orbital). The extra multi-configuration corrections remain small. The same remarks apply to the 2e atom.

Unfortunately, it is evident from comparing figures 9.4 and 9.6 that also the exchange-corrected Lewenstein model fails to reproduce the multi-electron solution, and it still does so by orders of magnitude. A failure with respect to overall harmonic intensity alone might have been ascribed to one of the known shortcomings of the Lewenstein model, namely incorrect ionization rates. What is more disturbing and can certainly not be explained in this way is the strong deviation in the spectral shape at high harmonic energies, as molecular orbital tomography [34] depends on the unambiguous understanding of the harmonic power spectrum (and phases).

9.3.3 Factoring the multi-electron wave function

In view of the failure of the previous models, we now attempt to directly extract a time-dependent single-electron function from the known multi-electron function such that the harmonic spectra agree for the two functions.

In the single-electron description one assumes that the movement of the electron that becomes ionized is on a different spatial and velocity scale from the electrons remaining closer to the nucleus. It may therefore be possible to write the total wave function as a product of a core $\Phi(x_1, \ldots, x_{f-1}; t)$ of electrons times a single-particle orbital $\phi(x_f; t)$ with proper antisymmetrization:

$$\Psi'(x_1, \ldots, x_f; t) = \frac{1}{N(t)}\mathcal{A}[\Phi(x_1, \ldots, x_{f-1}; t)\phi(x_f; t)]. \quad (9.13)$$

Note that, since Φ and ϕ are, in general, not orthogonal, we have to normalize by a time-dependent factor $N(t)$.

For the determination of the constituents Φ and ϕ two requirements should be met: (i) the product function should well approximate the true solution and (ii) the inactive electron part Φ should contribute little to our observable (the harmonic spectrum). To meet the first condition, ϕ is determined such that, given a particular Φ, Ψ' provides the best approximation to the true Ψ. Here, we define the best approximation as the one with the largest overlap $\langle\Psi|\Psi'\rangle$. Apart from this, the specific flavor of a particular model is introduced by Φ. Its choice depends on the physical process under

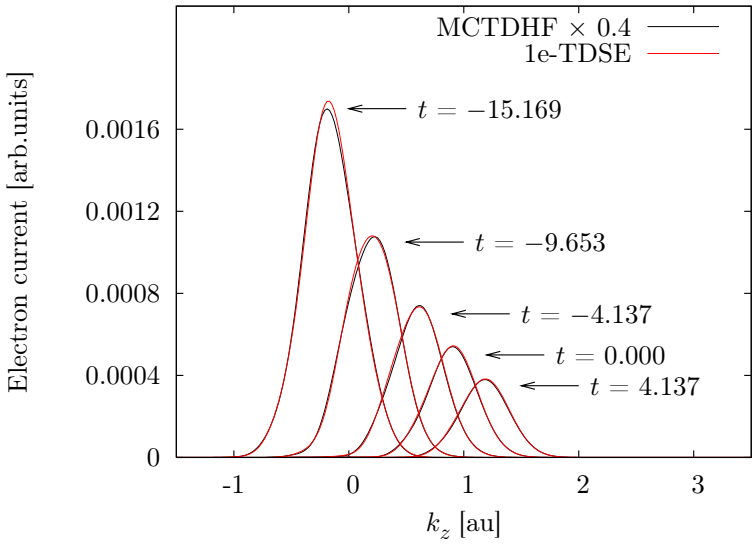

(a) 2e-gg molecule

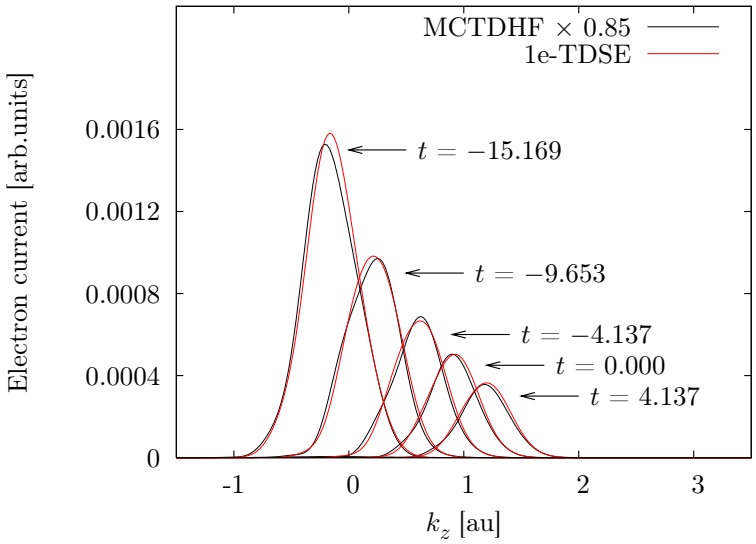

(b) 2e-gu molecule

Figure 9.5: Momentum distribution of the recollision electron current in the 1e-TDSE (red) model and MCTDHF (black) at 5 different times. The MCTDHF distributions were scaled by a factor such that they agree in magnitude with 1e-TDSE at $t = +4.137$. The time range covers about 20 au ($\sim$ 500 as).

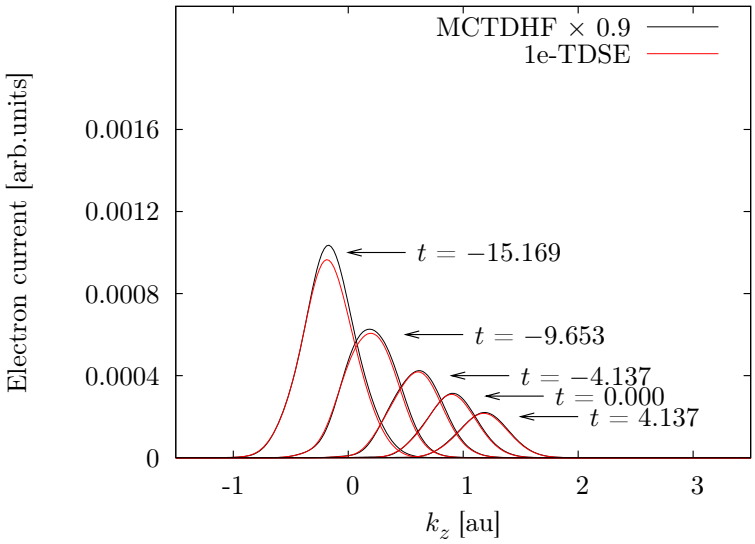

(c) 2e atom

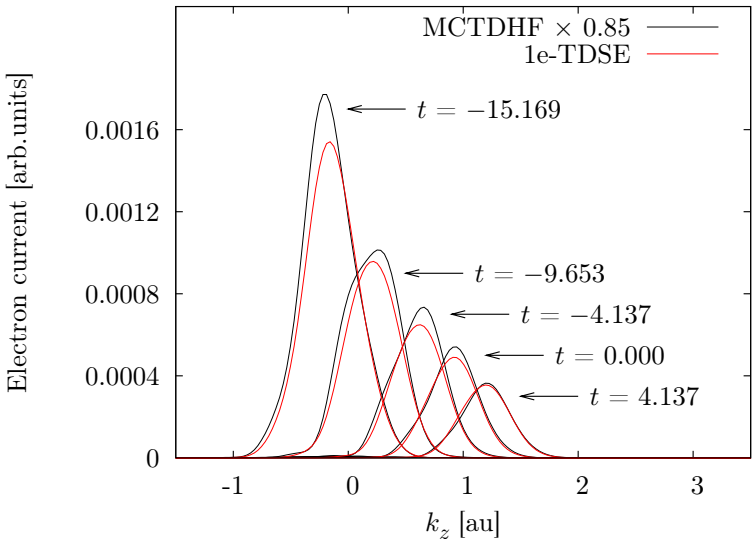

(d) 4e molecule

Figure 9.5: (continued)

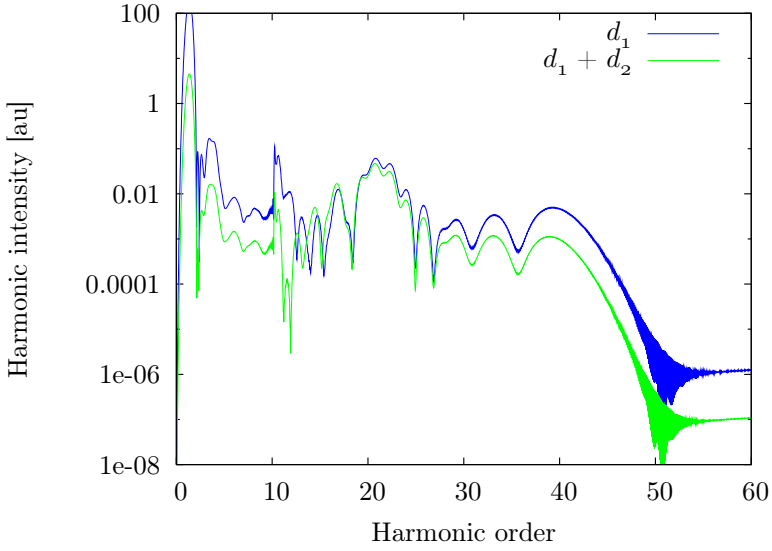

(a) 2e-gu molecule

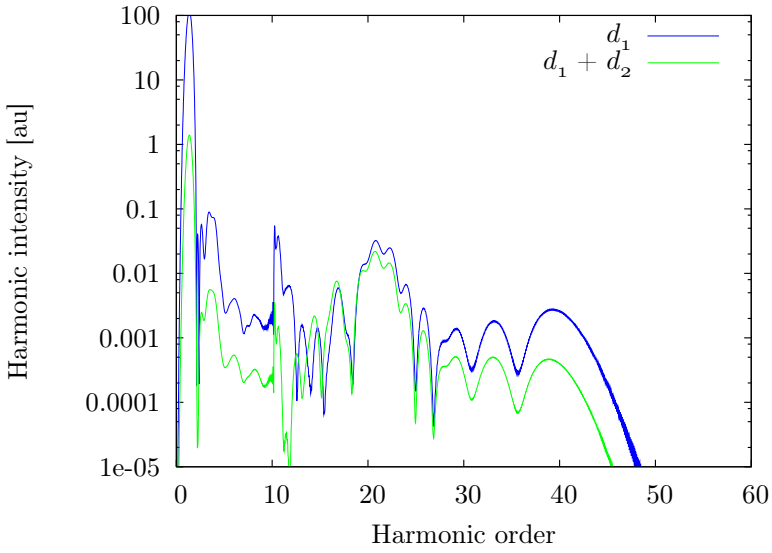

(b) 4e molecule

Figure 9.6: Comparison of harmonic spectra in the Lewenstein model without (blue, d_1) and with (green, $d_1 + d_2$) exchange terms.

consideration. For HHG a suitable choice seems to be the cationic wave function. In this case, ϕ is the Dyson orbital.

Technically, the Dyson orbital [67] is defined by the integral over the ionic coordinates

$$\phi_D(\vec{r}) = \sqrt{f} \int \mathrm{d}^3 r_1 \cdots \mathrm{d}^3 r_{f-1}\, \Psi_+^*(\vec{r}_1, \ldots, \vec{r}_{f-1}) \Psi(\vec{r}_1, \ldots, \vec{r}_{f-1}, \vec{r}), \tag{9.14}$$

for which we use the short notation

$$|\phi_D\rangle = \sqrt{f}\, \langle \Psi_+ \mid \Psi_0 \rangle\!\rangle. \tag{9.15}$$

The norm of the Dyson orbital $||\phi_D||$ (the 'pole strength'), is not necessarily equal to 1. Rather, the deviation from unity is a measure of how much the orbitals of the ion core change upon ionization. If it is impossible to satisfy requirement (i) with the ansatz (9.13), then the system is significantly correlated.

We consider two possible choices of core electron factor Φ:

1. The ion remains in its initial state (static), i.e. it is not significantly deformed by the laser pulse,

$$|\phi_D^{\mathrm{stat}}(q_f; t)\rangle = \sqrt{f}\, \langle \Psi_+(0) \mid \Psi_0(t) \rangle\!\rangle. \tag{9.16}$$

2. The ion is considerably polarized by the laser field and we need to include its correct time evolution:

$$|\phi_D^{\mathrm{dyn}}(q_f; t)\rangle = \sqrt{f}\, \langle \Psi_+(t) \mid \Psi_0(t) \rangle\!\rangle, \tag{9.17}$$

   where $\Psi_+(t)$ is the time-dependent ionic wave function.

Fig. 9.7 (left column) shows spectra obtained with the static and polarized ionic core. We see that polarization of the ionic core strongly affects the overall shape and intensity of the harmonic spectrum. As we have shown above, multi-electron corrections strongly affect the harmonic spectrum. It is therefore to be expected that even minor modifications of the inner shell electrons may strongly change the overall spectrum. Note that this change is not due to harmonic emission by the ion itself, which is by about two orders of magnitude lower than emission from the neutral (fig. 9.7, right column). The differences between static and polarized core factorizations are on a similar scale as the differences between the 1e-TDSE models and the MCTDHF result. It is intriguing that for all our models the high harmonic part of MCTDHF spectra is well approximated by the polarized core factorization. Interestingly, for the 2e atom, the factorized wave function leads to no improvement over the single-electron models (Lewenstein and 1e-TDSE), which actually yield better agreement in terms of harmonic intensity.

Fig. 9.7 (right column) shows, that the 'dynamical Dyson orbital' ϕ_D^{dyn} dominates the harmonic emission: in all cases, including the exchange corrections between ϕ_D^{dyn} and $\Psi_+(t)$ only slightly changes the harmonic spectrum. This means that we have

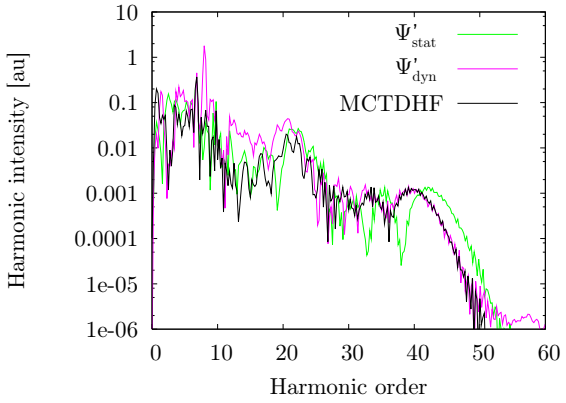

(a) 2e-gg molecule

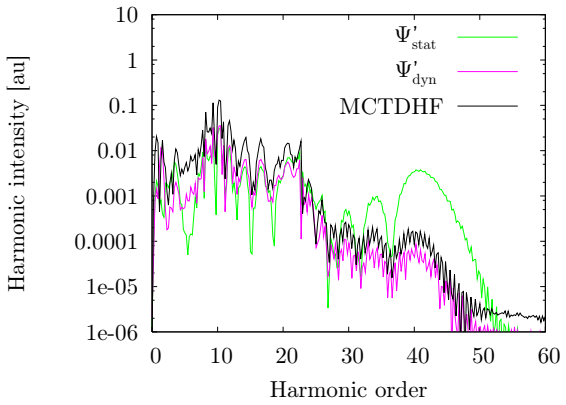

(b) 2e atom

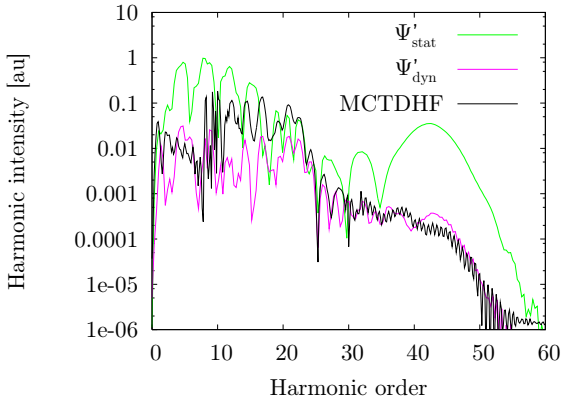

(c) 4e molecule

Figure 9.7: Comparison of harmonic spectra obtained by MCTDHF and from product wave functions as (9.13). The product wave functions with the static or dynamic ion core are denoted by Ψ'_{stat} and Ψ'_{dyn}, respectively. In the left column (a,b,c), Ψ'_{stat} (green) and Ψ'_{dyn} (magenta) are compared to the MCTDHF (black) solution.

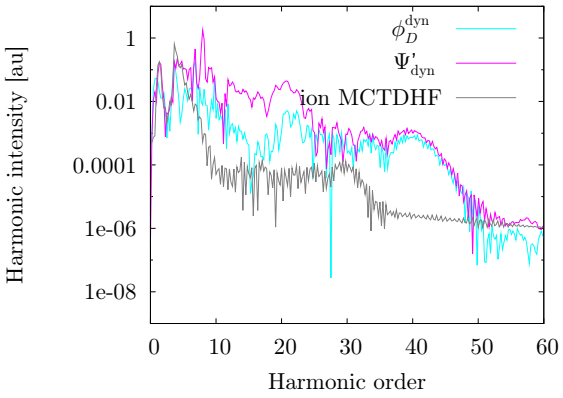

(d) 2e-gg molecule

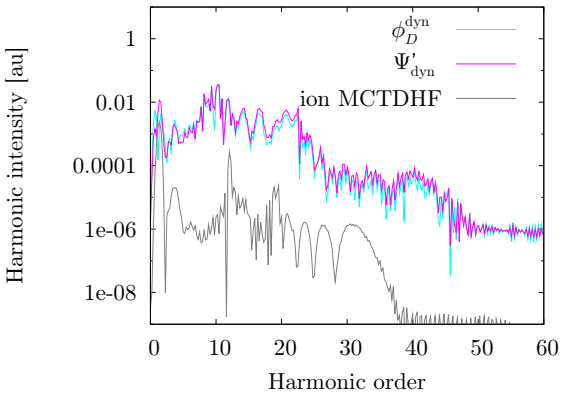

(e) 2e atom

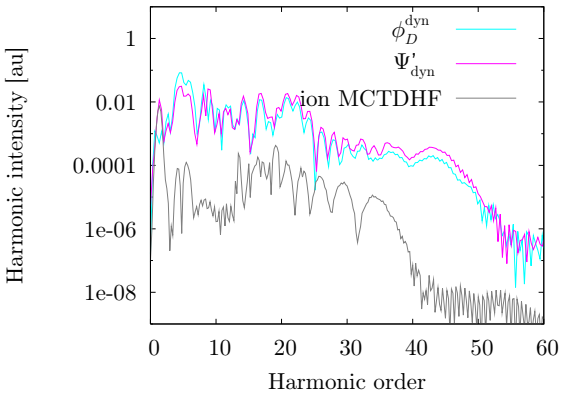

(f) 4e molecule

Figure 9.7: (continued) In the right column (d,e,f), we compare the Dyson orbital $\phi_D^{\rm dyn}$ (cyan) with the product wave function $\Psi'_{\rm dyn}$. For reference, the spectrum of the ion is also shown (gray).

indeed isolated the harmonic response of the system in a single-electron orbital and separated it from the background of the other electrons, as desired for a meaningful factorization. The spectra for the Dyson orbital are obtained from the dipole expectation value $\langle \phi_D^{\mathrm{dyn}} \mid z \mid \phi_D^{\mathrm{dyn}} \rangle$.

9.3.4 Accuracy and comparability of the calculations

As remarked in the discussion of the MCTDHF results (sec. 9.2) the convergence of spectra with respect to the number of orbitals (fig. 9.2) is not fully reached numerically, with changes remaining on the order of a factor of 2 in the worst case (4e molecule). Even so, this is considerably less than the observed deviations between MCTDHF and simpler models, which reach up to three orders of magnitude.

The importance of core-polarization effects derives from the in general strong contribution of the cross-matrix elements between the 'active' orbital and the core orbitals. This observation was originally made for the multi-electron corrected SFA [82, 70] and is corroborated here for the case when a frozen core is factorized out from the full MCTDHF wave function. The same procedure with the frozen core replaced with the polarized core systematically gives largely correct HHG spectra for all our model systems. In that case contributions from cross-matrix elements between the active single-electron factor and the core factor are small.

The success of the polarized core factorization, together with the failure of the static core factorization, also provides indirect evidence that both the ionic and the neutral wave functions are well described by MCTDHF for the purpose of the calculation of high harmonics spectra. All other features like frozen inner shell electrons, cylindrical symmetry, or fixed nuclei are common to all models. Therefore the comparison with MCTDHF allowed us to disentangle specific shortcomings of the single-electron models from the true multi-electron effects in HHG. The magnitude of these effects is linked to our specific molecular models. However, with key model parameters chosen in realistic ranges and calculations made in 3 dimensions, we expect effects on the same scale for real molecules.

9.4 Conclusions

We found strong indications that HHG is a genuinely *dynamic* multi-electron effect. Neither incorrect ionization rates nor the plane wave approximation, which could be remedied by more refined single-electron models, are responsible for the failure of SFA for our multi-electron model systems. We also conclude that in the present case the multi-electron effects cannot be described in the spirit of [82, 70] as the interaction of some frozen core with an active electron.

For these realistic 3D multi-electron molecular models, both the standard SFA and an advanced single-electron model that includes a phenomenological molecular potential completely fail to reproduce shape and intensity of the harmonic spectra. We could show that for our system parameters the ionization process is described with

satisfactory fidelity by the single-electron model, but recombination is grossly incorrect. The discrepancy is due to the large size of the multi-electron contributions to the recombination matrix element [70] and their sensitivity to the polarization of the ionic core by the laser pulse. A largely correct description of the higher part of the harmonic spectrum can be obtained when the full wave function is factorized into the polarized ion wave function times a single-electron factor. In the case of such a factorization, the cross-terms between the polarized ion and the 'active' electron contribute little and the single-electron factor already produces a roughly correct spectrum. In this very general sense, one might argue that HHG from molecules is still a single-electron process. However, the time evolution of this factor wave function implicitly includes interactions with the polarized core-electron wave function. In particular, any dynamical description of its time evolution must include terms accounting for the time-dependent exchange and correlation. In other words, there is no dynamical equation of a *single* particle that would have as its solution the desired "dynamic-core" single-electron orbital. Rather, it can only be extracted afterwards from a *multi*-electron calculation.

At present, due to computational limitations, we cannot conduct a similar calculation *ab initio* for systems most frequently used in experiments like N_2 or CO_2. Even within our model systems, confidence in the correctness of the results is based on an analysis in terms of various models rather than systematic convergence studies, as these would require larger computer resources than presently available to us. Still, we believe that the rather realistic nature of our MCTDHF simulations raises serious questions about the possibility of tomographic imaging for general systems that must be decided before the method can be put to practical use.

Part IV

Forest fire

10 Laser-induced breakdown in transparent materials

Ultrashort laser pulses of femtosecond duration allow materials to be subjected to unprecedented laser intensities [1]. From a practical point of view, the study of laser-induced breakdown and damage in transparent materials at these intensities is interesting because understanding damage mechanisms may help in constructing optics for laser systems with a higher damage threshold, which is currently limiting peak laser intensities. Another interesting application is micromachining of materials. For micromachining, short pulses are preferable because this limits thermal diffusion and leads to deterministic damage.

We consider transparent materials, i.e. dielectrics where the band gap between valence band and conduction band is larger than the photon energy of the laser. This implies that ionization requires absorption of multiple photons; there is no linear absorption mechanism. This leaves basically two non-linear absorption mechanisms: photoionization and avalanche ionization. The density of conduction band electrons n is given by a rate equation,

$$\frac{\mathrm{d}n}{\mathrm{d}t} = w_{PI}(I) + \eta(I)n, \tag{10.1}$$

with w_{PI} the photoionization rate and $\eta(I)$ the avalanche rate. For longer pulses, also electron losses by diffusion, recombination and trapping should be taken into account.

Depending on the laser frequency and intensity, there are two different regimes of photoionization, the multiphoton and the tunneling regime, as outlined in sec. 5.1. If one plots the tunneling and multiphoton ionization rates for common transparent materials as a function of the Keldysh parameter γ (5.1), the two curves cross at about $\gamma \approx 1.5$. For $\gamma > 1.5$ the multiphoton contribution, and for $\gamma < 1.5$ the tunneling contribution overwhelmingly dominate the total ionization rate.

10.1 Avalanche ionization (AVI)

An electron avalanche evolves in 3 steps:

- It is seeded by initially available conduction-band electrons.
- The laser field accelerates these electrons by inverse bremsstrahlung, which is another word for sequential laser-assisted collisions with the lattice.

[1] A very readable review of this field has been given in [83].

- When the kinetic energy exceeds the ionization threshold, the electron can ionize another electron in a collision.

Seed electrons can be provided by thermally excited charge carriers, by easily ionized impurity states, or by electrons that are directly excited by photoionization. Note that to conserve energy and momentum, a conduction band electron can only absorb a photon if, at the same time, it absorbs or emits a phonon or scatters at an impurity. Thus the avalanche rate is limited by the density of seed electrons and by the electron lattice scattering rate.

Stuart et al. [93] developed a model of avalanche ionization in which the avalanche rate depends linearly on the laser intensity $\eta = \alpha I$. This is the outcome of two approximations. First, the flux doubling approximation, which states that as soon as they have sufficient energy electrons impact-ionize and produce two electrons at the lower energetic end of the conduction band. Second, the model assumes that the energy distribution of the conduction-band electrons does not change as the carrier density increases during the avalanche.

Other groups have criticized this model on grounds of these questionable assumptions and because it contradicts the experimentally observed increase of threshold fluence [2] for decreasing pulse lengths. Instead, they use the expression from Thornber [95] which instead predicts linear scaling of the avalanche rate with the electric field, i.e. the square root of the intensity, $\eta = \beta\sqrt{I}$.

The term "optical breakdown" (OB) means that the material is irreversibly damaged, which requires destruction of the crystal lattice. This occurs when the temperature of the material becomes high enough for the material to melt or fracture. For this, energy needs to be transferred from the electrons to the lattice via phonon emission.

The damage mechanism differs depending on the duration and intensity of the laser pulse. For comparison, we assume pulses of the same fixed fluence, i.e. the same total number of incident photons per unit area.

Note that experimental measurements of breakdown threshold intensities are afflicted with numerous uncertainties in defining and measuring material damage and laser intensity in the sample. Most experiments have concentrated on surface effects, while theory treats only bulk effects. Only recently, some experiments directly used changes in the bulk to diagnose OB, e.g. [76].

10.2 Long pulses, t > 10 ps

For pulses of duration of a few picoseconds or longer, the energy is transferred from the electrons to the lattice on the same time scale as the energy is deposited by the laser, i.e. on the order of the pulse duration. The energy is then carried out of the focal volume by thermal diffusion. Hence the damage threshold is determined by the ratio of energy deposition to thermal diffusion. Under these assumptions, the threshold fluence scales as the square root of the pulse duration. Since avalanche is much more efficient,

[2] The fluence is the integral of the intensity over the whole pulse length τ, $F = \int_0^\tau \mathrm{d}t I(t)$.

the threshold intensities are too low for direct photoionization. Thus the avalanche is started either by thermally excited electrons or by impurity and defect states. The damage threshold is extremely sensitive to the presence of impurity electrons and is thus non-deterministic with respect to laser and material parameters.

10.3 Short pulses, t < 10 ps

For pulses shorter than a few picoseconds, the energy is deposited in the electrons faster than it can be transferred to the lattice. The electron density grows through avalanche ionization until the plasma frequency approaches the frequency of the incident laser, which happens at the critical plasma density $n_{\mathrm{cr}} \sim 10^{21}$ cm^{-3}. The high-density plasma strongly absorbs the laser energy. After the laser is gone, the energy is transferred from the electrons to the lattice very abruptly, much faster than the thermal diffusion can redistribute the energy. This leads to ablation or permanent structural damage, but the damage is strongly localized at the laser focus. Also, the total amount of energy deposited is much smaller than for longer pulses. For short pulses, the intensities needed for permanent damage are high enough to create seed electrons by photoionization. Thus the avalanche is less dependent on defects and the breakdown threshold is deterministic.

Thus femtosecond pulses are suited for micromachining as they produce more reproducible and spatially confined damage. Because thermal diffusion does not take place, they deposit less energy in a better defined region.

10.4 Ultrashort pulses, t < 100 fs

For very short pulses, time is too short for an avalanche to unfold, as it is limited by collisions of the electron with the lattice. Yudin et al. [106] argue that the timescale for an avalanche to start off is around 30–50 fs. The typical energy absorbed by an electron in a collision is about $2U_p \sim 1.2$ eV (at $I \sim 10^{13}$ W cm^{-2} and $\lambda = 800$ nm), which happens every half laser cycle. Hence, for fused silica (band gap 9 eV) and under optimal conditions, it takes at least ~ 10 laser half-cycles after the photoionization at the pulse peak before the electron has acquired sufficient energy for impact ionization. This corresponds to pulse durations of $\sim$ 30–50 fs.

Nevertheless, there are experimental reports of avalanche ionization operating for pulses as short as 10 fs [54]. How can an avalanche form at these short pulse lengths? Yudin et al. [106] propose two novel mechanisms for exponential enhancement of photoionization.

The first new mechanism is collision-assisted multiphoton ionization (or, equivalently, laser-assisted impact ionization). An electron in the conduction band with kinetic energy below the band gap can still promote another electron into the conduction band if the missing energy is provided by the laser field. Indeed, Rajeev et al. [76] have found indications for such a new ionization mechanism in avalanches. They

can fit their experimental data by assuming an avalanche rate of the form

$$\eta(I) = \alpha_0 I(1 + \beta_1 I), \tag{10.2}$$

and interpret the quadratic intensity dependence as a sign of laser-assisted impact ionization.

The second suggested process is hole-assisted multiphoton ionization. When an electron has been ionized, it leaves a positively charged ion (a hole) behind. In a simple model, the electric field of the hole $\vec{E}_h = \vec{R}/R^3$ combines with the oscillating laser field $\vec{E}_0 \cos \omega t$ to act on a neighboring atom. In the tunneling regime, this field enters exponentially into the ionization rate

$$\Gamma(t) \sim \exp\left(-\frac{2(2I_p)^{\frac{3}{2}}}{3|\vec{E}\cos\omega t + \vec{E}_h|}\right) \tag{10.3}$$

and enhances the effect of the laser. This mechanism is similar to enhanced ionization in molecules mentioned in sec. 5.2, and ionization ignition in clusters. As soon as new holes are created, they in turn continue to assist ionization at their neighbors. The ionization propagates in a way similar to forest fires. Isolated holes serve as nucleation sites around which new holes are created. The expansion of the ionized region then continues along its boundary.

Note that the forest fire mechanism is supposed to proceed exclusively via the additional electric field of the hole. There is no significant exchange of energy or momentum (like in impact ionization or inverse bremsstrahlung).

11 Cold electron-assisted field ionization

Based on the heuristic picture of forest fire described in the previous chapter, we conceive a model suitable for our MCTDHF code. So far, the forest fire has been verified only in a simple 1D computer model [106], where the nearby hole has been represented by a nearby Coulombic potential well (or, for comparison with analytic SFA theory, by its dipole field). The authors argue that the positively charged ion is much heavier than the electrons and does not move appreciably so that the fixed-in-space approximation is justified. However, the effective mass of holes in common dielectrics is very similar to that of electrons.

Therefore we think that it is more suitable to model the hole by a second electron. The polarity should not make much of a difference, as enhancement and suppression of laser field alternate at each half-cycle of the laser pulse. Another difference is the indistinguishability of an electron pair as opposed to an electron-hole pair.

11.1 Construction of model system

As a simple model of "forest-fire" ionization in solids, we use a two-electron system where one electron is bound to a nucleus in a hydrogen-like potential and the other is in the continuum. The free electron is meant to mimick the hole left over from a previous ionization event. Its energy is assumed to have already thermalized by collisions. The system is then exposed to a few-cycle laser pulse. To evaluate the effect of the charge carrier (the free electron) on the laser ionization of the bound subsystem, we compare the ionization yield of the bound subsystem in the absence of the free electron to the ionization yield of the two-electron system. Ionization is defined as the probability of finding the single or both electrons, respectively, outside a specified range around the nucleus (see below). We expect the latter yield to be significantly enhanced with respect to the former.

The crucial step is to represent the two-electron system in a way that faithfully models the conditions of the real physical situation in the dielectric.

11.1.1 Initial state

We construct our initial state in Hartree-Fock form from the product of a bound state (say, the 1s state) times a continuum state χ,

$$|\Psi\rangle = \mathcal{A}[|1s\rangle \otimes |\chi\rangle]. \tag{11.1}$$

For the continuum state, there are in principle two possible choices (similar to scattering theory):

(a) Scattering eigenstate,

(b) Wave packet.

To get a physically sensible representation of the situation, the two-electron wave function should meet the following criteria:

(i) The bound and continuum state should be orthogonal.

(ii) The energy of the continuum state should be on the order of thermal energies since we want to avoid impact ionization.

11.1.2 Scattering state

If we take for χ a single-electron scattering eigenstate of the binding (Coulomb) potential, then the condition of orthogonality is automatically fulfilled. The energy of the state can be chosen suitably.

However, there remains a problem: the product of the two single-particle states is very far from an eigenstate of the 2-particle Hamiltonian. Since both states have significant spatial overlap, the electron-electron repulsion will strongly distort the system at the start of time-propagation and lead to significant spurious double ionization.

An alternative would be to turn on the interaction adiabatically in order that the initial state relaxes into a 2-particle wave packet. But to avoid initial double ionization, this has to be done very slowly, on a time scale comparable to the time needed for a distant wave packet to reach the atom (see next section). Though this would work in principle, relaxation obscures the previous definite-momentum property of the initial state (it contains again a range of momenta, i.e. it becomes a wave packet). In summary, the scattering state offers no real benefit over starting from a wave packet right away, since it evolves into such anyway. Actually, there is the disadvantage that we do not know exactly what kind of wave packet we get.

A potential advantage could be that the scattering state has less free parameters than a wave packet: only the (single-particle) energy and the norm (a measure for the electron density at the atom).

11.1.3 Wave packet

In view of the above-mentioned considerations, we ultimately decided to use the wave packet approach. We made a serious effort to construct a wave packet that gently scatters from the atom.

1. Shape: We considered Gaussian and $\cos^2$ shapes. The latter offers the advantage of a finite support and thus minimal overlap with the bound state as well as a small box size. A $\cos^2$ wave packet in cylindrical coordinates reads:

$$\chi(z,\rho) = N\cos^2\left(\sqrt{\frac{(z-z_0)^2}{\sigma_z^2}}\,\frac{\pi}{2}\right)\cos^2\left(\sqrt{\frac{\rho^2}{\sigma_\rho^2}}\,\frac{\pi}{2}\right), \tag{11.2}$$

   where N is a normalization factor. For 1D, the last $\cos^2$ is dropped. As it is

more efficient, we perform parameter search in 1D.

2. Distance z_0 from atom: The wave packet is located at a large distance from the atom to minimize the overlap of states and influence of electron-electron interaction. The choice of z_0 is limited by σ_z on the lower side, and by computing time on the upper side. In 3D, too far distances will also lead to extensive wave packet spreading and thus low electron current on the atom itself.

3. Width: For physical reasons, we decided that we need very slow initial electron momenta, somewhere near thermal energies and not larger than the laser's U_p. The parameter to control this is the width of the initial wave packet. If the width is to small, there is a large portion of high momentum components, which whizz over the atom very fast. Even if this leads to enhanced ionization, it would rely on a mechanism much different from the forest fire model.

   We find sizable (orders of magnitudes) dependence of ionization on the initial width, if that width is narrow. A width of, e.g., 7.5 translates into scattering momenta of approximately $2\pi/7.5 \sim 1$ or energies on the scale of 20 eV. In that case we get significant impact ionization and on top of it a smaller scale effect due to the laser (red curves in fig. 11.1). When the widths are larger and energies are below 1 eV (width 45 and 75) there is no impact ionization. Also, the additional effect of the laser is largely independent of the exact width (green and blue curves in fig. 11.1).

   We wait and let the wave packet expand until it arrives in sizable strength near the atom (fig. 11.2). We see that the narrower wave packet (width 45) causes higher densities, but contains also faster momentum components, as it reaches the atom faster. Thus we settle for the broader wave packet.

To summarize the parameters of the wave packet used in the following calculations: $z_0 = 100$, $\sigma_z = 75$, $\sigma_\rho = 40$ (in 3D, equal to the total width of the calculation area).

11.1.4 Laser parameters

The wave packet reaches the atom about 15 to 20 laser cycles after release (fig. 11.2). At that time we let a 4 cycle laser pulse hit. The precise time was chosen such that the electron density in the surroundings of the atom reaches a first maximum.

The width of the pulse was made large enough (FWHM 4 optical cycles) to suppress high frequencies. We verified the multi-photon nature of ionization by checking the scaling behaviour of the unassisted single-electron ionization yield with intensity. From the ionization potential $I_p = 0.5$ and $\omega = 0.057$, we expect a number of 8–9 photons needs to be absorbed for ionization. With the pulse shape we have chosen, pure photoionization is approximately $\propto I^5$ due to non-negligible spectral width (fig. 11.4, "1e" lines). Multi-photon ionization very easily dominates the ionization and limits meaningful studies to $I \lesssim 10^{13}$ W cm^{-2}.

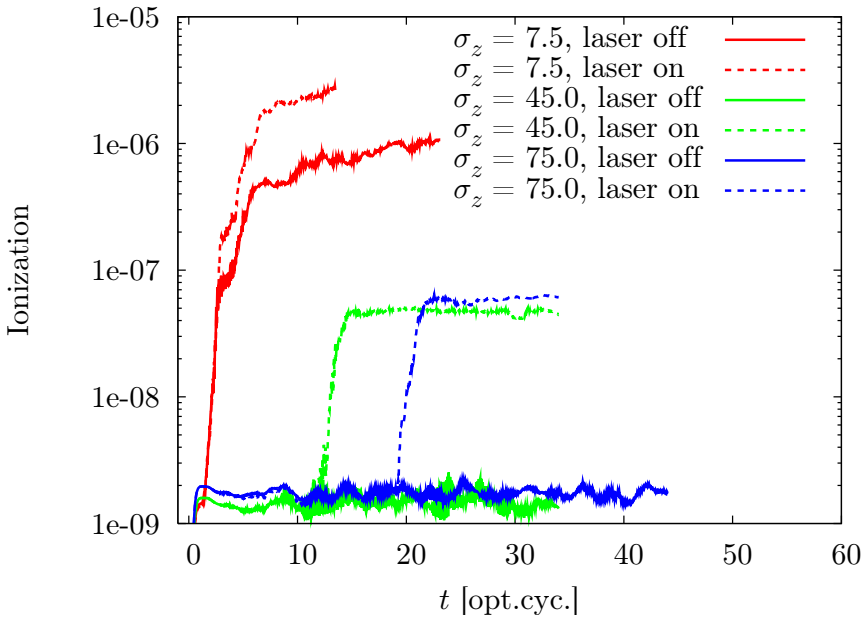

Figure 11.1: Dependence of ionization on wave packet width σ_z in 1D. (Distance of wave packet $z_0 = 100$ in all cases.)

11.1.5 How we determine ionization

We say an ionization has occurred when we find both electrons outside a region around the nucleus. The range of that region ("patch size") was chosen as $z \in [-24, 24]$, a rather large value, as apparently we tend to populate some loosely bound states that lead to oscillations when the patch is inside their range.

Static field ionization After minimizing electron impact ionization by maximizing the width of the electron wave packet, we observe some residual ionization which arises a very short time after we start time propagation from our initial state. Because of the short time delay, this cannot be caused by impact ionization. Rather, the origin of this background is field-ionization of the atom by the charge of the wave packet. The effect can be reduced by 2 to 3 orders of magnitude by placing two identical wave packets symmetrically on both sides of the atom, which eliminates the dipole moment of the charge distribution. This applies both to 1D and 3D (see Fig. 11.3). To factor out the pure field-effect in determining the enhancement, we subtract this initial double ionization pedestal from the double ionization observed after passage of the laser pulse.

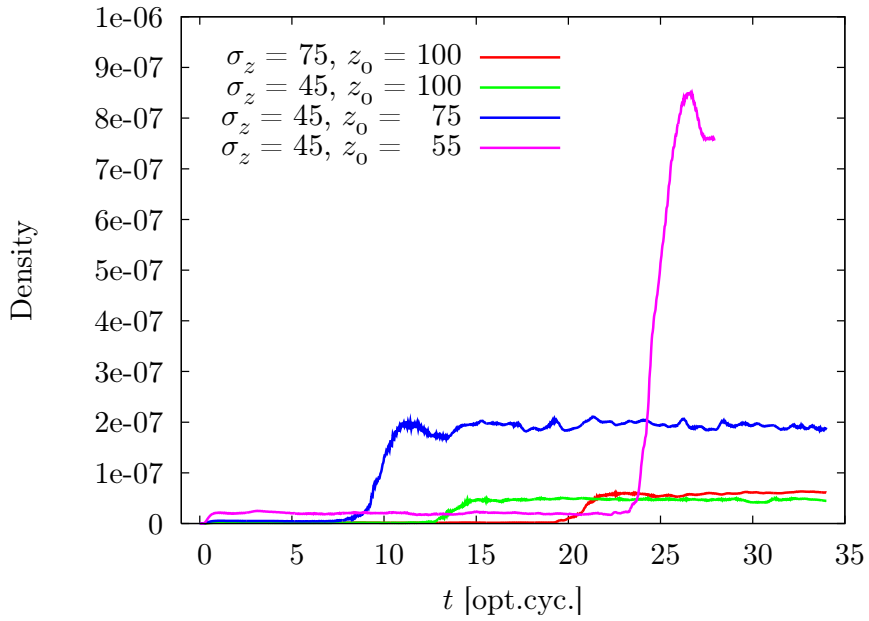

Figure 11.2: Time-dependent electron density averaged over a small box $\rho \in [0, 4], z \in [-5, 5]$ around the nucleus, for the two wave-packets with width 45 and 75, respectively.

11.2 Observation of apparent enhancement

11.2.1 Overview: Enhancement in 1D and 3D as a function of laser intensity

Table 11.1 gives a summary of the ionization enhancement found in Hartree-Fock approximation, for 1D and 3D as a function of laser intensity. Only intensities below 10^{13} W cm^{-2} show significant enhancement on the order of 10^2. Interestingly, the enhancement in 3D seems to be at least on the same scale (if not higher) than in 1D. Figures 11.4 and 11.5 show the ionization curves.

intensity	1e12	2.5e12	1e13
3D	500	500	2.47
1D	250	82.9	1.14

Table 11.1: Ionization enhancement factor: ionization for 2e system divided by ionization for 1e system, in the same laser pulse.

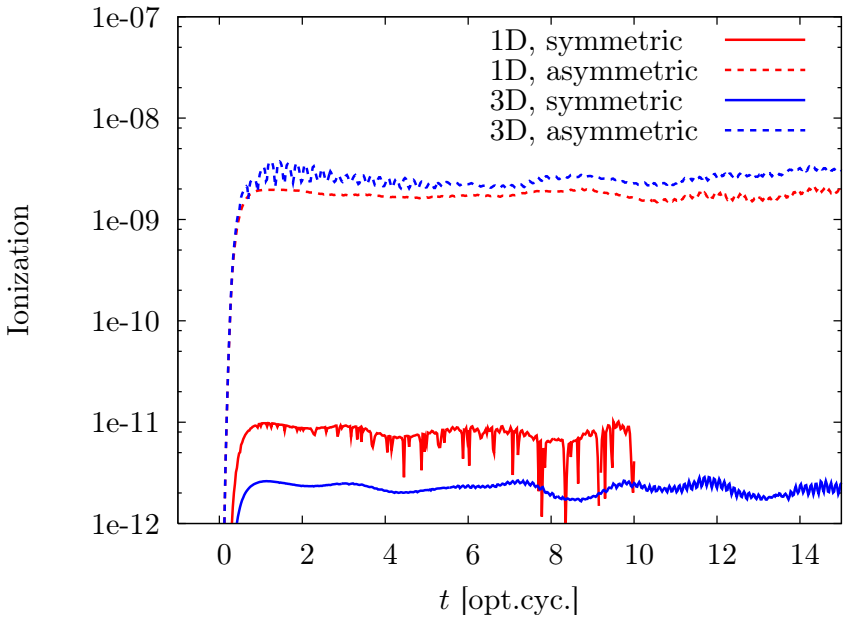

Figure 11.3: Ionization created by the wave packet without laser, either only on one side (asymmetric) or on both sides of the atom (symmetric).

11.2.2 Correlation effects in 1D and 3D

Correlation seems to have no serious (i.e. order of magnitude) impact on ionization, results varying by a factor around 2. (fig. 11.6 in 1D, fig. 11.7 in 3D). Unfortunately, in 1D convergence did not yet set in for 14 orbitals.

Thus, our preliminary conclusion is: we see enhancement of laser ionization by cold electrons, both in 1D and 3D, and it persists with correlation.

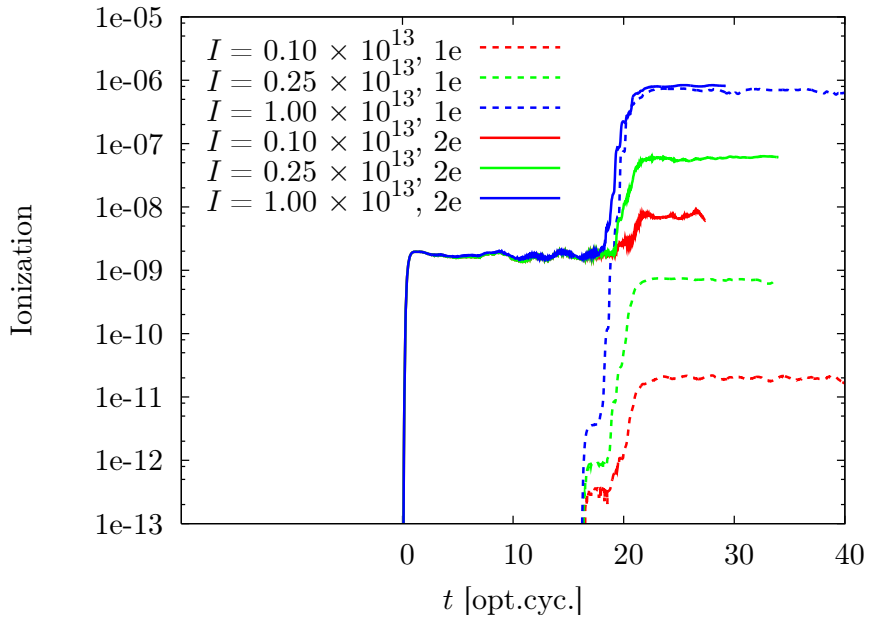

Figure 11.4: Unassisted (1e) and assisted (2e) ionization for different intensities in 1D.

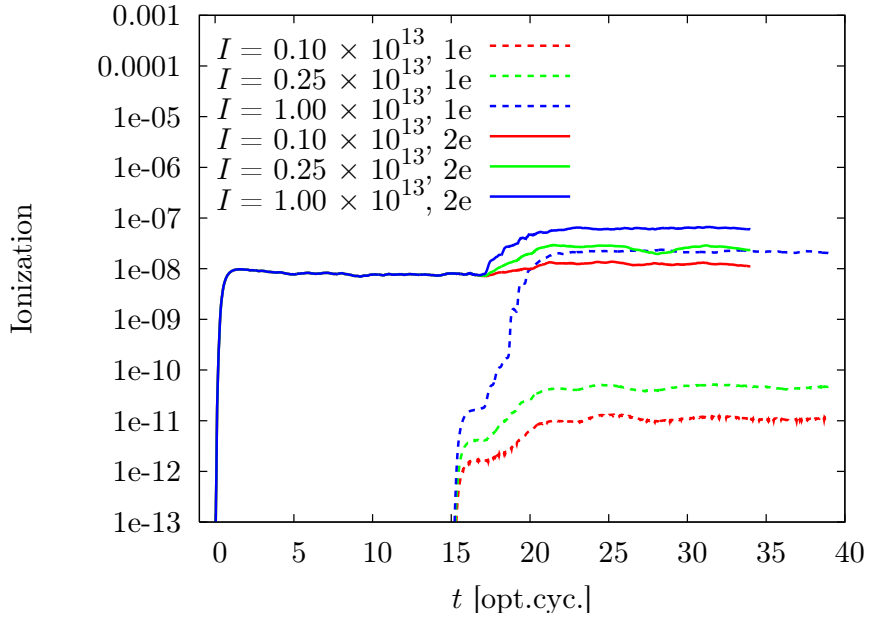

Figure 11.5: Unassisted (1e) and assisted (2e) ionization for different intensities in 3D.

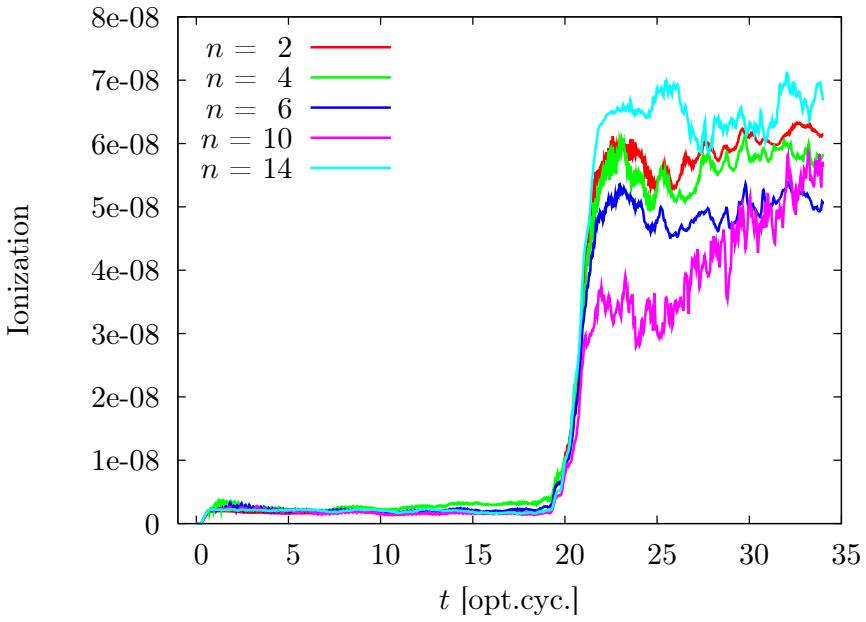

Figure 11.6: Correlation effects in 1D for $I = 2.5 \times 10^{12}$ W cm^{-2}. Note linear scale on y-axis.

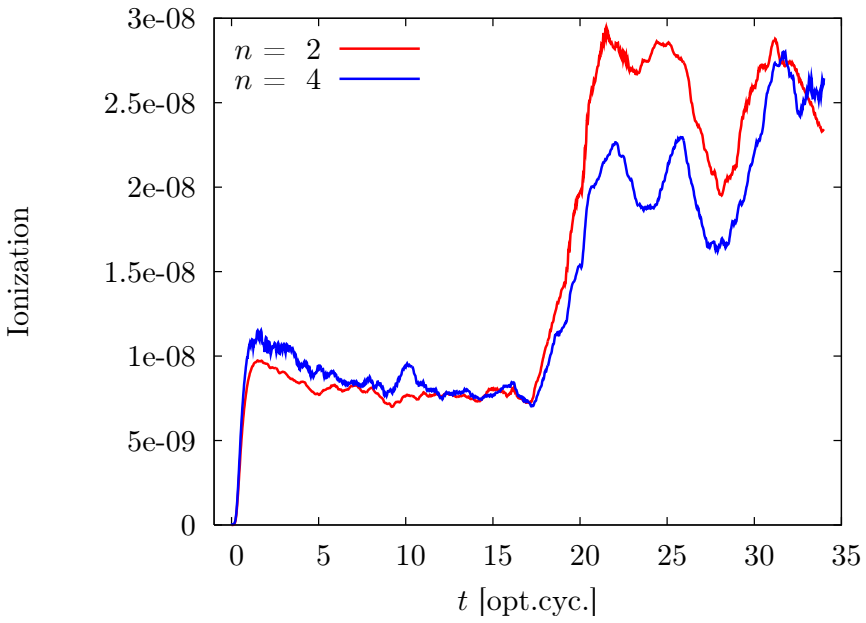

Figure 11.7: Correlation effects in 3D for $I = 2.5 \times 10^{12}$ W cm^{-2}. Note also linear scale on y-axis.

11.3 Failure

Unfortunately, the apparent enhancement does not survive closer scrutiny. We present 3 pieces of counter-evidence, unveiling the bogus nature of the observed effect.

11.3.1 Symmetric wave packet

As observed in sec. 11.1.5 above, the static field of the wave packet generates some initial field ionization, which can be suppressed by using a wave packet symmetric to the left and right of the atom as it makes the field vanish to dipole order. Unfortunately, however, at the same time the enhancement of laser ionization vanishes (fig. 11.8).

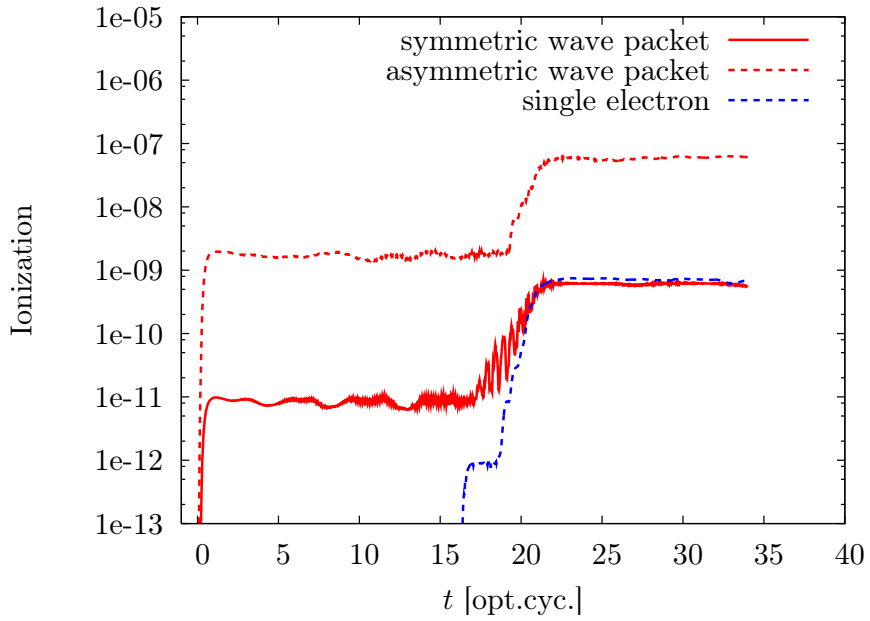

Figure 11.8: Assisted ionization yields in 1D for wave packet either only on one side (asymmetric) or on both sides (symmetric) of the atom ($I = 2.5 \times 10^{12}$ W cm^{-2}).

The explanation is actually quite simple: The electric field of the wave packet not only ionizes, but also excites the atom, and in fact with a much higher probability. The enhancement seems to come purely from the excited populations which have a lower ionization potential and hence are more easily ionized by the laser. Since the total ionization is quite small, these contributions are significant.

It is not completely straightforward to construct a singly-excited state in the case of an interacting two-electron system, where additionally one electron is an evolving wave packet. Strictly speaking, excitation and continuum are only defined for the entire two-particle space. Thus it is difficult to directly check the presence of excitation in the bound subsystem. But we can with little effort make an indirect check described

next.

11.3.2 Adiabatic switch-on of electron-electron interaction

If we regard the electron-electron interaction V_{12} as a perturbation in the independent-particle system, the electron excitation is a consequence of the sudden onset of this interaction, which implies high frequencies. We can avoid these high frequencies by adiabatically turning on the interaction. In practice, adiabatically means a phase-in period of several laser cycles. In fact, if we do this the ionization enhancement disappears, as well (fig. 11.9).

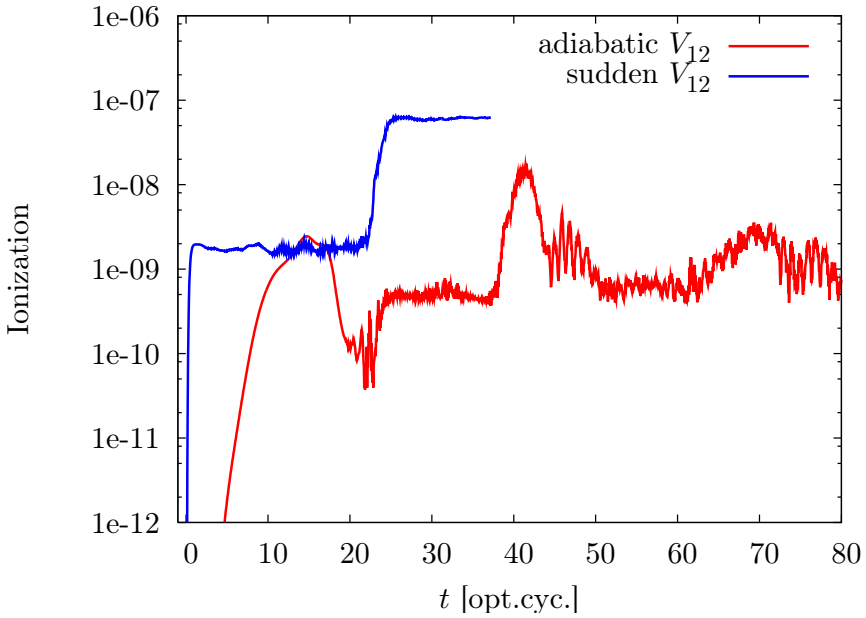

Figure 11.9: Assisted ionization yields in 1D for sudden and adiabatic switch-on of the electron-electron interaction.

11.3.3 Polarized initial atomic state

We now seek to avoid these intial excitation-ionization. The root cause of the problem is that our initial state $\Psi = \mathcal{A}[|1s\rangle \otimes |\chi\rangle]$ does not take into account the polarization of the atom by the static electric field. To arrive at a more realistic two-particle initial state, we diagonalize the single-electron Hamiltonian with a static electric field

$$H_F = H_0 + E_0 z \tag{11.3}$$

within the Hilbert space spanned by the ground state and the first few excited states of the field-free Hamiltonian H_0. This means we diagonalize $\langle i|H_F|j\rangle, i, j = 1, \ldots, 10$

with $H_0|i\rangle = \epsilon_i|i\rangle$. The value of E_0 can be roughly stimated as the electrostatic field of a point charge $-e$ at distance z_0. Ultimately, we choose the optimal E_0 which minimises the initial field ionization. Indeed, using this polarized ground state with a suitable E_0, we get rid of the field-ionization pedestal and – of the laser-ionization enhancement (fig. 11.10).

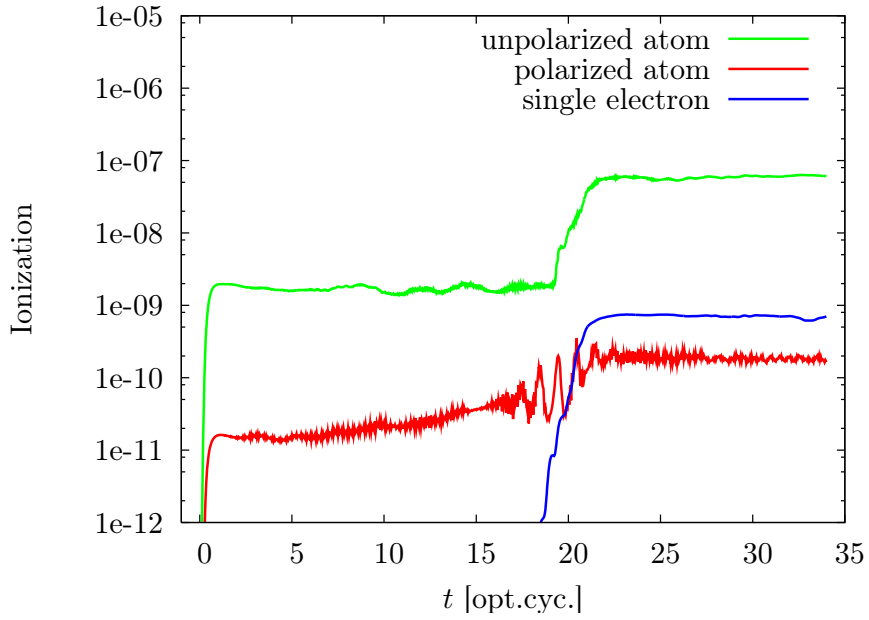

Figure 11.10: Assisted ionization yields in 1D for the unpolarized and the polarized atomic state (with the wave packet on one side only).

11.4 Conclusions

This supplies the final evidence that the observed ionization enhancement is an artefact due to excited states which are populated as the electron-electron interaction is suddenly switched on. The laser just skims off the excited electrons more easily. The ultimate reason lies in the too simple initial state which we originally used and which wrongfully neglects the long-range electron-electron interaction. This is however only admissible asymptotically for infinite distance z_0.

Returning to the original question of the forest fire mechanism: Using a suitable polarized initial state, we find no evidence for cold electron-assisted laser ionization, at least for the used electron energies and laser intensities.

Bibliography

[1] A. S. Alnaser, S. Voss, X. M. Tong, C. M. Maharjan, P. Ranitovic, B. Ulrich, T. Osipov, B. Shan, Z. Chang, and C. L. Cocke. Effects of molecular structure on ion disintegration patterns in ionization of O_2 and N_2 by short laser pulses. *Phys. Rev. Lett.*, 93(11):113003, Sep 2004.

[2] M.-V. Ammosov, N.-B. Delone, and V.-P. Krainov. Tunnel ionization of complex atoms and of atomic ions in an alternating electromagnetic field. *Sov. Phys. JETP*, 64:1191, 1986. [Zh. Eksp. Teor. Fiz. 91, 2008 (1986)].

[3] S. Baker, J. S. Robinson, C. A. Haworth, H. Teng, R. A. Smith, C. C. Chirilă, M. Lein, J. W. G. Tisch, and J. P. Marangos. Probing proton dynamics in molecules on an attosecond time scale. *Science*, 312:424, 2006.

[4] D. Bauer and F. Ceccherini. Time-dependent density functional theory applied to nonsequential multiple ionization of Ne at 800 nm. *Opt. Expr.*, 8:377, 2001.

[5] D. Bauer, D. B. Milošević, and W. Becker. Strong-field approximation for intense-laser atom processes: The choice of gauge. *Physical Review A*, 72(2):023415, 2005.

[6] D. Bauer, D. B. Milošević, and W. Becker. On the validity of the strong field approximation and simple man's theory. *Journal of Modern Optics*, 53(1):135, 2006.

[7] D. Bauer and P. Mulser. Exact field ionization rates in the barrier-suppression regime from numerical time-dependent Schrödinger-equation calculations. *Physical Review A*, 59(1):569, 1999.

[8] M. H. Beck, A. Jäckle, G. A. Worth, and H.-D. Meyer. The Multiconfiguration Time–dependent Hartree (MCTDH) Method: .... *Phys. Rep.*, 324, 2000.

[9] A. Becker, L. Plaja, P. Moreno, M. Nurhuda, and F. H. M. Faisal. Total ionization rates and ion yields of atoms at nonperturbative laser intensities. *Physical Review A*, 64(2):023408, July 2001.

[10] W. Becker, A. Lohr, M. Kleber, and M. Lewenstein. A unified theory of high-harmonic generation: Application to polarization properties of the harmonics. *Physical Review A*, 56(1):645, July 1997.

[11] V. R. Bhardwaj, P. B. Corkum, and D. M. Rayner. Internal laser-induced dipole force at work in C_{60} molecule. *Phys. Rev. Lett.*, 91:203004, 2003.

[12] Thomas Brabec, Michel Côté, Paul Boulanger, and Lora Ramunno. Theory of tunnel ionization in complex systems. *Phys. Rev. Lett.*, 95:73001, 2005.

[13] J. Breidbach and L. S. Cederbaum. Universal attosecond response to the removal of an electron. *Phys. Rev. Lett.*, 94(3):033901, Jan 2005.

[14] P. H. Bucksbaum, A. Zavriyev, H. G. Muller, and D. W. Schumacher. Softening of the H_2^+ molecular bond in intense laser fields. *Physical Review Letters*, 64(16):1883, April 1990.

[15] P. G. Burke and V. M. Burke. Time-dependent R-matrix theory of multiphoton processes. *Journal of Physics B*, 30(11):L383–L391, 1997.

[16] P. G. Burke, P. Francken, and C. J. Joachain. R-matrix-Floquet theory of multiphoton processes. *Journal of Physics B*, 24(4):761–790, 1991.

[17] Szczepan Chelkowski and Andrè Bandrauk. Asymmetries in strong-field photoionization by few-cycle laser pulses: Kinetic-energy spectra and semiclassical explanation of the asymmetries of fast and slow electrons. *Physical Review A*, 71(5):053815, May 2005.

[18] C. C. Chirilă and M. Lein. Assessing different forms of the strong-field approximation for harmonic generation in molecules. *Journal of Modern Optics*, 54(7):1039, 2007.

[19] P. B. Corkum. Plasma perspective on strong-field multiphoton ionization. *Phys. Rev. Lett.*, 71:1994, 1993.

[20] A. S. de Wijn, M. Lein, and S. Kümmel. Strong-field ionization in time-dependent density functional theory. *EPL (Europhysics Letters)*, 84(4):43001, 2008.

[21] P. A. M. Dirac. *Proc. Cambridge Philos. Soc.*, 26:376, 1930.

[22] W. D. Domcke, D. R. Yarkony, and H. Köppel, editors. *Conical intersections. Electronic structure Dynamcis and Spectroscopy.* World Scientific, Singapore, 2004.

[23] M. Drescher, M. Hentschel, R. Kienberger, M. Uiberacker, V. Yakovlev, A. Scrinzi, Th. Westerwalbesloh, U. Kleineberg, U. Heinzmann, and F. Krausz. Time-resolved atomic inner-shell spectroscopy. *Nature*, 419:803, 2002.

[24] J. Feist, S. Nagele, R. Pazourek, E. Persson, B. I. Schneider, L. A. Collins, and J. Burgdörfer. Nonsequential two-photon double ionization of helium. *Physical Review A*, 77(4):043420, 2008.

[25] V. A. Fock. *Izv. Akad. Nauk SSSR Ser. Fiz.*, 18:161, 1954.

[26] J. Frenkel. *Wave mechanics.* Clarendon Press, Oxford, 1934.

[27] Ariel Gordon, Franz X. Kärtner, Nina Rohringer, and Robin Santra. Role of many-electron dynamics in high harmonic generation. *Phys. Rev. Lett.*, 96(22):223902, 2006.

[28] E. Goulielmakis, M. Schultze, M. Hofstetter, V. S. Yakovlev, J. Gagnon, M. Uiberacker, A. L. Aquila, E. M. Gullikson, D. T. Attwood, R. Kienberger, F. Krausz, and U. Kleineberg. Single-cycle nonlinear optics. *Science*, 320(5883):1614–1617, June 2008.

[29] Xiaoxu Guan, C. J. Noble, O. Zatsarinny, K. Bartschat, and B. I. Schneider. Time-dependent R-matrix calculations for multiphoton ionization of argon atoms in strong laser pulses. *Physical Review A*, 78(5):053402, 2008.

[30] Wolfgang Hackbusch. A sparse matrix arithmetic based on H-matrices. Part I: Introduction to H-matrices. *Computing*, 62:89–108, 1999.

[31] S. M. Hankin, D. M. Villeneuve, P. B. Corkum, and D. M. Rayner. Nonlinear ionization of organic molecules in high intensity laser field. *Phys. Rev. Lett.*, 84:5082–5085, 2000.

[32] M. Hentschel, R. Kienberger, C. Spielmann, G. A. Reider, N. Milosevic, T. Brabec, P. Corkum, U. Heinzmann, M. Drescher, and F. Krausz. Attosecond metrology. *Nature*, 414:509, 2001.

[33] A. N. Hussain and G. Roberts. Procedure for absorbing time-dependent wave functions at low kinetic energies and large bandwidths. *Physical Review A*, 63(1):012703, December 2000.

[34] J. Itatani, J. Levesque, D. Zeidler, Hiromichi Niikura, H. Pepin, J. C. Kieffer, P. B. Corkum, and D. M. Villeneuve. Tomographic imaging of molecular orbitals. *Nature*, 432(7019):867–871, 2004.

[35] J. Itatani, F. Quere, G. L. Yudin, M. Yu. Ivanov, F. Krausz, and P. B. Corkum. Attosecond streak camera. *Phys. Rev. Lett.*, 88:173903, 2002.

[36] T. Kanai, Sh. Minemoto, and H. Sakai. Quantum interference during high-order harmonic generation from aligned molecules. *Nature*, 435:470–474, 2005.

[37] Tosio Kato. On the eigenfunctions of many-particle systems in quantum mechanics. *Communications on Pure and Applied Mathematics*, 10(2):151–177, 1957.

[38] Tsuyoshi Kato and Hirohiko Kono. Time-dependent multiconfiguration theory for electronic dynamics of molecules in an intense laser field. *Chem. Phys. Lett.*, 392:533 540, 2004.

[39] L. V. Keldysh. Ionization in the field of a strong electromagnetic wave. *Zh. Eksp. Teor. Fiz.*, 47:1945, 1964. [Soviet Physics JETP 20, 1307 (1965)].

[40] M. Kitzler, J. Zanghellini, Ch. Jungreuthmayer, M. Smits, A. Scrinzi, and T. Brabec. Ionization dynamics of extended multi-electron systems. *Phys. Rev. A*, 70:041401(R), 2004.

[41] Matthias F. Kling and Marc J.J. Vrakking. Attosecond electron dynamics. *Annual Review of Physical Chemistry*, 59(1):463–492, 2008.

[42] Peter Knowles, Martin Schütz, and Hans-Joachim Werner. Ab initio methods for electron correlation in molecules. In J. Grotendorst, editor, *Modern Methods and Algorithms of Quantum Chemistry*, volume 3 of *NIC Series*, pages 97–179. John von Neumann Institute for Computing, 2000.

[43] V. P. Krainov. Ionization rates and energy and angular distributions at the barrier-suppression ionization of complex atoms and atomic ions. *Journal of the Optical Society of America B*, 14(2):425–431, February 1997.

[44] Ferenc Krausz and Misha Ivanov. Attosecond physics. *Reviews of Modern Physics*, 81(1):163, 2009.

[45] K. C. Kulander. Time-dependent Hartree-Fock theory of multiphoton ionization: Helium. *Phys. Rev. A*, 36:2726, 1987.

[46] K. C. Kulander, K. J. Schafer, and J. L. Krause. Dynamics of short-pulse excitation, ionization and harmonic conversion. *Proceedings of the Workshop, Super Intense Laser Atom Physics (SILAP) III, edited by B. Piraux (Plenum, New York)*, 1993.

[47] Alexander I. Kuleff, Jorg Breidbach, and Lorenz S. Cederbaum. Multielectron wave-packet propagation: General theory and application. *The Journal of Chemical Physics*, 123(4):044111–10, July 2005.

[48] Demetris G. Lappas and Robert van Leeuwen. Electron correlation effects in the double ionization of He. *Journal of Physics B*, 31(6):L249–L256, 1998.

[49] M. Lein, E. K. U. Gross, and V. Engel. Intense-field double ionization of helium: Identifying the mechanism. *Phys. Rev. Lett.*, 85(22):4707–4710, Nov 2000.

[50] M. Lein, N. Hay, R. Velotta, J.P. Marangos, and P. L. Knight. Interference effects in high-order harmonic generation with molecules. *Phys. Rev. A*, 66:023805, 2002.

[51] M. Lein, N. Hay, R. Velotta, J.P. Marangos, and P. L. Knight. Role of the intramolecular phase in high-harmonic generation. *Phys. Rev. Lett.*, 88:183903, 2002.

[52] M. Lein and S. Kümmel. Exact time-dependent exchange-correlation potentials for strong-field electron dynamics. *Phys. Rev. Lett.*, 94:143003, 2005.

[53] Manfred Lein. Attosecond probing of vibrational dynamics with high-harmonic generation. *Phys. Rev. Lett.*, 94:53004, 2005.

[54] M. Lenzner, J. Krüger, S. Sartania, Z. Cheng, Ch. Spielmann, G. Mourou, W. Kautek, and F. Krausz. Femtosecond optical breakdown in dielectrics. *Phys. Rev. Lett.*, 80(18):4076–4079, May 1998.

[55] M. Lewenstein, P. Balcou, M. Y. Ivanov, A. L'Huillier, and P. B. Corkum. Theory of high-harmonic generation by low-frequency laser fields. *Phys. Rev. A*, 49:2117, 1994.

[56] M. Lezius, V. Blanchet, M.Yu. Ivanov, and A. Stolow. Polyatomic molecules in strong laser fields: Nonadiabatic multielectron dynamics. *J. Chem. Phys.*, 117:1575, 2002.

[57] I. V. Litvinyuk, Kevin F. Lee, P. W. Dooley, D. M. Rayner, D. M. Villeneuve, and P. B. Corkum. Alignment-dependent strong field ionization of molecules. *Phys. Rev. Lett.*, 90(23):233003, Jun 2003.

[58] Per-Olov Löwdin. Quantum theory of many-particle systems. I. Physical interpretations by means of density matrices, natural spin-orbitals, and convergence problems in the method of configurational interaction. *Physical Review*, 97(6):1474, March 1955.

[59] F. Lépine, S. Zamith, A. de Snaijer, Ch. Bordas, and M. J. J. Vrakking. Observation of large quadrupolar effects in a slow photoelectron imaging experiment. *Physical Review Letters*, 93(23):233003, November 2004.

[60] Alexei N. Markevitch, Stanley M. Smith, Dmitri A. Romanov, H. Bernhard Schlegel, Misha Yu. Ivanov, and Robert J. Levis. Nonadiabatic dynamics of polyatomic molecules and ions in strong laser fields. *Phys. Rev. A*, 68:011402(R), 2003.

[61] A. McPherson, G. Gibson, H. Jara, U. Johann, T. S. Luk, I. A. McIntyre, K. Boyer, and C. K. Rhodes. Studies of multiphoton production of vacuum-ultraviolet radiation in the rare gases. *J. Opt. Soc. Am. B*, 4(4):595–601, 1987.

[62] F. Morales, F. Martin, D. A. Horner, T. N. Rescigno, and C. W. McCurdy. Two-photon double ionization of H_2 at 30 eV using exterior complex scaling. *Journal of Physics B*, 42(13):134013 (8pp), 2009.

[63] R. Moshammer, J. Ullrich, B. Feuerstein, D. Fischer, A. Dorn, C. D. Schröter, J. R. Crespo Lopez-Urrutia, C. Hoehr, H. Rottke, C. Trump, M. Wittmann, G. Korn, and W. Sandner. Rescattering of ultralow-energy electrons for single ionization of Ne in the tunneling regime. *Physical Review Letters*, 91(11):113002, 2003.

[64] J.G. Muga, J.P. Palao, B. Navarro, and I.L. Egusquiza. Complex absorbing potentials. *Physics Reports*, 395(6):357–426, June 2004.

[65] Michael Mundt and Stephan Kümmel. Derivative discontinuities in time-dependent density-functional theory. *Phys. Rev. Lett.*, 95(20):203004, Nov 2005.

[66] J. Muth-Böhm, A. Becker, and F. H. M. Faisal. Suppressed molecular ionization for a class of diatomics in intense femtosecond laser fields. *Phys. Rev. Lett.*, 85(11):2280–2283, Sep 2000.

[67] Y. Öhrn and G. Born. Molecular electron propagator theory and calculations. *Adv. Quantum Chem.*, 13, 1981.

[68] J. S. Parker, B. J. S. Doherty, K. T. Taylor, K. D. Schultz, C. I. Blaga, and L. F. DiMauro. High-energy cutoff in the spectrum of strong-field nonsequential double ionization. *Physical Review Letters*, 96(13):133001, 2006.

[69] J. S. Parker, K. J. Meharg, G. A. McKenna, and K. T. Taylor. Single-ionization of helium at Ti:sapphire wavelengths: rates and scaling laws. *Journal of Physics B*, 40(10):1729–1743, 2007.

[70] Serguei Patchkovskii, Zengxiu Zhao, Thomas Brabec, and D. M. Villeneuve. High harmonic generation and molecular orbital tomography in multielectron systems: Beyond the single active electron approximation. *Phys. Rev. Lett.*, 97(12):123003, 2006.

[71] Domagoj Pavičić, Kevin F. Lee, D. M. Rayner, P. B. Corkum, and D. M. Villeneuve. Direct measurement of the angular dependence of ionization for N_2, O_2, and CO_2 in intense laser fields. *Physical Review Letters*, 98(24):243001, 2007.

[72] A. M. Perelomov, V. S. Popov, and M. V. Terent'ev. Ionization of atoms in an alternating electric field. *Sov. Phys. JETP*, 23:924–934, 1966.

[73] M. Petersilka and E. K. U. Gross. Strong-field double ionization of helium: a density-functional perspective. *Laser Phys.*, 9(1):105, 1999.

[74] D. Pinkham and R. R. Jones. Intense laser ionization of transiently aligned CO. *Phys. Rev. A*, 72(2):023418, Aug 2005.

[75] Jakub S. Prauzner-Bechcicki, Krzysztof Sacha, Bruno Eckhardt, and Jakub Zakrzewski. Quantum model for double ionization of atoms in strong laser fields. *Physical Review A*, 78(1):013419, 2008.

[76] P. P. Rajeev, M. Gertsvolf, P. B. Corkum, and D. M. Rayner. Field dependent avalanche ionization rates in dielectrics. *Physical Review Letters*, 102(8):083001, 2009.

[77] H. R. Reiss. Spectra of atoms at nonperturbative laser intensities. *Physical Review A*, 65(5):055405, May 2002.

[78] T. N. Rescigno and C. W. McCurdy. Numerical grid methods for quantum-mechanical scattering problems. *Phys. Rev. A*, 62(3):032706, Aug 2000.

[79] U. V. Riss and H.-D. Meyer. Investigation on the reflection and transmission properties of complex absorbing potentials. *J. Chem. Phys.*, 105:1409, 1996.

[80] Camilo Ruiz, Luis Plaja, Luis Roso, and Andreas Becker. Ab initio calculation of the double ionization of helium in a few-cycle laser pulse beyond the one-dimensional approximation. *Physical Review Letters*, 96(5):053001, 2006.

[81] Erich Runge and E. K. U. Gross. Density-functional theory for time-dependent systems. *Phys. Rev. Lett.*, 52(12):997, Mar 1984.

[82] Robin Santra and Ariel Gordon. Three-step model for high-harmonic generation in many-electron systems. *Phys. Rev. Lett.*, 96:073906, 2006.

[83] Chris B. Schaffer, Andre Brodeur, and Eric Mazur. Laser-induced breakdown and damage in bulk transparent materials induced by tightly focused femtosecond laser pulses. *Measurement Science and Technology*, 12(11):1784–1794, 2001.

[84] A. Scrinzi and N. Elander. A finite element implementation of exterior complex scaling. *J. Chem. Phys.*, 98:3866, 1993.

[85] Armin Scrinzi. Attosecond physics. Lecture notes, 2007.

[86] Tamar Seideman, M. Yu. Ivanov, and P. B. Corkum. Role of electron localization in intense-field molecular ionization. *Phys. Rev. Lett.*, 75(15):2819–2822, Oct 1995.

[87] J. Seres, P. Wobrauschek, Ch. Streli, V. S. Yakovlev, E. Seres, F. Krausz, and Ch. Spielmann. Generation of coherent keV X-rays with intense femtosecond laser pulses. *New Journal of Physics*, 8(10):251, 2006.

[88] Olga Smirnova, Michael Spanner, and Misha Ivanov. Coulomb and polarization effects in sub-cycle dynamics of strong-field ionization. *J. Phys. B*, 39(13):S307–S321, 2006.

[89] Olga Smirnova, Michael Spanner, and Misha Ivanov. Analytical solutions for strong field-driven atomic and molecular one- and two-electron continua and applications to strong-field problems. *Physical Review A*, 77(3):033407, 2008.

[90] Marc Smits, C. A. de Lange, Albert Stolow, and D. M. Rayner. Absolute ionization rates of multielectron transition metal atoms in strong infrared laser fields. *Physical Review Letters*, 93(21):213003, November 2004.

[91] Marc Smits, C. A. de Lange, Albert Stolow, and D.M. Rayner. Dynamic polarization in the strong-field ionization of small metal clusters. *Phys. Rev. Lett.*, 93:203402, 2004.

[92] Edward S. Smyth, Jonathan S. Parker, and K.T. Taylor. Numerical integration of the time-dependent schrödinger equation for laser-driven helium. *Comput. Phys. Commun.*, 114:1–14, 1999.

[93] B. C. Stuart, M. D. Feit, S. Herman, A. M. Rubenchik, B. W. Shore, and M. D. Perry. Nanosecond-to-femtosecond laser-induced breakdown in dielectrics. *Phys. Rev. B*, 53(4):1749–1761, Jan 1996.

[94] Suren Sukiasyan, Chris McDonald, Carlos Destefani, Misha Yu. Ivanov, and Thomas Brabec. Multielectron correlation in high-harmonic generation: A 2d model analysis. *Physical Review Letters*, 102(22):223002, 2009.

[95] K. K. Thornber. Applications of scaling to problems in high-field electronic transport. *Journal of Applied Physics*, 52(1):279–290, 1981.

[96] X. M. Tong, S. Watahiki, K. Hino, and N. Toshima. Numerical observation of the rescattering wave packet in laser-atom interactions. *Physical Review Letters*, 99(9):093001–4, 2007.

[97] X. M. Tong, Z. X. Zhao, and C. D. Lin. Theory of molecular tunneling ionization. *Phys. Rev. A*, 66(3):033402, Sep 2002.

[98] R. Torres, N. Kajumba, Jonathan G. Underwood, J. S. Robinson, S. Baker, J. W. G. Tisch, R. de Nalda, W. A. Bryan, R. Velotta, C. Altucci, I. C. E. Turcu, and J. P. Marangos. Probing orbital structure of polyatomic molecules by high-order harmonic generation. *Phys. Rev. Lett.*, 98(20):203007, 2007.

[99] M. Uiberacker, Th. Uphues, M. Schultze, A. J. Verhoef, V. Yakovlev, M. F. Kling, J. Rauschenberger, H. Schröder N. M. Kabachnik and, M. Lezius, K. L. Kompa, H.-G. Muller, M. J. J. Vrakking, S. Hendel, U. Kleineberg, U. Heinzmann, M. Drescher, and F. Krausz. Attosecond real-time observation of electron tunnelling in atoms. *Nature*, 446:627–632, 2007.

[100] H. W. van der Hart, M. A. Lysaght, and P. G. Burke. Time-dependent multielectron dynamics of Ar in intense short laser pulses. *Physical Review A*, 76(4):043405, 2007.

[101] A. Vibok and G. G. Balint-Kurti. Parametrization of complex absorbing potentials for time-dependent quantum dynamics. *The Journal of Physical Chemistry*, 96(22):8712–8719, October 1992.

[102] C. Vozzi, F. Calegari, E. Benedetti, J.-P. Caumes, G. Sansone, S. Stagira, M. Nisoli, R. Torres, E. Heesel, N. Kajumba, J. P. Marangos, C. Altucci, and R. Velotta. Controlling two-center interference in molecular high harmonic generation. *Phys. Rev. Lett.*, 95:153902, 2005.

[103] B. Walker, B. Sheehy, L. F. DiMauro, P. Agostini, K. J. Schafer, and K. C. Kulander. Precision measurement of strong field double ionization of helium. *Phys. Rev. Lett.*, 73(9):1227–1230, Aug 1994.

[104] Jian Wu, Heping Zeng, and Chunlei Guo. Comparison study of atomic and molecular single ionization in the multiphoton ionization regime. *Physical Review Letters*, 96(24):243002–4, June 2006.

[105] Xinhua Xie, Gerald Jordan, Marlene Wickenhauser, and Armin Scrinzi. Time and momentum distributions of re-scattering electrons. *J. Mod. Opt.*, 54:999, 2007.

[106] G. L. Yudin, L. N. Gaier, M. Lein, P. L. Knight, P. B. Corkum, and M. Yu. Ivanov. Hole-assisted energy deposition in clusters and dielectrics in multiphoton regime. *Laser Physics*, 14(1):51–56, 2004.

[107] Gennady L. Yudin and Misha Yu. Ivanov. Nonadiabatic tunnel ionization: Looking inside a laser cycle. *Phys. Rev. A*, 64(1):013409, Jun 2001.

[108] D. Zeidler, A. B. Bardon, A. Staudte, D. M. Villeneuve, R. Dorner, and P. B. Corkum. Alignment independence of the instantaneous ionization rate for nitrogen molecules. *Journal of Physics B*, 39(7):L159–L166, 2006.

[109] Ahmed H. Zewail. Femtochemistry: atomic-scale dynamics of the chemical bond using ultrafast lasers (nobel lecture). *Angew. Chem. Int. Ed. Engl.*, 39:143, 2000.

[110] T. Zuo and A. D. Bandrauk. Charge-resonance-enhanced ionization of diatomic molecular ions by intense lasers. *Phys. Rev. A*, 52(4):R2511–R2514, Oct 1995.